Alma Mater Studiorum – Università di Bologna

DOTTORATO DI RICERCA IN

GEOFISICA

Ciclo XXVII

Settore Concorsuale di afferenza: 04/A4 - GEOFISICA

Settore Scientifico disciplinare: GEO/10– GEOFISICA DELLA TERRA SOLIDA

TITOLO TESI

A multi-instrumental approach to the study of equatorial ionosphere over South America

Presentata da: Claudio Cesaroni

Coordinatore Dottorato	**Relatore**
Prof. Michele Dragoni	Dott. Carlo Scotto

Esame finale anno 2015

… To whom is already here

and to whom is about to be.

Introduction

Since the end of the nineteenth century, when Guglielmo Marconi realized his experiment for the transmission of radio waves across the Atlantic (between Poldhu in Cornwall and Clifden in Co. Galway), the existence of an ionized layer in the upper atmosphere was argued. Only in 1926, Scottish physicist Robert Watson-Watt introduces the term *ionosphere* and, one year later, the physicist Edward V. Appleton confirmed the existence of the ionosphere with his experiment of phase interference patterns. As the Breit and Tuve developed the first *ionosonde,* different kind of experiments and instruments was developed in order to measure the height and the density of the ionized layers of the upper atmosphere mostly because the importance of the radio transmission for military purposes increased. In the second half of the twentieth century, with the increase of technological and scientific interest in the propagation of electromagnetic waves through the atmosphere, also satellite missions have been realized to study the physics governing the morphology and the dynamics of the ionosphere. Some example are the missions Alouette 1 and 2 launched in 1962 and 1965 respectively and ISIS satellites launched in 1969 and 1971 respectively. All these missions was devoted mainly on the study of the ionospheric electron density distribution during quiet and disturbed helio-geophysics conditions. In fact, It was well known since the first studies of the terrestrial ionosphere that the behaviour of the ion and electron in the upper atmosphere is strictly governing by the solar activity and influenced by the geomagnetic field. In the meanwhile, US Navy starts to develop a satellite mission named *Transit* with the aim to furnish a positioning service to the ship during navigation in all weather conditions. First of the six *Transit* satellites reached its orbit in 1960 and since 1967 the first satellite positioning service was made available. Tacking advantage from the experience of *Transit* US Department of Defence started to develop a new satellite fleet and in 1994 the Global Positioning System (GPS) services was made available. These satellites, as the *Transit* ones, transmit on two different frequencies to correct, at least partially, the error induced by the ionosphere. From this, it is clear that, from another point of view, GPS signals can be used to infer information about the ionized upper atmosphere. The global coverage of the GPS and decreasing costs related to the receiver installation and maintenance, make the GPS one of the most used instruments for the investigation of the ionosphere. After the introduction of the GPS some other countries have been developed their own system to allow satellite based positioning such as Russia (GLONASS), China (BiDou) and finally the European community (GALILEO). All these systems is generally named GNSS (Global Navigation Satellite System)

The interaction between the ionosphere and the geomagnetic field lead to some particular features of the ionosphere especially in the low and high latitude regions. In particular, in the region near the geomagnetic equator, the coupling between electric field, generated by thermospheric neutral wind, and the horizontal magnetic field creates a vertical movement of the ionospheric plasma. This vertical drift is the main responsible for the “noise” (known as scintillation) experienced by GNSS signals crossing the low latitude

ionosphere. The influences of the scintillations on the signal can lead to a degradation of the positioning performance and even to a complete loss of the signal tracking by the receiver.

In the framework of the FP7 programme, CALIBRA (Countering GNSS high Accuracy applications LImitation due to ionospheric disturbance in BRAzil) project was running until February 2015 with the aim to develop countermeasures against the ionospheric disturbances to the high precision GNSS applications in Brazil. A specific working package, leaded by INGV, was dedicated to the ionospheric assessment and, in particular, to the relationship between TEC (Total Electron Content), its spatial gradients and the GNSS scintillation phenomenon occurrence.

This thesis is part of the work performed during this project by the author in strict collaboration with the partners of the project and, in particular, with the INGV people involved in CALIBRA and the Nottingham Geospatial Institute. In the first chapter of this dissertation an overview on the morphology of the ionosphere and its regular variation is given. Particular emphasis is posed on the topics related to the equatorial ionosphere electrodynamics that drive the phenomena described in the next chapters. In chapter 2 an overview of the instruments and technique used to perform all the analysis presented in this thesis is given. Section 2.1 treat the use of GNSS receivers to study the morphology and dynamics of the equatorial ionosphere over Brazil in terms of TEC, scintillations and velocity of the ionospheric irregularities. Section 2.2 is devote to the description of the ground based HF radar (ionosonde), an instrument used to retrieve electron density vertical profile by using an automatic interpretation software developed at INGV (Autoscala, described in section 2.2.3). Last section of chapter 2 (2.3) describe an electron density model, the NeQuick, able to give TEC climatological estimation starting from some fundamental ionospheric parameters (M(3000)F2 and f_oF2). This model is the one adopted by ESA to give ionospheric correction to the users of the new European GNSS constellation GALILEO. Last part of this thesis is devoted to the validation of such model used to retrieve TEC at low latitude regions.

The core of this thesis is given in chapter 3,4 and 5. In the first one the description of the analysis of TEC, its spatial gradients and amplitude scintillation is given in order to establish a relationship between the morphology of the distribution of the electron and the scintillation experienced by GNSS signal. Different original and known technique is applied in order to reach the objectives. Results are given in section 3.2 and summarized in section 3.3. Main conclusions are reported in section 3.4 highlighting the importance of the meridional TEC gradients in the occurrence of the scintillations and confirming the high occurrence of the strongest scintillations in the post sunset hours during spring and summer. Validation of the results by means of their use in the precise positioning algorithms applied in Brazil is given in section 3.3. This section reports the work performed in collaboration with Nottingham Geospatial Institute and described in detail in a paper submitted to *Journal of Geodesy*, at present, under review. This work is also part of a project funded by ESA

and in which the author is involved as tasks leader. This project highlights the importance of the results reached in this thesis also from the technological point of view in the field of the satellite navigation and high precision GNSS applications at low latitude regions.

Chapter 4 is devoted to the analysis of high sampling rate GNSS receivers deployed in Brazil. In particular, two close receivers (about 300 meters far each other) give the opportunity to study the zonal velocity of the small scale ionospheric irregularities by means of an original algorithm (section 4.2) developed by the author starting from the equations and discussions presented by Ledvina et al., 2004. Important results about the correlation between this velocity and amplitude scintillation occurrence is given in section 4.4 together with the comparison between the velocity inferred by this technique and by means of other independent instruments such as Incoherent scatter radar and ionosonde.

Finally, in chapter 5 a validation of the NeQuick model at low latitude region is described. By means of GNSS-derived TEC values and ionosonde derived parameters (M(3000)F2 and f_oF2) and slightly modifying the source-code of the model, is shown that the model can improve its performance if it ingests parameter measured by an ionosonde instead of modelled one (section 5.2). In addition, a proper selection of the ionosonde data input can be applied to further improve the performance of the model in terms of TEC estimation. This algorithm to automatically evaluate the goodness of the ionosonde derived parameters was developed in the framework of this thesis and it is published in a paper on *Advances in Space Research* (Cesaroni et al., 2013).

1. The Equatorial Ionosphere

This initial chapter provides an outline of some fundamental concepts regarding the formation of the ionosphere and its cyclical variations. A theoretical basis is established in order to better understanding the research described in the subsequent chapters. Certain important phenomenon that occur at low latitudes and in the equatorial ionosphere are specifically analysed as an introduction to the results presented in this thesis.

1.1 The ionosphere

The region above 80 km is generally classified as the "upper atmosphere". Due to the low density of neutral particles at this altitude, the free electrons created from the ionization process can survive for a significant time before recombination with ions. The ionization process involves the stripping or addition of one or more electrons from atoms or molecules resulting in positively or negatively charged particles. In the upper atmosphere there is a marked prevalence of positively charged ions generated by loss of an electron rather than negatively charged ions with an extra electron. Ionization in this context occurs when electrons are dislodged from their host ions either by high-energy solar photons (mainly UV and X-rays) or energetic particles precipitating into the atmosphere and colliding with atmospheric gasses. The traditional atomic model (referred to as the "Bohr model" in acknowledgement of this scientist's role in its development) includes one or more electrons orbiting a nucleus of sub-atomic particles called protons and neutrons. Protons exhibit equal but opposite positive and negative charges, respectively. Opposite charges are attracted to each other with what is called the electrostatic or Coulomb force, while matching charges (negative/negative or positive/positive) repel each other. The vast majority of atoms and molecules in the Earth's lower atmosphere have the same number of protons and electrons in each atom making them neutral,. However, in the upper atmosphere there are appreciable numbers of charged particles (ions and electrons). The number of free ions and electrons peaks at altitudes around 300 km forming a region known as the "ionosphere". The vertical structure of this region is shown schematically in Figure 1. The ionosphere is generated primarily by solar electromagnetic radiation in a process called photoionization, with the consequence that the ionosphere is most dense during local daylight hours. The ionosphere does not entirely disappear at night because the necessary recombination time for the ions and electrons (the average time required for all the ions and electrons to unite to form neutral particles) is long enough for the layer to persist overnight. The recombination rate is determined by background density and is consequently high at low altitudes (where density is high), and decreasing with altitude as the density falls. The degree of ionization at any given point is a balance between the rate of production of ions (photoionization), and the rate of loss of ions (recombination).

1.2 Ionospheric vertical structure

There is a tendency for the terrestrial ionosphere to separate into layers at all latitudes, even though different processes are seen to dominate at different latitudes. The D, E, F1, and F2 layers are, however, only distinct at mid-latitudes in the diurnal ionosphere. The various layers generally exhibit a maximum density at a given altitude, with decreasing density above and below the maximum value. Historically, the E layer was discovered first, followed by the F and D layers. The E and F layers are usually defined as shown in Figure 1 using critical frequencies (f_oE, f_oF , f_oF2), peak heights (h_mE, h_mF1, h_mF2), and half-thicknesses (y_mE, y_mF1, y_mF2). The critical frequency is proportional to $\sqrt{n}$ and is the highest frequency that will be reflected from a layer. Any higher frequency electromagnetic waves transmitted upwards towards the layer will pass through it to higher altitudes. A peak density (N_mE, N_mF1, N_mF2) and peak height (altitude of maximum density) are associated with each critical frequency. It is also common to define a half thickness for each specific layer, established from the best fit of a parabola to the electron density profile, within a range of altitude centred on the maximum density. All layers appear during the day, but the F1 layer decays during the night, and the E and F2 layers can be separated by the formation of a distinct E–F valley .

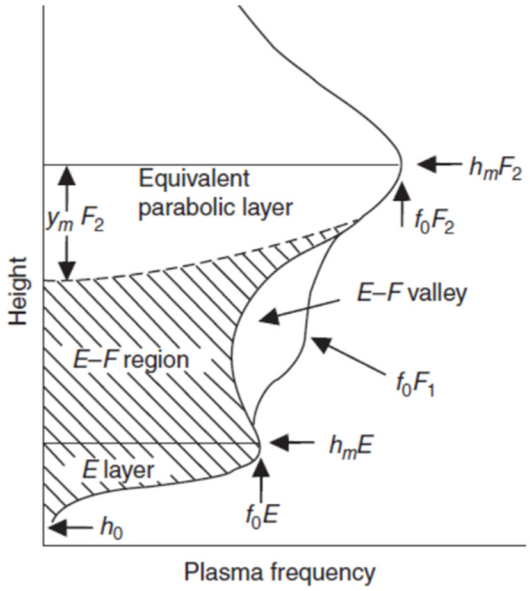

Figure 1. Electron density profiles for daytime (labeled f_0F_1) and nighttime ionosphere (labeled E-F valley). In the figure critical frequencies, peak heights and half-thicknesses for the different layers are also shown. From "Ionospheres Physics, plasma physics and chemistry, Schung and Nagy

Molecular ions (NO^+, O_2^+ , N_2^+) are dominant in the E region with short enough chemical time constants so that plasma transport processes can be ignored. Photochemistry prevails in this context. Notwithstanding the large number of minor ion species in the E region, just a few photochemical processes are sufficient to

provide a good approximate description of the main ions. Since photochemistry is more important here than transport processes, the ion continuity equation for species s can be reduced to:

$$\frac{dn_s}{dt} = P_s - L_s \tag{1.1}$$

where P_s is the production rate and L_s is the loss rate.

A few simplifying assumptions make it possible to establish an analytical expression for electron density in an ionosphere dominated by photochemical reactions. First, one of the molecular ions is assumed to be dominant, implying equality of ion and electron densities. During most daylight hours the time derivative term in the continuity equation is negligible, and the equation can be reduced to:

$$P_e = k_d n_e^2 \tag{1.2}$$

where k_d is the ion–electron recombination rate. Next, it is assumed that the Chapman production function is suitable to describe an ionization rate as a function of altitude, z, and solar zenith angle, χ, giving the derivation:

$$P_c(\mathrm{z},\chi) = \mathrm{I}_\infty \eta\sigma n(\mathrm{z})\mathrm{e}^{-\tau} \tag{1.3}$$

Where

$$\tau = H\sigma n(\mathrm{z})\sec\chi \tag{1.4}$$

$$n(\mathrm{z}) = \mathrm{n}_0\, e^{-(\mathrm{z}-\mathrm{z}_0/\mathrm{H})} \tag{1.5}$$

and where n(z) is the neutral density , H is the neutral scale height, σ is the absorption cross section, I_∞ is the flux of radiation incident on the top of the atmosphere, η is the ionization efficiency, τ is the optical depth, and z_0 is a reference altitude. If the reference altitude is chosen to be the level of unit optical depth (τ = 1) for overhead sun (χ = 0◦), the production rate at z_0 becomes

$$P_{c0} = \mathrm{I}_\infty \eta\sigma n_0\, \mathrm{e}^{-1} \tag{1.6}$$

The Chapman production function can thus be written as:

$$P_{c0}(\mathrm{z},\chi) = P_{c0}\exp\left[1 - \frac{z-z}{H} - \exp\left(\frac{z_0 - z}{H}\right)\sec\chi\right] \tag{1.7}$$

Finally, substitution of the Chapman production function in the continuity equation gives an expression for the Chapman layer:

$$n_e(\mathrm{z},\chi)=\left(\frac{P_{c0}}{k_d}\right)^{1/2}\exp\left\{\frac{1}{2}\left[1-\frac{z-z_0}{H}-\exp\left(\frac{z_0-z}{H}\right)\sec\chi\right]\right\} \tag{1.8}$$

It should be noted that near the layer peak ($z \approx z_0$) the exponentials can be expanded into a Taylor series, and the expression for the electron density can be reduced to

$$n_e(\mathrm{z},0^\circ)\approx\left(\frac{P_{c0}}{k_d}\right)^{1/2}\left[1-\frac{(z-z_0)^2}{4H^2}\right] \tag{1.9}$$

for overhead sun ($\chi = 0^\circ$). The electron density profile is thus parabolic near the layer peak, explaining why half-thicknesses are defined in relation to a parabolic shape.

Generally the F region is divided into three subregions. Photochemistry is dominant in the lowest region labelled F1. The region of transition from dominance of photochemistry to diffusion is labelled F2, and the upper F region dominated by diffusion is called the ionosphere topside. The photochemistry in the F1 region is simplified because a single ion (O+) is dominant. Photoionization of neutral atomic oxygen and losses in reactions with N_2 and O_2 are the most important reactions. Transport processes become increasingly important in the F2 and upper F regions. These include electrodynamic drifts across B, and ambipolar diffusion and wind-induced drifts along B. The magnetic field is essentially straight and uniform at F region altitudes in the mid-latitude ionosphere, but also inclined to the horizontal at an angle I. However, the mid-latitude ionosphere is horizontally stratified resulting in vertically aligned density and temperature gradients (and gravity). The inclination of the B field limits the possibility for diffusion and constrains the charged particles to diffuse along B as a result of the low collision-to-cyclotron frequency ratios. The wind-induced and electrodynamic plasma drifts are also affected by the inclined B field. If $u_{a||}$ is the ambipolar diffusion component of ion velocity along B, then for a vertical force F (g, dT/dz, dn/dz), difussion is driven by the component of F along B, so that $u_{a||} \propto F \sin I$. The vertical component of the ambipolar diffusion velocity, inserted into the continuity equation, is $u_{az} = u_{a||} \sin I$, so that $u_{az} \propto F \sin^2 I$. A meridional neutral wind and a zonal electric field both induce vertical plasma drift . With an equatorward neutral wind (u_n), the induced plasma drift along B is $u_n \cos I$ while the vertical component of plasma velocity is $u_n \sin I \cos I$. Finally, an eastward electric field produces electrodynamic drift with a vertical component equal to (E/B) cos I. Taking all three plasma drifts into account, the ion diffusion equation can be expressed as

$$u_{iz}=\frac{E}{B}\cos I+u_n\sin I\cos I-\sin^2 I D_a\left(\frac{1}{n_i}\frac{\partial n_i}{\partial z}+\frac{1}{T_p}\frac{\partial T_p}{\partial z}+\frac{1}{H_p}\right) \tag{1.10}$$

where $H_p = 2kT_p / (m_i g)$ is the plasma scale height. Equation (1.10) is the "classical" ambipolar diffusion equation for the F2 region, applicable at both mid and high latitudes. The expressions for vertical plasma drifts induced by electric fields and neutral winds are more complicated when magnetic field declination is also taken into account.

The basic shape of the F layer is not affected by neutral winds and electric fields and so their influence can be temporarily ignored. Diffusion is not significant in the daytime F1 region at mid-latitudes and time variations are slow. The O+ (or electron) density can thus be calculated by simply equating the production and loss terms (see Eq.(1.1)). The O+ density increases exponentially with altitude when chemical equilibrium is prevalent (Figure 2).

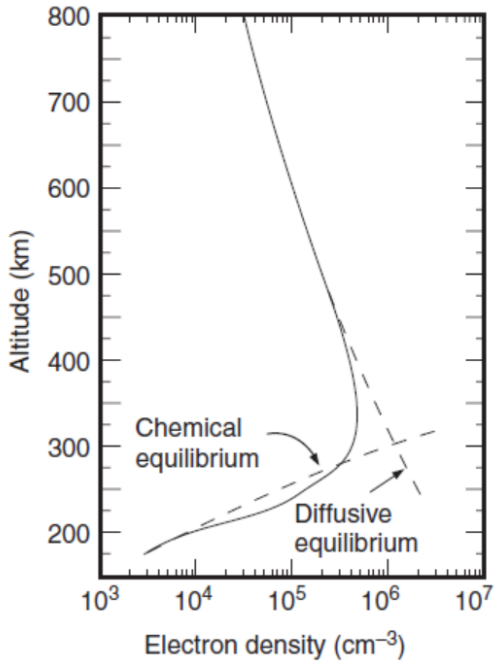

Figure 2. Chemical and diffusive equilibrium profiles and associated mid-latitude F region O^+ profile. From "Ionospheres Physics, plasma physics and chemistry, Schung and Nagy

This is a result of the O+ photoionization rate being directly proportional to the atomic oxygen density, which decreases with altitude exponentially, although less rapidly than the decline in N_2 and O_2 densities. The overall consequence is an exponential decrease in O+ density with altitude. In the upper F region, diffusion is instead dominant, and generally the O+ density presents a diffusive equilibrium profile (Figure 2) generated by setting the parenthesis in the equation (1.10) to zero. O+ density therefore decreases exponentially with altitude at a rate dependent on both the plasma temperature gradient and scale height. The peak density of the F region occurs at the altitude where the prevalence of diffusion and chemical processes are balanced, with equal chemical and diffusion time constants. As already noted, at F region altitudes the charged particles

are constrained to move along B. A neutral wind in a poleward direction thus induces a downward drift of plasma, while a wind towards the equator induces an upward drift of plasma. Similarly, an electric field oriented towards the west induces a downward plasma drift, and an electric field towards the east induces an upward plasma drift. An upward plasma drift shifts the F layer to higher altitudes where the O+ loss rate is lower, causing an increase in both N_mF2 and h_mF2. The opposite occurs when there is a downward plasma drift. There is no photoionization at night and the ionosphere decays. Figure 3 illustrated this decay in an idealized situation, ignoring nocturnal sources of ionization.

Figure 3 shows ionospheric decay in the absence of ionization sources, although this situation is not representative of true nocturnal conditions because different sources of ionization other than direct photoionization do exist at night. The nocturnal E region is maintained by production from starlight and resonantly scattered solar radiation (H Lyman α and β). The nocturnal F region is maintained to some extent by a downward flow of ionization from the upper plasmasphere.

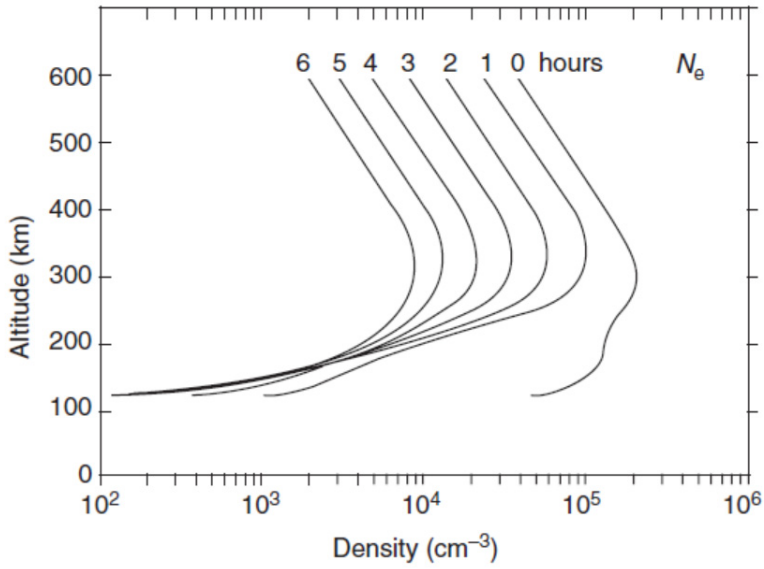

Figure 3. Nocturnal decay of the electron density in the F layer after setting photoionization rate to zero. From "Ionospheres Physics, plasma physics and chemistry, Schung and Nagy

1.3 Geographical and seasonal variations in the ionosphere

There are marked variations in the Earth's ionosphere with changing seasons, latitude, longitude, altitude, universal time, solar cycle, and magnetic activity. Variations are exhibited in all ionospheric parameters including electron density, ion and electron temperatures, and ionospheric composition and dynamics. This is largely a consequence of the coupling of the ionosphere with other components of the solar-terrestrial

system: sun, interplanetary medium, magnetosphere, thermosphere, mesosphere, and to a limited extent also the troposphere and stratosphere . Variations fall into two general categories. The first are reasonably regular, within cycles or quasi-cycles that can be forecast with reasonable accuracy within "quiet" ionospheric conditions. The second are irregular, deriving mostly from sporadic behaviour of the sun and geomagnetic field, difficult to forecast, and representing "disturbed" ionospheric conditions.

Variations in ionospheric electron density caused by temporal cycles can be classified as: diurnal, day-to-day, seasonal, and solar cycles. The effects of the geomagnetic field on the ionosphere also produce regular geographical variations. Overall, five main variations in ionospheric electron density can be defined and need to be taken into account:

1. diurnal variation during daylight hours due mainly to the changing solar zenith angle;
2. seasonal variation during the year;
3. geographic and geomagnetic location;
4. long term solar cycles and disturbances;
5. height variations and the different layers.

These variations have all been experimentally established in worldwide ionospheric observations over recent decades. Routine ionospheric monitoring can be used to establish diurnal, seasonal, solar cycle, and height variations. Figure 4 and Figure 5 illustrate these four variables at a typical mid-latitude station, respectively during solar maximum and minimum, as indicated by the T parameter values.

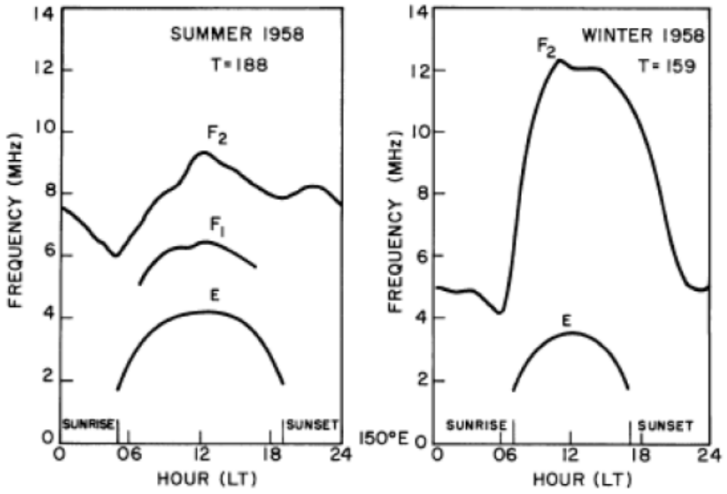

Figure 4. Daily variation of the critical frequencies of the ionospheric layers (E, F_1, F_2) during the solar maximum in 1958 registered at Camberra station (mid-latitude). Left panel shows measurements carried out in June and right panel shows January measurements.

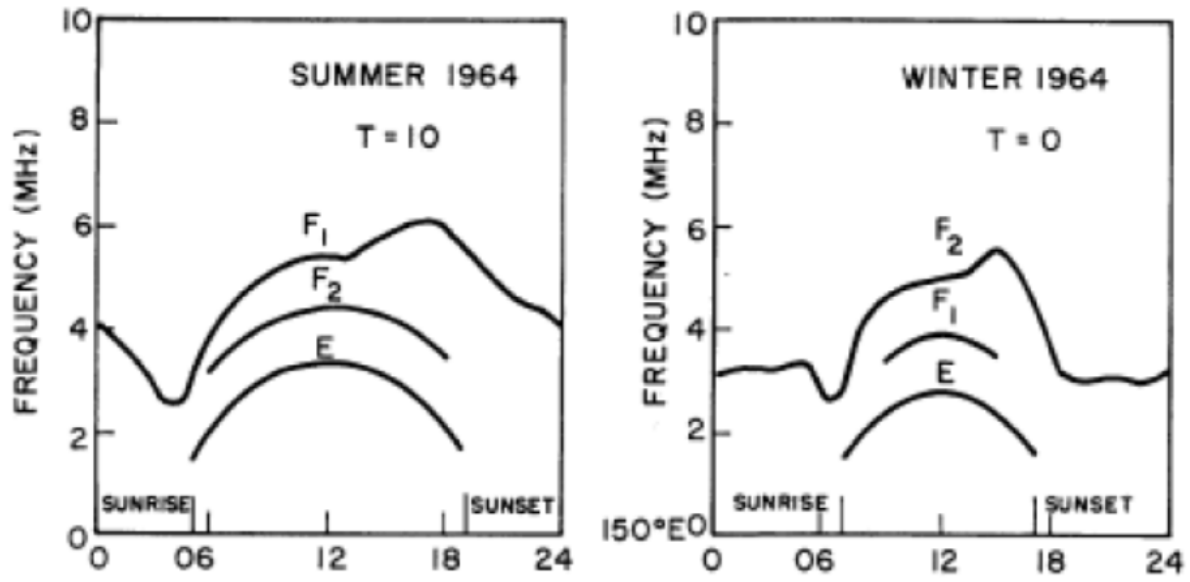

Figure 5. Daily variation of the critical frequencies of the ionospheric layers (E, F_1, F_2) during the solar minimum in 1964 registered at Camberra station (mid-latitude). Left panel shows measurements carried out in June and right panel shows January measurements.

Figure 4 and Figure 5 clearly show that the critical frequencies of the ionospheric layers are higher during a solar maximum than during a solar minimum. Figure 4 also shows an example of the mid-latitude seasonal anomaly, which is the seemingly unlikely fact that f_oF2 is higher in winter than in summer, despite the larger solar zenith angle.

Figure 6 also illustrates how the F2 layer critical frequency, f_oF2, varies at 00 UT in June around the world, under both high and low solar activity. Variations by location were quantified in an international campaign of measurements and data exchange. The relatively simple structure of the E and Fl layers, with foE and f_oF1 contours closely matching the solar zenith angle contours, is seen to be no longer valid, although a clear dependence on zenith angle is observed around sunrise. f_oF2 is also seen to vary by latitude, which is not the case for f_oFE and f_oF1. In Figure 6, f_oF2 is seen to exhibit two afternoon peaks either side of the equator, a feature known as the equatorial anomaly which will be discussed in greater detail in following section.

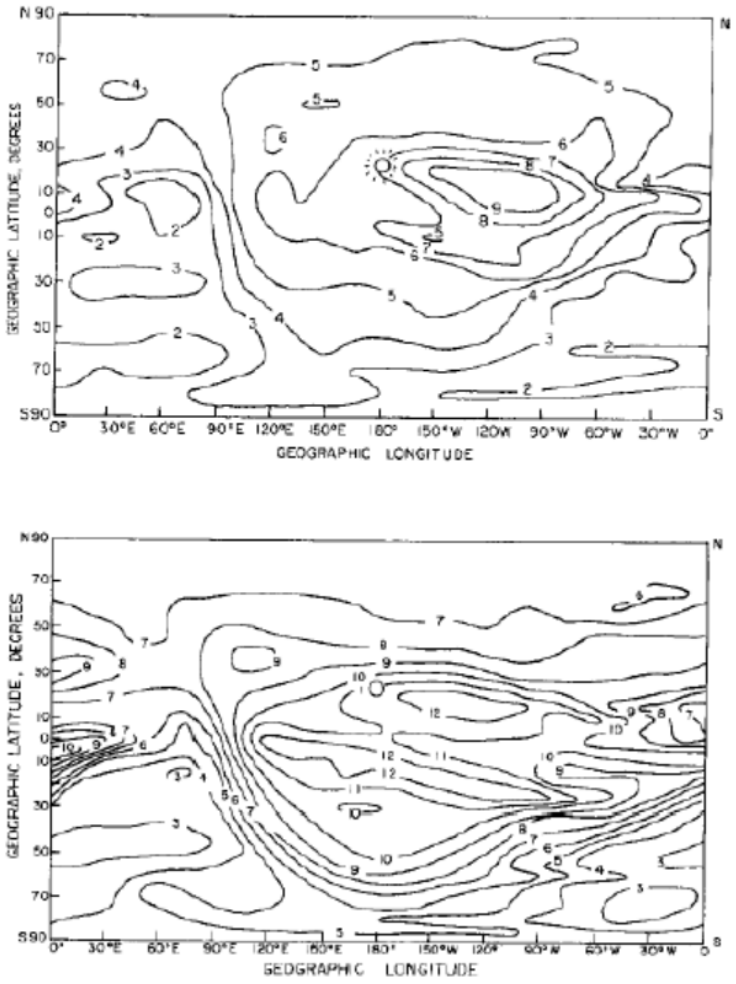

Figure 6. Geographical variation of the critical frequency of the layer F2 during summer for solar minimum (top panel) and maximum (bottom panel).

1.4 Electrodynamics of the Equatorial ionosphere

Since the 1960s, routine ionospheric monitoring has highlighted that the equatorial ionosphere behaves very differently in certain respects from the ionosphere elsewhere. These differences were found to be caused not by the geographic equator but rather by the dip (or magnetic) equator. The dip equator is defined by the locus of points at which the dip angle of the magnetic field is zero, coinciding with the geographic equator only in two points. The orientation of the dip equator relative to the geographic equator is shown in Figure 7, where it clearly emerges how the main variation between the two is over South-America, which is the region considered in the present thesis.

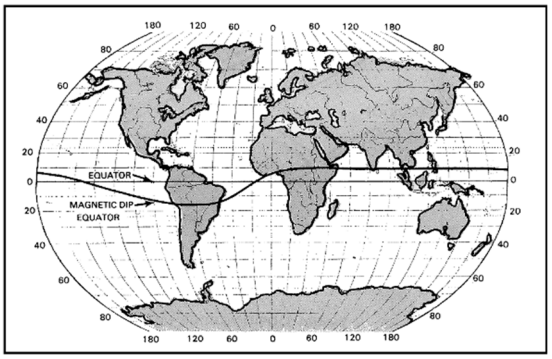

Figure 7. Position of the dip equator (black tick line) with respect to the geographic equator (black thin line).

1.4.1 Equatorial electrojet

At high latitudes the electrodynamics are controlled by an interaction between solar wind and magnetosphere. At the equator the electrodynamics are instead driven by thermospheric winds, which generate the equatorial electrojet and are strongly influenced by the magnetic configuration in the equatorial region. The magnetic field in this region is oriented horizontally from south to north with the field aligned direction lying along the meridian plane. At heights over about 100 km the conductivity parallel to the magnetic field is so strong that the magnetic field lines are almost equipotential with the result that only the zonal (east-west) and vertical directions contribute to the electrodynamics. Below 100 km the conductivity is so weak that this lower ionospheric region makes no significant contributions to the overall dynamics. Thermospheric winds are oriented towards the east during the day and generate an eastward electric field E_P. A vertical Hall current develops as a consequence of this electric field,, mainly due to the electrons, flowing downwards during the day. Subsequently, vertical charge separation occurs in the ionosphere and a vertical electric field E_H develops, constraining the ions in a vertical motion. This acts to reduce the vertical Hall current until it becomes strong enough to block the Hall current completely. Averaging a magnetic field line, by integrating the entire length of the line (characterized by the curvilinear abscissas) gives:

$$E_P \int \sigma_P \, ds = E_S \int \sigma_S \, ds \tag{1.11}$$

The polarization electric field E_H is clearly very influential in the lower ionosphere given that integrated σ_S is much lower than integrated σ_P in this zone. This electric field commonly generates a strong eastward Hall current, known as the equatorial electrojet, further enhancing the zonal direction current J_P. This is how the atmosphere and magnetosphere are coupled. However, Pedersen conductivity rapidly decreases with altitude, along with E_H, so that the polarization field E_H is only strong over a limited range of latitude, limiting the latitudinal extension of the equatorial electrojet .

1.4.2 *Vertical drift and Equatorial ionization anomaly (EIA)*

At altitudes above 100 km, the magnetic field traps ions and electrons. Analogous to the effect at high latitudes, a vertical convectional plasma drift is generated by the Pedersen electric field (caused by the neutral wind), so that with an eastward electric field, the ionosphere is raised higher. At high altitudes this vertical transport gives way to diffusion along the magnetic field lines as a consequence of the influence of gravity. Overall, ionospheric plasma exhibits a fountain-like movement in the equatorial region, known as the equatorial fountain effect. This movement causes plasma to accumulate at latitudes around 10 to 20 degrees north and south of the magnetic equator, generating density enhancements, referred to occasionally as the Appleton anomaly, or Equatorial Ionization Anomaly. The plasma uplift mechanism due to the electric and magnetic fields, and the reductive influence of gravity on the motion, is shown schematically in Figure 8.

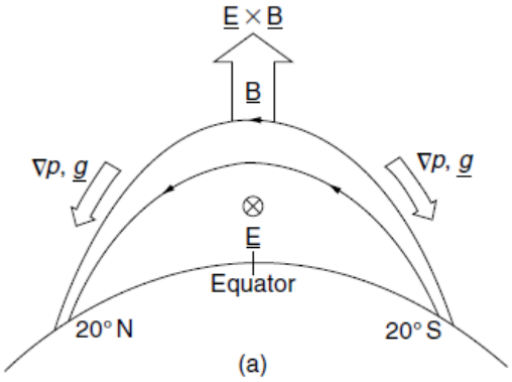

Figure 8. Schematic representation of the plasma motion generating the EIA.

1.4.3 *Rayleigh-Taylor instability and plasma bubbles*

The solar–terrestrial environment is generally in a state of non-equilibrium, maintained by a variety of instabilities in the plasma and fluid systems. Space plasma and terrestrial atmospheric instabilities are induced by countless free energy sources including velocity shear, gravity, temperature anisotropy, electron and ion beams, and currents. Unstable waves are characterized by complex wave frequencies, with a real part describing the rate of wave oscillations, and an imaginary part describing the rate of growth of instability. The latter can be established with the complex solution of a plasma dispersion relation. Plasma instabilities can be classified into macroinstabilities, which occur on scales comparable to the plasma bulk scales, and microinstabilities, which occur on scales comparable with particle motion.. Macroinstabilities are fluid in nature and can be studied using fluid and MHD (magnetohydrodynamic) equations. These instabilities occur in configuration space, so macroinstability lowers the energy state of a system by distorting its configuration. Examples of macroinstability include the Kelvin–Helmholtz instability, and the Rayleigh–Taylor instability. Rayleigh–Taylor instability is also known as interchange instability and is a fluid or plasma boundary macroinstability under the influence of a gravitational field. The gravitational field causes ripples to grow at

the boundary interface causing the formation of density bubbles. The Rayleigh–Taylor instability growth rate is a function of gravitational acceleration. This macroinstability is commonly found in the equatorial ionosphere, where collisions with neutrals considerably transform the instability, generating plasma density bubbles known as equatorial spread-F. These plasma bubbles cause ionospheric GPS signal scintillations.

Figure 9 gives a schematic representation of the Rayleigh-Taylor instability in the equatorial ionosphere. The horizontal dashed line represents the unperturbed plasma boundary. Plasma fills the upper halfspace and the magnetic field is perpendicular to the $x-y$ plane.

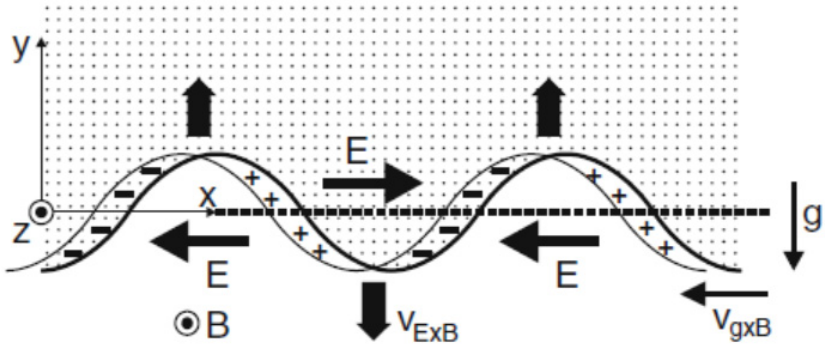

Figure 9. Schematic representation of the Rayleigh-Taylor instability in the equatorial ionosphere. From "Plasma Physics: an introduction to Laboratory, Space and Fusion plasma", Alexander Piel.

Under the influence of gravity, the ions experience a g×B drift at a velocity (ignoring ion-neutral collisions) given by

$$\vec{v}_g = \frac{m}{q}\frac{\vec{g}\times\vec{B}}{B^2} \tag{1.12}$$

The drift velocity of the electrons opposes this, but smaller by a factor m_e/m_i and is ignored. In order to explain the instability mechanism, an initial sinusoidal perturbation of the boundary is considered, as indicated by the heavy line in Figure 9. The g×B drift causes the ions to shift slightly in the $-x$ direction, as indicated by the fine line. This generates positive surplus-charges on the surface due to overloading of ions on the leading edge and diminished ions on the trailing edge. An E×B motion is generated in the perturbed plasma region by these surface charges, as indicated with the box arrows. It should be remembered that E×B drift is the same for electrons and ions and so does not generate further charge separation. This secondary drift effectively amplifies the original perturbation, which is gravitational Rayleigh-Taylor instability mechanism. Rayleigh-Taylor instability was originally used to described the interface between a heavy fluid

(like water) resting on a lighter fluid (like oil). A sinusoidal perturbation of this interface generates rising blobs of oil and descending blobs of water. Equatorial ionospheric plasma rests on the horizontal magnetic field, which here represents the lighter fluid. After the sunset, the lower portions of the ionosphere (the E-region) disappear rapidly by recombination. A steep density gradient forms at the bottom of the F-layer, which can develop Rayleigh-Taylor instability, leading to bubbles of low-density plasma rising into the higher-density F-layer. Rayleigh-Taylor-like instabilities are commonly observed in magnetized plasmas.

1.5 References

This first chapter is a brief review of the physics behind the morphology and dynamics of the ionosphere in particular at equatorial region. The content are well known and well described in the following fundamental text:

Hysell, D. L., Yokoyama, T., Nossa, E. E., Hedden, R. B., Larsen, M. F., Munro, J., Smith, S. M., Sulzer, M. P. and González, S. a.: Aeronomy of the Earth's Atmosphere and Ionosphere, Springer Science & Business Media., 2011.

Kamide, Y. and Chian, A. C.-L.: Handbook of the Solar-Terrestrial Environment, Springer Science & Business Media. [online] Available from: https://books.google.com/books?id=qRN53YwEv7cC&pgis=1 (Accessed 18 February 2015), 2007.

Kelley, M. C.: The Earth's Ionosphere: Plasma Physics & Electrodynamics, Academic Press. [online] Available from: https://books.google.com/books?id=3GlWQnjBQNgC&pgis=1 (Accessed 18 February 2015), 2009.

Kintner, P. M.: Size, shape, orientation, speed, and duration of GPS equatorial anomaly scintillations, Radio Sci., 39(2), n/a–n/a, doi:10.1029/2003RS002878, 2004.

Piel, A.: Plasma physics-An Introduction to Laboratory, Space, and Fusion Plasmas, Springer Science & Business Media., 2011.

Schunk, R.: Ionospheres: Physics, Plasma Physics, and Chemistry, Cambridge University Press. [online] Available from: https://books.google.com/books?id=sCJ8xJGRNYIC&pgis=1 (Accessed 18 February 2015), 2009.

2. Ground based measurements and models for ionospheric studies

This chapter introduces all the instruments and models used to establish the results described in detail in the following chapters. A brief review is also provided of the processing applied to measurements to obtain the ionospheric parameters (TEC, TEC gradients, scintillation indices) subsequently utilized to characterized the behaviour of the equatorial ionosphere.

2.1 GNSS and ionospheric effects on satellite signals

Satellite navigation systems include arrays of satellites that can provide autonomous geo-spatial positioning on a global scale. These systems enable small electronic receivers to establish specific high precision location coordinates (longitude, latitude, and altitude to within a few metres) on the basis of line of sight time signals transmitted by radio from satellites. The system also calculates the current local time of the electronic receivers to high precision, enabling time synchronisation. Satellite navigation systems offering worldwide coverage are known as global navigation satellite systems, abbreviated GNSS.

Global Navigation Satellite System positioning measurements depend on the availability and the accuracy of the satellite readings. GNSS can be used to estimate position, velocity, and time by using transmitted from satellites in known orbits. The accuracy of a GNSS is dependent on various parameters including availability and accuracy of observables, satellite geometry, number of satellites tracked, and operating location. GNSS position errors can be caused by a variety of conditions including clock drift, satellite ephemeris, radio signal propagation, relativistic and atmospheric effects. The main source of errors is the ionosphere, due to its dispersive nature as a medium affecting the propagation of GNSS signals. All measurement error sources have to be assessed and corrected in order to improve system performance.

The number of military, commercial, and scientific applications that take advantage of accurate GNSS positioning and timing information has increased enormously over the last decade. Current GNSS systems cannot guarantee the positions and times calculated by user devices. The integrity of a satellite signal can be lost, especially when used for aircraft navigation. As already noted, the main source of GNSS disturbance is the ionosphere and various methods are adopted in order to minimize its effect. These implement:

- dual-frequency techniques,
- augmentation systems for single frequency receivers,
- corrections based on an ionospheric model.

Dual-frequency techniques apply a linear combination of dual frequency pseudorange measurements to estimate ionospheric delay (the results of this technique are referred to as "iono-free"). This is the most accurate method, but cannot be applied using a single frequency receiver. Single-frequency receivers have to implement ionospheric correction by means of an ionospheric model or augmentation system like

Differential GNSS (DGNSS), or Satellite Based Augmentation System (SBAS). These are based on differential corrections computed by individual stations or a network, and broadcast by terrestrial radio or satellite to GNSS receivers.

The most widely used GNSS system for contemporary navigation is the Global Positioning System, or GPS. This is a fully-operational system that satisfies the requirements stipulated in 1960s for positioning systems. It offers continuous, accurate, three-dimensional position and velocity information on a worldwide basis to users equipped with appropriate receivers. The nominal satellite constellation comprises 24 orbiting on 6 planes with 4 satellites per plane. A ground control network around the world monitors the functionality and status of the individual satellites. The GPS system is divided into three segments: a Control Segment, Space Segment, and User Segment.

The Space Segment includes all the satellites, which transmit the radio-navigation signals and record and retransmit navigation messages issued by the Control Segment. The transmissions are performed with the support of highly accurate atomic clocks on board the satellites.

The Control Segment includes five control stations (at optimal longitudinal intervals around the planet), with one Master Control Station. The control stations serve mainly to monitor the performance of the GPS satellites. They collect data from the satellites and forward it to the Master Control Station for processing. The latter manages all aspects of constellation control and command. The Control Segment serves mainly to monitor GPS performance in compliance with standards, generate and upload navigation data to the satellites, maintain performance standards, and detect any satellite failures in order to minimize negative consequences.

The User Segment consist of the active receivers and their data processing routines. GPS can support an unlimited number of users.

Receivers use navigation data to determine the location of satellites at the time of transmission of received signals, while ranging codes enables them to determine the signal transit time and the satellite-to-user range. The GPS uses the Klobuchar model to correct for ionospheric disturbance, offering an error correction of 50% to 60% RMS (Root Mean Square) of total ionospheric delay. The Klobuchar model parameters are broadcasted in the GPS navigation messages. Highly accurate atomic frequency clocks on board the satellites are synchronized with a GPS time base, and this provides a reference for satellite transmissions. Ranging codes and navigation data are broadcast by the satellites on two carrier signals: L1 (frequency = 1575.42 MHz; wavelength = 19.0 cm), and L2 (frequency = 1227.60 MHz; wavelength = 24.4 cm). The second signal serves for self-calibration of the signal delay caused by the Earth's ionosphere. Binary information is encoded into the carrier signals in a process called phase modulation. Three types of code are included in carrier

signals: C/A code (on the L1 channel), P code (on both the L1 and L2 channels), and the Navigation Message (on the L1 channel).

2.1.1 Ionospheric refractive index and Total electron content

An electromagnetic wave propagating in empty space is known to travel at the speed of light. The speed of a wave propagating in a medium changes due to interaction with the particles of the medium. This is called wave refraction and the degree of refraction is established using a medium specific refractive index. Unfortunately, the refractive index of the ionosphere is not constant due to this medium being inhomogeneous, anisotropic, and dispersive. The refractive index of a dispersive medium depends upon the frequency of the wave. The refractive index for the propagation of electromagnetic waves in a cold magnetized plasma can be expressed as:

$$n^2 = 1 - \frac{X}{1 - iZ - \frac{Y_T^2}{2(1-\mathrm{X}-\mathrm{iZ})} \pm \sqrt{\frac{Y_T^2}{4(1-\mathrm{X}-\mathrm{iZ})^2} + Y_L}} \tag{2.1}$$

Equation (2.1) is known as the Appleton-Hartree equation, in which n^2 is the square of the refractive index, $X = \frac{\omega_0^2}{\omega^2}$, $Y = \frac{\omega_H}{\omega}$, $Z = \frac{\nu}{\omega}$, $\omega = 2\pi f$ is the angular frequency of the transmitted wave, ω_0 is the electron plasma frequency, ω_H is the electron gyro frequency and a function of the magnetic field intensity, and ν is the electron collision frequency.

The positioning signal frequency must be selected to bring n_2 as close as possible to unity (in outer space the refractive index is 1). A refractive index less than 1 causes the wave to be advanced, and greater than 1 causes it to be delayed. A first order approximation of the Appleton-Hartree formula can be used for positioning frequencies:

$$n = \sqrt{1 - X} \tag{2.2}$$

Expanding (2.2), the refractive index can be expressed as:

$$n = 1 - X^2 = 1 - \frac{40.3 N_e}{f^2} \tag{2.3}$$

When N_e is the electron density and f is the frequency of the electromagnetic wave.

Using the first order expansion, the Optical Path (geometrical length of ray plus ionospheric contribution) Λ becomes:

$$\Lambda = \int n \; ds = \int \left(1 - \frac{40.3 N_e}{f^2} \right) ds = D - \frac{40.3}{f^2} \int N_e \; \mathrm{ds} = D - \frac{40.3}{f^2} TEC \tag{2.4}$$

where

$$TEC = \int N_e \; ds \tag{2.5}$$

is the total ionospheric electron content. TEC represents the free electron content of a cylinder with a base of 1 m^2 extending through all the ionospheric altitudes. TEC is typically expressed in TEC units (TECu) defined as:

$$1 \; TECu = 10^{16} \frac{e}{m^2} \tag{2.6}$$

2.1.2 L-band scintillations

One effect of electromagnetic scintillation in the visible frequency range was observed after the introduction of telescopes. This is a rapid random fluctuation of the instant amplitude and phase of a signal. Newton ascribed this phenomenon to atmospheric disturbance and recommended locating telescopes on top of the highest mountains. Further developments in scintillation research began when astronomy started analysing radio frequencies. Scintillation effects were observed when monitoring signals from other galaxies and in particular Cassiopeia. The cause of this scintillation was established using a number of receivers positioned remotely from each other, operating on a range of frequencies. The scintillation effects at the remote receivers were correlated making it possible to establish the Earth's atmosphere as the source of scintillation. A frequency dependence indicated that the scintillating medium was dispersive.

GNSS signals are strongly affected by amplitude and phase scintillation resulting from propagation through the atmosphere. The GNSS signal scintillation effects due to propagation in the troposphere are negligible compared to those generated by the ionosphere. Signal scintillation effects are very important for navigation and geodetic applications, potentially hindering receiver performance enough to compromise a lock and stop signal tracking. Amplitude scintillation degrades signal quality, while phase scintillation affects the carrier tracking loop so that a wider bandwidth is required due to higher carrier dynamics. However, scintillation effects can also provide useful geophysical information about the internal structure and dynamics of the atmosphere, as discussed in detail in the following chapters.

Scintillations are the result of TEC irregularities, principally in the F-layer. Scintillation increases during a solar maximum period due to a higher background TEC. The amplitude of irregularities does not change much as a result of the solar activity, but the background TEC can easily become as much as 10 times higher. In a quiet

year, with a monthly sun-spot number below 30, scintillation may not be observed at all, while the scintillation generated during high solar activity years may severely compromise GNSS signals. Signal fading can be as much as 7dB for 10% of the time, and 25 dB in isolated spikes in low- and mid-latitudes at L1 frequencies. During a worst case solar maximum scenario, L-band fading at low latitudes (±15°) in the plume areas can easily reach 20 dB.

Scintillation is caused by wave scattering and the mechanism depends on the size of the irregularities causing the effect relative to the Fresnel zone. The Fresnel zone length is the fundamental length scale when diffraction effects are significant, defined as follows:

$$l_F = \sqrt{\lambda H} \tag{2.7}$$

when λ is wavelength and H is distance from the Fresnel zone to a receiver . The Fresnel length establishes the scale at which irregularities produce amplitude scintillation with a receiver at distances greater than H. Structures larger than this contribute directly to phase, because Fresnel filtering suppresses their contribution to amplitude.

The following index is related to signal intensity and can be used to express a quantitative value for amplitude scintillation:

$$S_4 = \sqrt{\frac{\langle I^2 \rangle - \langle I \rangle^2}{\langle I \rangle^2}} \tag{2.8}$$

The S4 index gives root mean square deviation of intensity I, normalized to mean intensity, while the σ_ϕ index is used to define phase scintillation and represents the standard deviation of the detrended phase of the carrier frequency, over a given interval. A period of 60 seconds is normally applied to define amplitude and phase indices .

The underlying physics of equatorial scintillation can be explained schematically as follows. Rising bubbles of low electron density are contained in plume-like structures or funnels. If the bubble sizes are greater than the Fresnel zone as observed from the ground station, then the signal is refracted. Instead diffraction occurs if the sizes of the irregularities are equal to or smaller than the Fresnel zone. Moving bubbles generate minor irregularities, with sizes within the range of a few centimetres, which in turn cause scintillation by diffraction.

2.2 HF radar for ionospheric vertical soundings

Each ionospheric layer has a different electron density maximum and thus its own critical frequency. Since the layer maxima increase progressively with altitude, a simple experiment can be designed to identify the critical frequencies and heights of each layer. If a pulse of electromagnetic energy is fired vertically into the ionosphere, initially a low (carrier) frequency, the pulse will be "reflected" off the lower portion of the E layer (the D region generally does not have enough ionization to cause refraction and so is ignored). As the frequency in increased, the pulse will be reflected from higher in the E layer until the E layer critical frequency is reached. Any further increase in frequency will cause the pulse to penetrate right through the E layer, and until reflected from the lower portion of the F_1 layer, where the electron density is similar to the E layer maximum. Continuing to increase frequency will cause the pulse to penetrate further into the F_1 layer before being reflected, until the critical frequency of the F_1 layer is reached. Beyond this the pulse will completely penetrate the F_1 layer and be reflected from the F_2 layer at the level where the electron density is similar to the F_1 maximum. A further increase in frequency will cause the pulse to be reflected from higher up in the F_2 layer until, once again, its critical frequency is reached, after which the pulse passes through the F_2 layer with no further possibility of being reflected back to Earth. Figure 10 represents this sequence schematically. This experiment is known as ionospheric sounding and the instrument used to carry it out is called an *ionosonde*. The graphic representation of the results is usually called an *ionogram.*

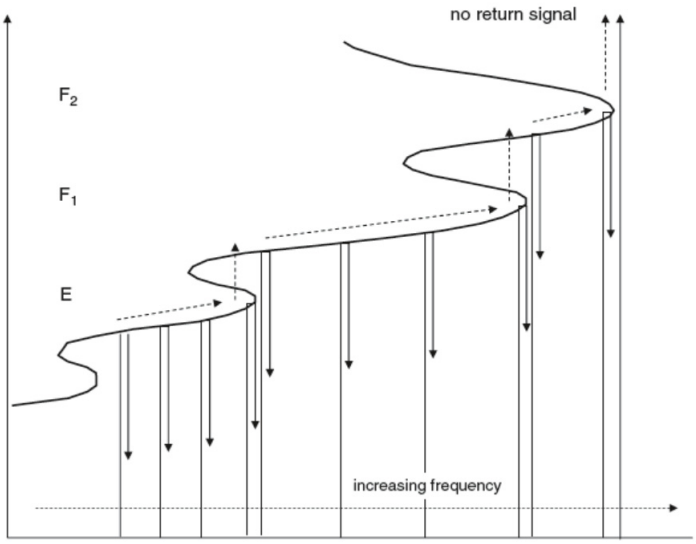

Figure 10. Schematic representation of a ionosonde experiment. From "Radio Wave Propagation. An Introduction for the Non-Specialist", Richard

Figure 11 shows predicted results and a stylised set of what actual results might resemble. The latter diverge significantly from the predicted values near the critical frequencies, where the layer heights also tend towards infinity. Height measurements are indicated as *virtual* heights.

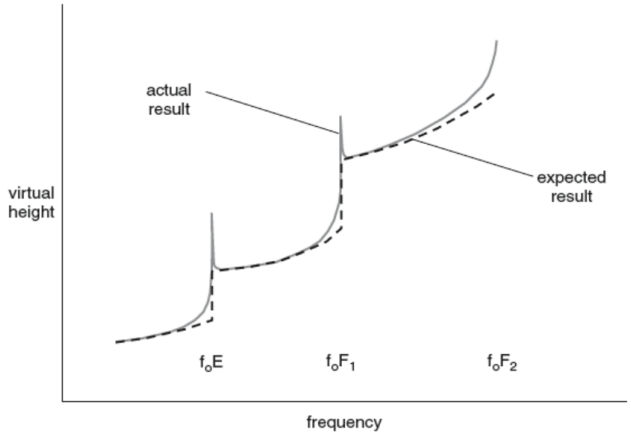

Figure 11. Expected vs actual results of an ionosonde experiment. From "Radio Wave Propagation. An Introduction for the Non-Specialist", Richard

2.2.1 The virtual height of an ionospheric layer

In order to establish the speed of a wave travelling on the surface of the ocean or an electromagnetic wave, it is sufficient to lock on to a point of constant phase and observe how fast the point moves. A continuous sinusoidal waveform, represented by cos θ , is travelling if:

$$\theta = \omega t - \beta z \tag{2.9}$$

in which z is the spatial coordinate and β is the phase constant of the wave, given by

$$\beta = \omega\sqrt{\mu\varepsilon} \tag{2.10}$$

By setting θ=constant, the velocity of the wave is:

$$v_{phase} = \frac{\partial z}{\partial t} = \frac{\omega}{\beta} = \frac{1}{\sqrt{\mu\varepsilon}} \tag{2.11}$$

This is referred to as the *phase velocity* since this is the observed speed of movement of a point of constant phase. A continuous sinusoidal wave carries no information and has no time reference points or markers that could be used in an ionosonde experiment. The wave needs to be modulated before it is useful for a time delay experiment of this type. Measuring the time taken by a pulse from transmission to reception makes it possible to gauge the height of the reflecting layer. It should be noted that the modulated pulse does not necessarily travel at the phase velocity and first the velocity of the modulation envelope must be established. Processing pulse modulation is unnecessarily complicated and the required theory can be derived from one

of the simplest of all modulations, a double side band suppressed carrier (DSBSC). DSBSC signals exhibit just two side bands, one above and one below the carrier frequency. When travelling, this can be expressed as

$$\cos\left(\omega_1 t-\beta_1 z\right)+\cos\left(\omega_2 t-\beta_2 z\right) \tag{2.12}$$

That can be written as:

$$2\cos\left(\omega_0 t-\beta z\right)\cos\left(\Delta\omega t-\Delta\beta z\right) \tag{2.13}$$

Where

$$\omega_0=\frac{\omega_1+\omega_2}{2},\beta_0=\frac{\beta_1+\beta_2}{2},\Delta\omega=\frac{\omega_1-\omega_2}{2},\Delta\beta=\frac{\beta_1-\beta_2}{2} \tag{2.14}$$

The second term in (2.13) (2.13) is the modulation carrying the information. If a point of constant phase in chosen on the modulation envelope then it can be seen that the speed at which the modulation travels is given by

$$v_{group}=\frac{\partial z}{\partial t}=\frac{\partial\omega}{\partial t} \tag{2.15}$$

That is the group velocity.

These two velocity can be expressed in terms of the refractive index as:

$$v_{phase}=\frac{c}{n},v_{group}=nc \tag{2.16}$$

Although these results were derived for DSBSC, they can nevertheless by applied to any modulation. The results shown in Figure 11 can now be interpreted by noting that as frequency approaches the critical frequency of a layer, with the pulse penetrating ever further into the layer, the refractive index is seen to fall.; Equation (2.16) shows that this causes pulse modulation to drop below the speed of light, the empty space value. The critical frequency occurs at the electron density maximum and here the refractive index is zero, implying that the pulse velocity also falls to zero. Consequently, whenever the delay between transmission and reception of a pulse is used to try and establish the height of an ionospheric layer, the height will be overestimated if the assumption is made that the signal travels at the speed of light (as radio waves do in outer space), which is why this measurement is referred to as *virtual height*. The height appears to be infinite at the critical frequency because the group velocity approaches zero.

2.2.2 *Vertical ionograms*

A typical ionogram recorded at a mid-latitude ionospheric station is shown in Figure 12. An ionogram records ionospheric conditions in terms of the relationship between a vertically emitted radio frequency and the virtual heights of echoes reflected from the ionosphere. The frequency range normally extends from about 1 to 20 MHz and the height range extends from 100 to 800 km. When the frequency range is near to the highest plasma frequency of the ionospheric layers, a split is observed in the radio echoes producing two traces, called the ordinary and extraordinary components and corresponding respectively to lower and higher frequency traces, separated by about half the electron gyro-frequency as a result of the influence of the geomagnetic field. At the critical frequencies of the ionospheric layers, the virtual height tends towards infinite, as already described above. For example, the ordinary wave critical frequency of the F2 layer, and the extraordinary wave critical frequency of the F1 layer are represented by f_oF2 and fxF1 respectively.

Ionogram height scales are marked on the assumption that radio waves propagate at the speed of light in the ionosphere,. while in reality they propagate more slowly in an ionized medium like the ionosphere. The recorded heights thus always tend to be higher than the real values and are referred to as virtual heights (*h'*), indicated as *h'*E, *h'*F etc. layer by layer.

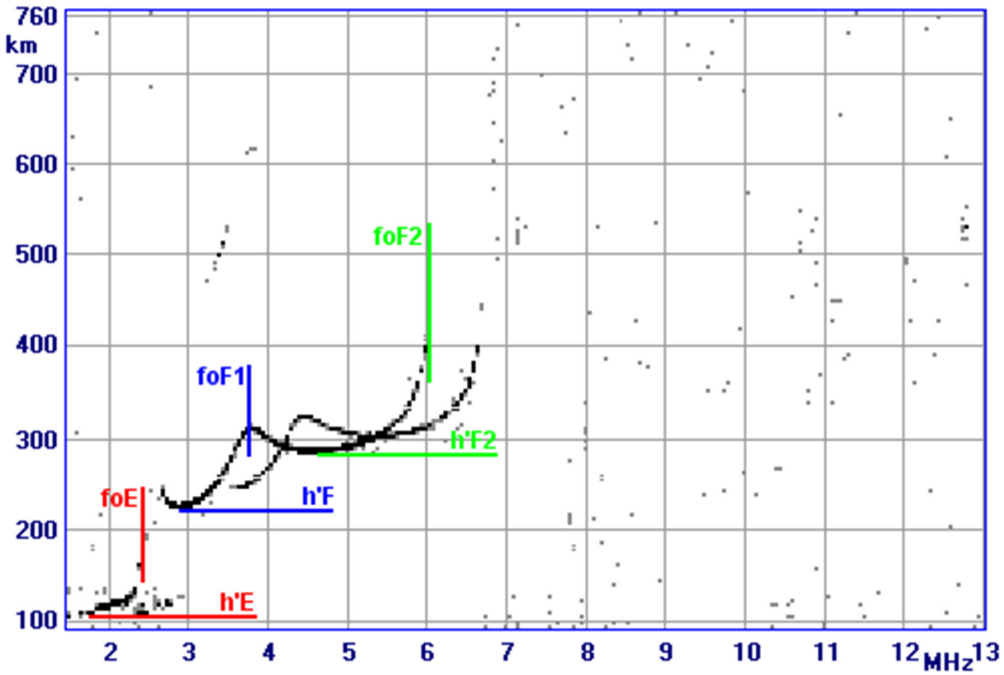

Figure 12. Typical ionograms registered by AIS-INGV ionosonde installed in Rome.

An experienced operator can use ionograms to establish the most important ionospheric parameters, these being the critical frequency of the F2 layer (f_oF2), and the Maximum Usable Frequency at a distance of 3000 km (MUF(3000)F2). In recent decades efforts have been made to develop software for the real time scaling

of ionograms In response to growing interest in real time mapping and short term forecasting. One example of a widely used and well tested automatic scaling program is the ARTIST system, developed at the University of Lowell, Center for Atmospheric Research.

2.2.3 *Autoscala: software for automatic interpretation of the vertical ionograms*

The INGV computer program AUTOSCALA implements an image recognition technique and does not require polarization information for operation, making it suitable for use with both single and crossed antenna systems. A maximum contrast technique is applied to a family of typical F2 layer shape functions and the nearest match is selected as representative of the current F2 layer trace. The vertical asymptote of the selected function represents the critical frequency f_oF2 and the MUF(3000)F2 is established numerically, defining the tangential transmission curve to the selected function. The latest version of the INGV software introduces some important improvements.

1) Redesign of the main routine, reducing CPU footprint, and girofrequency parameterizing so that this version can scale ionograms recorded at any location.

2) It is not possible to scale the required ionospheric values (MUF(3000)F2 and f_oF 2) in a significant proportion of ionograms for a variety of causes. These are well established and categorized in International Union of radio science (URSI) standards. The most frequent causes are:.

a) Blanketing by the E sporadic layer prevents observation of an F2 trace, when the URSI standard recommends using the descriptive letter A on bulletins to substitute the value of the ionospheric f_oF2 parameter.

b) The trace proximal to the critical frequency is not recorded clearly for various reasons, when the URSI standard recommends scaling the most probable f_oF2 value by extrapolation, extending the traces hypothetically to the most likely critical frequency value. For extrapolated frequency ranges greater than 10%, the standard recommends reporting the highest recorded trace frequency followed by the qualifying letter D (greater than) and the appropriate descriptive letter explaining why the trace is unclearly defined (S interference, R absorption, C equipment). AUTOSCALA recognizes the trace and outputs both parameter values. In the latest version a method has been introduced and tested for identifying ionograms carrying insufficient information. This improvement means that ionograms assessed as lacking information are discarded by the program without generating any f_oF2 or MUF(3000)F2 data.

2.2.4 *Adaptive Ionospheric Profiler (AIP)*

The potential of the AUTOSCALA software was recently extended by the INGV team with the development of an algorithm for automatically estimating the electron density profile and adjusting the model parameters

according to ionogram readings. Other computer programs start from a scaled (manual or auto) ionogram trace, $h(f)$, and then derive a frequency profile for the plasma from the first frequency up to f_oF2. The new version of AUTOSCALA derives a limited number of parameters from an ionogram rather than a whole trace, and then surveys a range of possible versions to establish the profile that best matches the scaled parameters. The applied model is based on existing electron concentration models, which apply mathematical expressions to generate a profile based on ionospheric parameters scaled from ionograms. Figure 13 shows a diagram of the applied electron density profile model, which can be divided into two regions:

1. The bottom-side F_2 profile, through the F_1 layer to the top of the E valley (Figure 13, from A to C);
2. The E valley and the E bottom-side (Figure 13, from C to F)

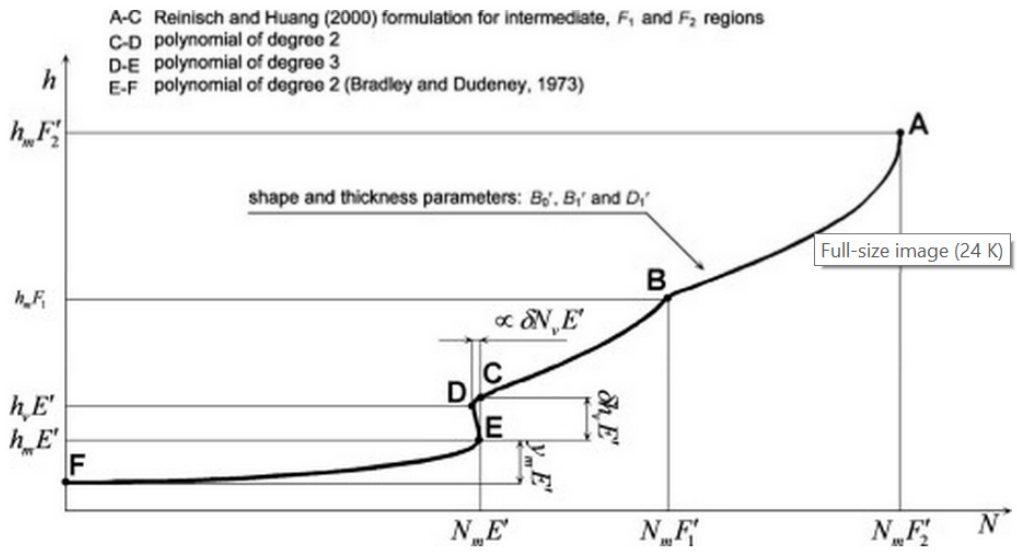

Figure 13. The electron density model used in the INGV profiler(Scotto, 2009).

The models described above for the F_2–F_1 layer and E region can be used to construct an electron density profile with 12 free parameters (6 related to the E region and 6 to the F_2– F_1 layers). These 12 parameters are reported in Figure 13, and include:

1. N_mF'2 maximum electron density of F2 layer
2. h_mF'2 height of maximum electron density of F2 layer
3. N_mF'1 maximum electron density of F1 layer
4. B'$_0$ thickness parameter
5. B'$_1$ shape parameter

6. D'_1 shape parameter
7. N_mE' maximum electron density of E layer
8. h_mE' height of maximum electron density of E layer
9. h_vE' height of E valley point
10. δ h_vE' E valley width
11. δ N_vE' E valley depth
12. y_mE' parabolic E layer semi-thickness

A flow chart of the algorithm is presented in Figure 14. An electron density profile is calculated from a model and this profile is then used to compute a simulated ionogram. The model parameters p are varied into appropriate Δp ranges centred in the vicinity of certain p_{base} values, referred to as "base values" and modelled on the basis of the input data (external conditions parameters, geographic and geomagnetic coordinates of the station, f_oF2 and M(3000)F2). This provides a wide set of profiles, which in turn generate a corresponding set of simulated ionograms, from among which the algorithm selects the ionogram that most resembles the recorded one. A range of variation must be selected for each p parameter also in consideration of the available computer resources. Generally speaking, the efficiency of the adjustment procedure is directly proportional to the variation range of the parameter, which in turn in directly proportional to computation time. The comparison between calculated and real ionograms represents the most critical phase for the algorithm and the choice of method has a marked effect on performance and computation time.

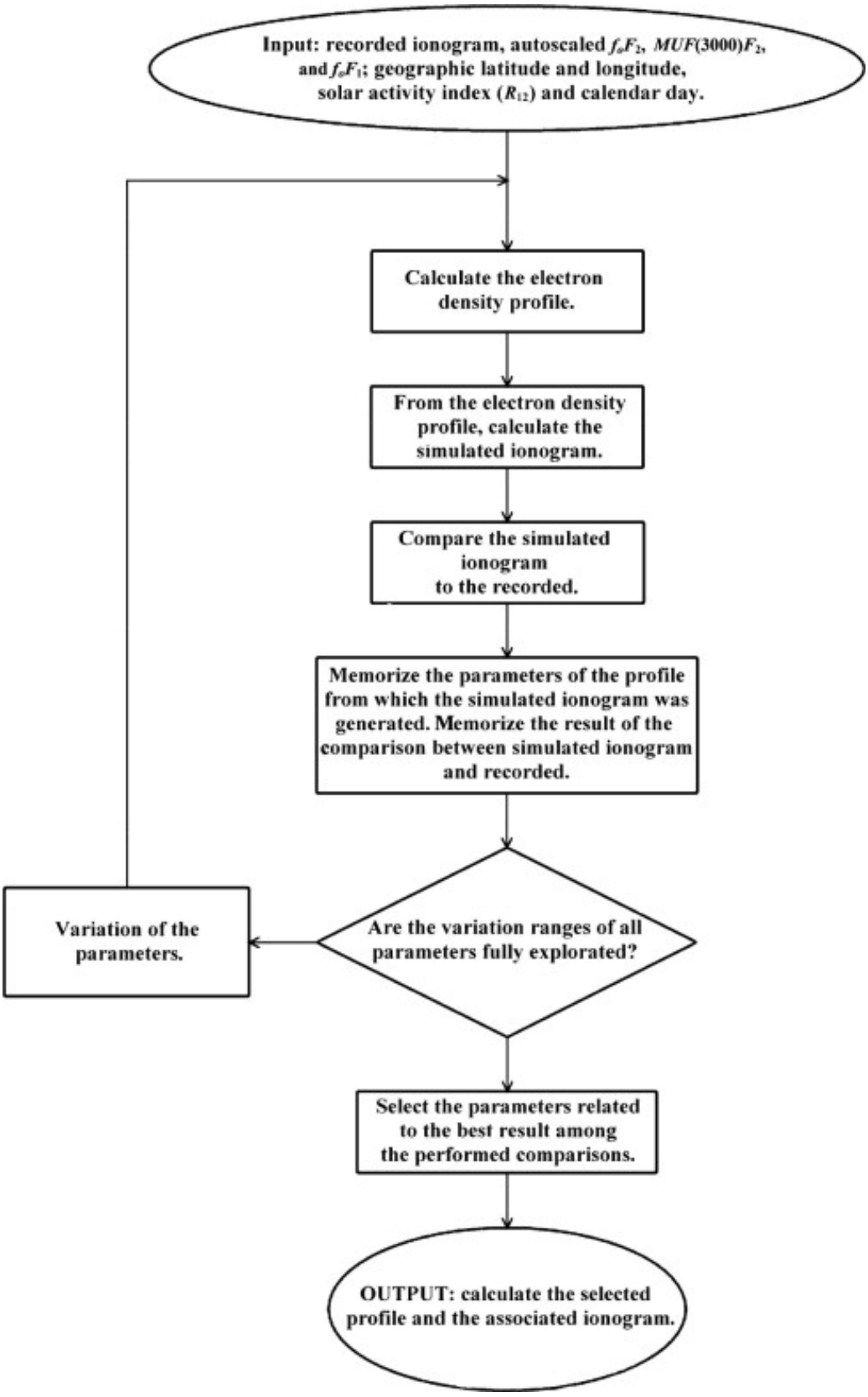

Figure 14. Bloch diagram representing the work flow of the AIP (Scotto, 2009).

2.3 NeQuick model for ionospheric electron content

The NeQuick ionospheric electron density model was developed at the Aeronomy and Radiopropagation Laboratory of The Abdus Salam International Centre for Theoretical Physics (ICTP), in Trieste, Italy, and at the Institute for Geophysics, Astrophysics and Meteorology (IGAM) of the University of Graz, Austria. The evolution of NeQuick can be traced back to the DGR profiler proposed by Di Giovanni and Radicella in 1990 and modified by Radicella and Zhang in 1995. The European Space Agency (ESA) European Geostationary Navigation Overlay Service (EGNOS) project for assessment analysis implemented the original version of this model for single-frequency positioning applications within the framework of the European Galileo project. The International Telecommunication Union, Radiocommunication Sector (ITU-R) also adopted it as a suitable method for TEC modelling. The source code for NeQuick (FORTRAN 77) is available at http://www.itu.int/ITU-R/. There has been significant work to improve the analytical formulation of NeQuick and to exploit the growing availability of data with continuous updating of the model. Specific modifications were made in response to the need to better represent the median ionosphere on a global scale. The bottomside and topside modelling descriptions have recently been subject to major changes. Specific revisions have also been introduced in the computer package associated with the NeQuick model to improve its computational efficiency. The main features of NeQuick2 are outlined below but first it is useful to recall the Epstein function expression that underlies the model formulation:

$$N_{Epstein}(\mathrm{h},\mathrm{h}_{\max},\mathrm{N}_{\max},\mathrm{B}) = \frac{4N_{\max}}{\left(1+\exp\left(\frac{h-h_{\max}}{B}\right)\right)^2}\exp\left(\frac{h-h_{\max}}{B}\right) \tag{2.17}$$

2.3.1 *Bottomside ionosphere modelling*

Considering the well-known expressions relating maximum electron density and critical frequency (in 10^{11} m^{-3}) for each ionospheric layer $NmE = 0.124(foE)^2$, $NmF1 = 0.124(foF1)^2$, $NmF2 = 0.124(foF2)^2$, h_mE, h_mF1, h_mF2 for the E, F1 and F2 layer peak heights (in km), respectively, and BE, B1, B2 for the E, F1 and F2 layer thickness parameters (in km), respectively, it is possible to express the NeQuick 2 bottomside as a sum of semi-Epstein layers as follows:

$$N_{bot}(\mathrm{h}) = N_E(\mathrm{h}) + N_{F1}(\mathrm{h}) + N_{F2}(\mathrm{h}) \tag{2.18}$$

Where:

$$N_E(\mathrm{h}) = \frac{4N_mE*}{\left(1+\exp\left(\frac{h-h_mE}{B_E}\xi(\mathrm{h})\right)\right)^2}\exp\left(\frac{h-h_mE}{B_E}\xi(\mathrm{h})\right) \tag{2.19}$$

$$N_{F1}(\mathrm{h}) = \frac{4N_mF1^*}{\left(1+\exp\left(\frac{h-h_mF1}{B_{F1}}\xi(\mathrm{h})\right)\right)^2}\exp\left(\frac{h-h_mF1}{B_{F1}}\xi(\mathrm{h})\right) \tag{2.20}$$

$$N_{F2}(\mathrm{h}) = \frac{4N_mF2}{\left(1+\exp\left(\frac{h-h_mF2}{B_{F2}}\right)\right)^2}\exp\left(\frac{h-h_mF2}{B_{F2}}\right) \tag{2.21}$$

In which:

$$N_mE^* = N_mE - N_{F1}(\mathrm{h}_m\mathrm{E}) - \mathrm{N}_{F2}(\mathrm{h}_m\mathrm{E}) \tag{2.22}$$

$$N_mF1^* = N_mF1 - N_E(\mathrm{h}_m\mathrm{F1}) - \mathrm{N}_{F2}(\mathrm{h}_m\mathrm{F1}) \tag{2.23}$$

and

$$\xi(\mathrm{h}) = \exp\left(\frac{10}{1+1|h-h_mF2|}\right) \tag{2.24}$$

Is a function to smooth the E and F1 curve near the F2 peak.

2.3.2 Topside ionosphere modelling

The model topside is represented by a semi-Epstein layer with a height-dependent thickness parameter H, described as follow:

$$N(\mathrm{h}) = \frac{4N_mF2}{(1+\exp(z))^2}\exp(z) \tag{2.25}$$

With:

$$z = \frac{h-h_mF2}{H} \tag{2.26}$$

$$H = H_0\left[1+\frac{rg(h-h_mF2)}{rH_0+g(h-h_mF2)}\right] \tag{2.27}$$

And the constant $r = 100$ and $g = 0.125$ used to drive the change of the parameter H.

The parameters applied to compute density profiles are all calculated from well-known equations, widely available in scientific literature. The two main parameters f_oF2 and M(3000)F2 (also used to conduct validation as discussed in chapter 5) are determined by the NeQuick model using the ITU-R (previously called

CCIR,1967) coefficients. An important detail is that, in order to compute f_oF2 and M(3000)F2 for a given location, the modip for the location must be known in advance. A set of 12 files are thus included in the NeQuick package, each containing the f_oF2 and M(3000)F2 coefficients for one month, along with a file containing modip values over a worldwide grid spaced by 5° in latitude and 10° in longitude. The NeQuick2 program includes all the specific functions and interpolation routines required to establish the necessary parameter values from these files.

.

2.4 References

As for the first chapter, the second one collects some well known information about different way to probe the ionosphere so it does not require a detailed bibliography. Main sources of what reported in this chapter are listed below.

Nava, B., Coïsson, P. and Radicella, S. M.: A new version of the NeQuick ionosphere electron density model, J. Atmos. Solar-Terrestrial Phys., 70, 1856–1862, doi:10.1016/j.jastp.2008.01.015, 2008.

Petrovski, I. and Tsujii, T.: Digital satellite navigation and geophysics: A practical guide with {GNSS} signal simulator and receiver laboratory, Cambridge University Press. [online] Available from: http://books.google.co.cr/books?id=y2z8q-sfL9YC&printsec=frontcover&dq=gnss&hl=es-419&sa=X&ei=IxvrUMKBM4H49gTd7YCwBw&ved=0CFoQ6AEwBw (Accessed 18 February 2015), 2012.

Pezzopane, M. and Scotto, C.: Automatic scaling of critical frequency f_oF2 and MUF(3000)F2: A comparison between autoscala and artist 4.5 on rome data, Radio Sci., 42(4), n/a–n/a, doi:10.1029/2006RS003581, 2007.

Richards, J. a.: Radio wave propagation: An introduction for the non-specialist, Springer Science & Business Media., 2008.

Scotto, C.: Electron density profile calculation technique for Autoscala ionogram analysis, Adv. Sp. Res., 44(6), 756–766, doi:10.1016/j.asr.2009.04.037, 2009.

3. TEC gradients and scintillation climatology over Brazil

Global Navigation Satellite Systems (GNSS) provide all-weather continuous Position, Navigation and Time (PNT) information worldwide. Nowadays, GNSS allows to measure position with accuracy from few meters to few centimetres depending on the variables and the method used (Dow et al., 2009). GNSS has now become essential to a wide range of industrial applications from construction and surveying to aviation and precision agriculture. Furthermore, satellite system applications permit to study physical phenomena in different fields of Earth sciences (space geodesy and glaciology, seismic and volcano activity monitoring, tsunami hazard, atmospheric remote sensing etc.) (Bevis et al., 1992; Blewitt et al., 2006; Frezzotti et al., 1998; Larson, 2009; Shimada et al., 1990).

Space weather conditions have a great influence on GNSS integrity, accuracy and availability as the ionosphere is the largest contributor to the error budget for single frequency GNSS receivers. Trans-ionospheric signals propagating from satellites to ground-based receivers pass through an ionized medium with a phase refractive index less than unit and a group refractive index greater than unit resulting in an "advance" in the phase of carrier component and a "group delay" of the code component. Such effect is in general properly taken into account in modern GNSS data processing and positioning can be corrected against it. Other meaningful effects induced by the ionospheric plasma dynamics on satellite signals can be divided into two different groups: (a) distortion caused by a large spatial and temporal scale fluctuation of the ionospheric plasma density and (b) rapid fluctuations of signal phase and amplitude due to small scale structures of plasma inhomogeneity. The former is strictly related to diurnal and seasonal variations of ionospheric morphology as well as 11-yr solar cycles. When solar activity increases reaching its maximum, the influence of Sun radiation and particle flux increase resulting on a great variability in space and time of the plasma density. In particular, solar maximum is associated with increase of solar flares and coronal mass ejections that causes temporarily intense disturbances of Earth's magnetosphere and ionosphere, as for instance during the severe storm in October 2003, exhaustively studied in the recent past (Doherty et al., 2004; De Franceschi et al., 2008; Mitchell et al., 2005; Muella et al., 2010). Effects on the ionosphere due to the seasonal and diurnal variability are well known and quite easily modelled. Nevertheless, the influence of the Sun activity is often sudden and the effect at ground level is hard to predict, due to the complexity of the coupling between the solar wind, the magnetosphere and the ionosphere. The inhomogeneity of ionospheric electron distribution can cause irregular fluctuations of the amplitude and phase of the received signals referred to as "ionospheric scintillation" (Crane, 1977; Rama Rao et al., 2006; Rino and Livingston, 1982).

Scintillation can cause degradation on both pseudorange and phase measurements and, in the worst case, can lead to signal loss of lock, bedevilling the availability of the service and the precise positioning for a time extent that could last from minutes to several hours. Amplitude scintillation is traditionally monitored by means of the S4 index, which is the standard deviation of the received power normalized by its mean value,

whereas phase scintillation is monitored by the σφ index, which is the standard deviation of the detrended carrier phase. In modern, high sampling frequency (50 Hz) receivers for scintillation monitoring, the time intervals in which such indices are calculated are of 60 seconds for S4 and 1, 3, 10, 30 and 60 seconds for σφ.

Because of the morphology of the geomagnetic field, the geographic regions mainly affected by scintillations are the polar and the equatorial areas. The scintillation-driving irregularities in the those regions are formed through different mechanisms: at high latitudes they are mainly driven by magnetospheric phenomena associated with storm events, while at low latitudes the so-called "fountain effect", due to the interplay between ExB drift, gravity and pressure gradients, leads to the formation of the Equatorial Plasma Bubbles (EPBs). This phenomenon is also known as Equatorial Ionospheric Anomaly (EIA) and occurs in a band of ≈±20° around the geomagnetic equator. Although several studies have been carried out, neither the mechanisms producing equatorial scintillation nor its morphology are yet fully understood. This work aims to contribute to the understanding of the relationship between the ionospheric plasma irregularities and the scintillations production. Since the 1950's several studies (Koster, 1972; Muella et al., 2013; Yeh and Swenson, 1959) report that equatorial scintillations are mainly night-time events that occur in particular during the post-sunset period and that the fluctuations of plasma density producing scintillations occur at altitudes from 200 to 400 km (F region peak altitude). A recent paper by Chatterjee and Chakraborty (2013) shows that intensity of amplitude scintillations is controlled not only by the intensity of the irregularities but also by background electron density and its distribution in the ionosphere. In fact, during solar maximum the intensity of variations in plasma density does not increase whereas background electron density undergoes increasing by a factor of up to 10 near the Equatorial Ionization Anomaly (EIA) crests resulting in intense scintillation activity. The ionosphere over South America, and in particular over Brazil, is of great interest not only for the presence of the EIA but also for the important role played by the South Atlantic Magnetic Anomaly (SAMA). In the SAMA zone, the magnetic field strength being almost half of what it is when compared to other regions, a large amount of high energy particles penetrates into the ionosphere, influencing the sunset electrodynamics processes responsible for the EPB irregularity generation and related dynamics (zonal and vertical drifts etc.)(Abdu et al., 2005). Therefore SAMA represents a source of significant longitudinal variability in the global description of scintillation in the equatorial ionosphere.

This work is focused on the analysis of ionospheric scintillation over the São Paulo state region (Brazil), aiming to catch its relationship with ionospheric plasma irregularities, also taking into account the spatial and temporal distributions of the total electron content (TEC) derived by GNSS measurements carried out over the whole of year 2012. The study is performed in two manifold directions:

- Study of some case studies occurred during the 2012.

- Climatological analysis of the TEC and scintillations by means of Ground Based Scintillation Climatology (GBSC), a technique described in (Alfonsi et al., 2011; Spogli et al., 2009) and briefly recalls in the next sections.

This approach permits to highlight different aspects of the mechanism that lead to the genesis of the scintillations. TEC, estimated from São Paulo State University (UNESP) Real Time Kinematic Network (URTKN) observations, are used to create very resolute regional maps, by interpolating data over a regular grid. The crucial aspect of the data treatment is the calibration of TEC values inferred by GNSS code and phase carrier delays (Ciraolo et al. 2007). In order to obtain TEC absolute values it is necessary to estimate different offsets introduced by satellites and receivers clock errors, phase ambiguity and cycle slips. Calibrated TEC measurements are used to estimate spatial variations of TEC and then create maps of calibrated TEC gradients along geographical North-South and East-West directions. Scintillation activity is investigated by using one PolaRxS, a multi-frequency, multi-constellation receiver installed at Presidente Prudente (PRU2, 22.12° S, 51.41° W) as part of the network deployed in the framework of the CIGALA (Concept for Ionospheric Scintillation mitigation for professional GNSS in Latin America) project (http://cigala.galileoic.org/).

3.1 Data and methods

3.1.1 URTKN and CIGALA networks

The UNESP Real Time Kinematic Network (URTKN) is the densest GNSS active network in South America consisting of 13 GNSS stations providing real time data. Each station provides L1, C1, L2, P2 delay data every 15 seconds by means of multi-constellations (GPS+GLONASS) GNSS receivers (for more information about the receivers see http://www.fct.unesp.br/#!/pesquisa/grupos-de-estudo-e-pesquisa/gege//gnss-sp-network2789/). All data are freely available from IBGE (Istituto Brasileiro de Geografia e Estatistica) ftp server in Receiver Independent Exchange (RINEX) observational file format. Table 1 describes the 11 stations used to calculate the TEC during the whole of 2012. Out of the whole network, data from two of the stations (ROSA and UBA1) were not available in the period involved in this study or were too noisy for the purpose of this work. The region of São Paulo state is a very interesting area to investigate ionospheric phenomena because of its geomagnetic position: near the southern crest of EIA and close to the SAMA. Figure 15 shows the location of the URTKN stations in São Paulo state region (red placemarks) and CIGALA PRU2 scintillation monitoring station in Presidente Prudente (concentric black and white circles). In the same figure, the red curve identifies the magnetic equator and the isolines represent the total intensity of the geomagnetic field (F) calculated by the spherical harmonics expansion up to the 13th order with IGRF-11 coefficients (Finlay et al., 2010). GNSS stations used for this work (red placemarks in Fig. 1) cover an area close to the minimum of the magnetic field intensity inside the SAMA anomaly $(F \sim 23000\ nT)$.

Table 1. List of the URTKN stations used to compute TEC values. For each station location, station code and geographic coordinates are reported.

Location	Station Code	Lat.	Lon.
Araçatuba	SPAR	-21°11'	-50°26'
Campinas	SPCA	-22°48'	-47°03'
Cananéia	NEIA	-25°01'	-47°55'
Ourinhos	OURI	-22°56'	-49°53'
Presidente Prudente	PPTE	-22°07'	-51°24'
São José do Rio Preto	SJRP	-20°47'	-49°21'
São Paulo	POLI	-23°33'	-46°43'
Maringá	PRMA	-23°24’	-51°56’
Curitiba	UFPR	-25°27’	-49°14’
Varginha/Cemig	MGVA	-21°32'	-45°26'
Inconfidentes	MGIN	-22°19'	-46°19'

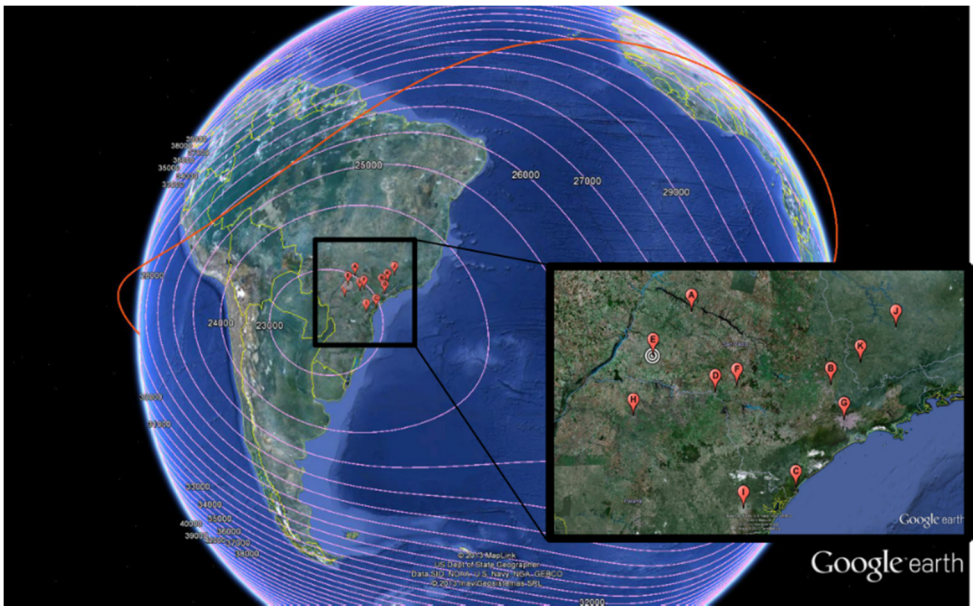

Figure 15.The URTKN stations in São Paulo state region (red placemarks) and PRU2 scintillation receiver (black and white concentric circles). The dark red line indicates the magnetic equator and the light red lines represent the isolines of the total intensity of the magnetic field. White labels represent the intensity of the field in nT.

Scintillation activity in the region is monitored by the network of PolaRxS receivers deployed in the frame of the CIGALA project shown in and reported in . CIGALA was a project funded by the European Commission under the 7th Framework Program (GALILEO-2008 call) and ended in 2011. The main objective of the project was to develop, validate and implement algorithms in a GNSS receiver, which would increase its robustness to ionospheric scintillation effects and to deploy a network of such receivers in Brazil. The PolaRxS's are multi-frequency, multi-constellation receivers capable of tracking simultaneously GPS L1CA, L1P, L2C, L2P, L5; GLONASS L1CA, L2CA; GALILEO E1, E5a, E5b, E5AltBoc; COMPASS B1, B2; SBAS L1 (Romano and Bougard, 2011). Sampling at 50 Hz, the receivers give the following main output parameters:

1. the σΦ phase scintillation index calculated over different time intervals (1, 3, 10, 30, 60 seconds);
2. the S4 amplitude scintillation index calculated over 60 seconds;
3. the TEC and Rate Of TEC change (ROT) every 15 seconds,
4. the spectral parameters: spectral slope of the phase Power Spectral Density (p) in the 0.1 to 25 Hz range and the spectral strength of the phase power spectrum density (T) at 1 Hz (60 seconds);
5. the Standard Deviation of the Code Carrier (CCSTDDEV - 60 seconds) ;
6. the Carrier to noise ratio, C/n (60 seconds);
7. the locktime (60 seconds).

All these quantities (except TEC and ROT) are calculated for all the available signal frequencies transmitted by the satellites and along the slant path connecting the receiver to the satellite. TEC values are obtained by the pseudorange measurements only. TEC is based on the L2-P and L1-P pseudoranges for GPS; on the L1-C/A and L2-C/A pseudoranges for GLONASS and on the L1BC and E5a for Galileo. ROT is computed from the carrier phase measurements only, and hence is more accurate than TEC.

Table 2. Name, location and geographic coordinates of the receiver forming the CIGALA network.

Name	**Location**	**Lat (°N)**	**Lon (°E)**
POAL	Porto Alegre	-30.07	-51.12
PRU1	Presidente Prudente	-22.12	-51.41
PRU2	Presidente Prudente	-22.12	-51.41
SJCI	Sao Jose dos Campos	-23.21	-45.86
SJCU	Sao Jose dos Campos	-23.21	-45.96

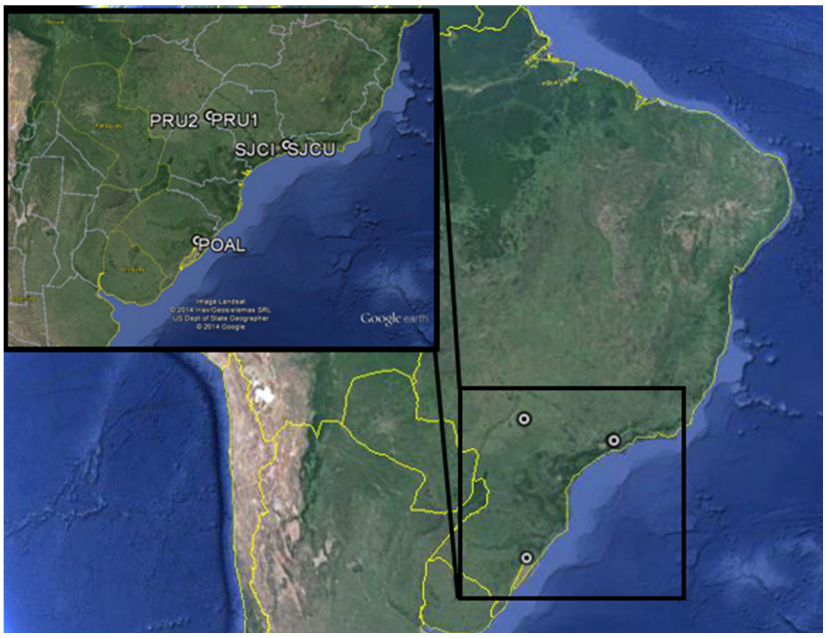

Figure 16. The 5 CIGALA network scintillation receivers. SJCU, SJCI and PRU1, PRU2 are almost co-located.

3.1.2 TEC calibration technique

As mentioned in the introduction, pseudorange and carrier-phase from RINEX files are affected by several frequency independent terms and by a dispersive contribution due to the presence of ionosphere expressed as an excess path:

$$I = \alpha sTEC / f^2 \tag{3.1}$$

where $sTEC$ is the total electron content along the path from satellite to receiver in TEC units (TECu), I is the ionospheric range delay at frequency f and α/f2 is a conversion factor from TECu to length units. Using simultaneous observations at different frequencies it is possible to obtain an observable that is not affected by frequency-independent errors. Subtracting observations L1 and L2 (i.e. referred to GPS carriers) a new observable L_{arc} can be obtained:

$$L_{arc} = sTEC + B_R + B_s + C_{arc} + \varepsilon_L \tag{3.2}$$

where the sub-index "arc" refers to every continuous arch of carrier-phase observations , BR and BS are the biases introduced by receiver and satellite hardware in the carrier-phase observations, C_{arc} is the bias produced by carrier-phase ambiguities in the ionospheric observable and ε_L is the effect of noise and multi-path. Similarly, using dual-frequency code-delay observations (P) another ionospheric observable can be obtained:

$$P = sTEC + b_R + b_s + \varepsilon_P \tag{3.3}$$

where b_R, b_s are the so-called inter frequency biases (IFB) and the other terms are analogous to (3.3). Once L_{arc} and P have been obtained, the average difference between those two observables can be computed for each arc as:

$$\left\langle L_{arc} - P_{arc} \right\rangle = C_{arc} + B_R - b_R + B_s - b_s - \varepsilon_{P\ arc} \tag{3.4}$$

Subtracting this quantity from carrier-phase observation it can be obtained:

$$\tilde{L}_{arc} = STEC + b_R + b_s + \varepsilon_{P\ arc} + \varepsilon_L \tag{3.5}$$

(3.5) represents the carrier-phase ionospheric observable "levelled" to the code-delay ionospheric observable. Note that there is no ambiguity term in code-delay observations and εL can be neglected as described in (Parkinson and Spiker, 1996)

$$\tilde{L}_{i,arc} = STEC + b_R + b_s + \varepsilon_{P\ arc} \tag{3.6}$$

Usually it is assumed that also $\langle \varepsilon_P \rangle_{arc}$ can be disregarded (Mannucci et al., 1998; Parkinson and Spiker, 1996), but considering the co-located stations experiment described in Ciraolo et al. (2007) it is clear that this simple assumption does not work in several situations. This empirical evidence suggests maintaining $\langle \varepsilon_P \rangle_{arc}$ term in (3.6) trying to estimate bias for each arch instead of single biases for receivers and satellites. Eq. (3.6) becomes

$$\tilde{L}_{arc} = STEC + \beta_{arc} \tag{3.7}$$

that is the basic relation used to calibrate the TEC.

In (3.7) β_{arc} is the arc-offset, a constant to be determined for each arc of observations related to a given receiver and satellite pair. β_{arc} represents the contribution of receiver and satellites biases ($b_R + b_s$), and the contribution of any non-zero averaged errors over an arc of observations, e.g. the multipath.

A thin shell (Mannucci et al., 1998) model at 350 km is used to define the mapping function between the slant and vertical TEC. In order to avoid well known errors related to the mapping function (Sekido, 2003) considering global/regional solutions, a single station solution is adopted. For further detailed information about the calibration technique refers to http://cdsagenda5.ictp.trieste.it/askArchive.php?base=agenda&categ=a12180&id=a12180s7t6/lecture_notes

3.1.3 *Calibrated TEC interpolation and spatial gradients.*

By interpolating data obtained from the TEC calibration technique applied to the URTKN measurements, we constructed calibrated TEC maps over the São Paulo state region. We adopt the interpolation method known as natural neighbour interpolation technique (Boissonnat and Cazals, 2002), according to Foster and Evans (2008) in which the authors show that, in the case of local maps of TEC, this technique give better results with respect to other commonly used methods (linear, inverse distance weighting, Kriging etc.)

The natural neighbour interpolation technique is based on the identification of the Voronoi cell associated with a set of scattered points set in the selected area (Okabe et al., 1994). The Voronoi polygons network can be constructed through Delauney triangulation of the data (Lee and Schachter, 1980). For each point where an interpolated value is required, the method operates as follows:

1) Assume that the domain of the data is already divided following the Voronoi criteria.
2) Re-divide the domain to include the output point, thus adding a new Voronoi cell which overlaps the cells of the natural neighbours of the output point (Figure 17).
3) The contribution from each neighbour is given by the ratio of the area of overlap (w_i in Figure 17) to the total area of the new cell.
4) The value associated with the point x is calculated following:

$$F(x,y)=\sum_{i=1}^{N} w_i f_i \tag{3.8}$$

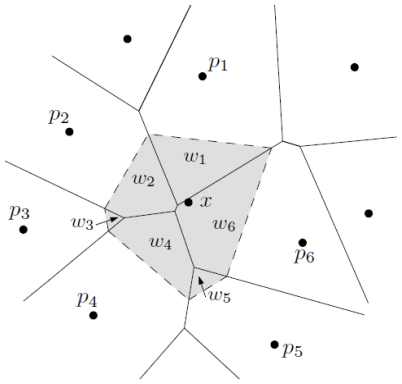

Figure 17. Representation of Voronoi diagrams using to compute value of function in point x. Grey area represents the "stolen" area for the point x.

The interpolation is made to obtain the calibrated TEC on a regular grid, covering the entire region of São Paulo state. An example of the interpolation method applied to the TEC values is given in Figure 18 in which red lines show the tessellation considering only IPP (point 1 in the description above) and blue lines illustrate

tessellations including the output point represented by a red cross in panel b (point 2 in the description). The area inside the red dashed line in the panel b represents the "stolen" area mentioned in point 3 of the description.

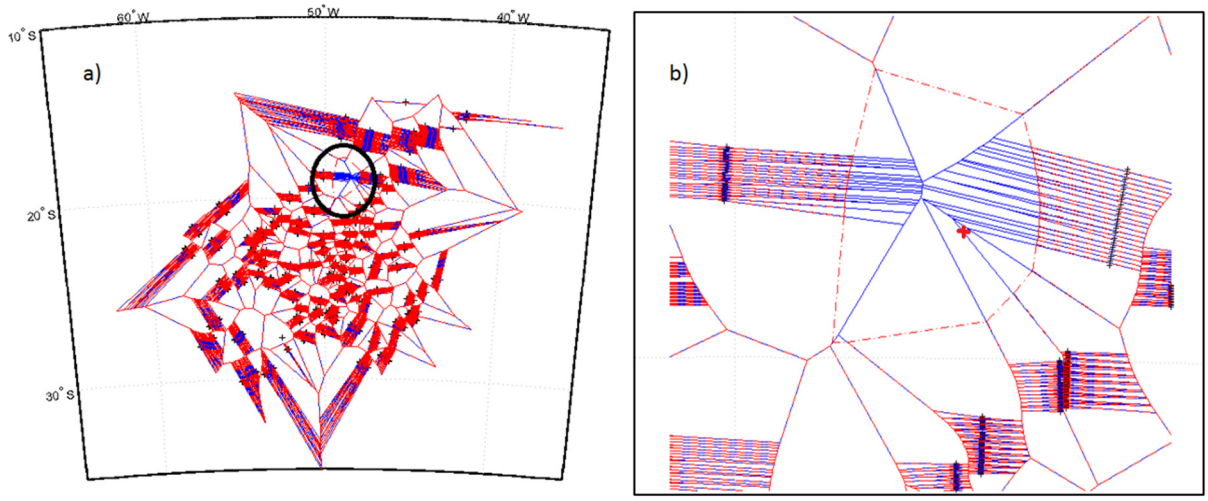

Figure 18.An example of Voronoi tessellation applied on calibrated TEC values retrieved from measurements on 16 February 2012 from 2:00 UT to 2:10 UT (panel a). Red lines show the tessellation considering only IPP, blue lines illustrate tessellations including the output point (red cross). Panel b) show a zoom on the region inside the black circle on panel a). Black crosses represent the IPP. Dashed red line represents the "stolen area" as described in the text.

From the interpolated TEC values over the grid, we calculate the TEC gradients along the North-South direction (ΔTEC_{N-S}) and East-West direction (ΔTEC_{E-W}) by means of the following equation:

$$\Delta TEC_{N-S}\left(GP_{i,j}\right)=\frac{TEC\left(GP_{i+1,j}\right)-TEC\left(GP_{i,j}\right)}{d_i} \tag{3.9}$$

$$\Delta TEC_{E-W}\left(GP_{i,j}\right)=\frac{TEC\left(GP_{i,j+1}\right)-TEC\left(GP_{i,j}\right)}{d_j} \tag{3.10}$$

where $\Delta TEC_{N-S}\left(GP_{i,j}\right)$ is TEC gradient along the North-South direction calculated for the point of the grid with coordinates (i,j), $TEC\left(GP_{i+1,j}\right)$ is the TEC value of the first northerly point of the grid with respect to (i,j), $TEC(GP_{i,j})$ is the TEC value of the considered grid point (i,j) and d_i is the distance between (i+1,j) and

(I,j) points. Analogous terms are used in Eq. (9) in which $TEC(GP_{i,j+1})$ is the easterly point of the grid with respect to (i,j). Symbols are also explained in Figure 19 in which an example of the grid points is given.

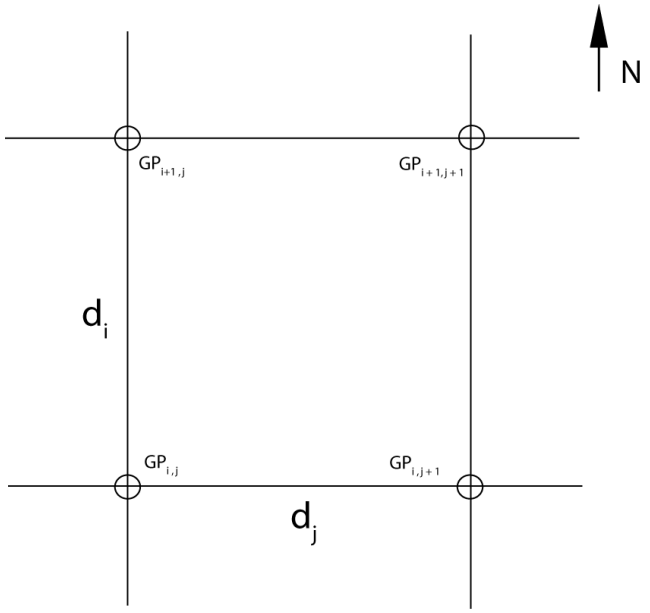

Figure 19. Sketch of the grid used for the computation of TEC gradients useful to explain the equations described in the text. di and dj represent the distance of the grid points in N-S and E-W directions respectively.

3.1.4 Ground based scintillation climatology (GBSC)

Ground based scintillation climatology (GBSC) is a tool developed at INGV (Alfonsi et al., 2011; Spogli et al., 2009) with the aim of highlight climatological features of the ionosphere at low and high latitudes. GBSC take as input the measurements coming from different kind of GNSS receivers to ingest scintillation as well as TEC data. For this study, the technique have been slightly modified to assimilate also data from the interpolation and gradients computation described in the previous section. Dividing the field of view of the receiver (or receivers if available) in bin of the dimension that the user can define, the technique is able to furnish as output different kind of maps relative to the ionospheric parameters considered. Typical output of the GBSC are maps of the mean and standard deviation of S4, σ_{φ} ,TEC and Rate of TEC (ROT) and occurrence maps of the scintillation parameters greater than a chosen threshold. In this work, also maps of calibrated TEC and TEC gradients can be produced. Maps can be visualized in different reference frame such as geographic coordinates, azimuth and elevation etc. The occurrence of a certain parameter above a defined threshold id defined as follow:

$$O(\%) = \frac{N(p > T)}{N_{tot}} \tag{3.11}$$

Where $O(\%)$ is the occurrence in percentage, $N(p > T)$ is the number of measurements in which the parameter p is greater than the threshold T and N_{tot} is the total number of measurements. The The occurrence as well as the mean and standard deviation is computed for each bin separately in order to construct maps covering all the field of view of the receiver.

3.2 Results

3.2.1 Climatological analysis

In order to study the relationship between TEC, its spatial gradients and ionospheric scintillation, data collected during the whole 2012 by the receivers of the URTKN and CIGALA network have been analysed by means of the GBSC technique described in the previous section. Starting from code and carrier phase information recorded in the RINEX files from the 11 stations of the URTKN listed in Table 1, the calibration procedure described above is applied in order to obtain vertical calibrated TEC values for each stations, satellite and epoch. Applying the interpolation and gradients computation technique, the values of the N-S and E-W gradients covering an area between -29° and -15° in latitude and -57° and -40° in longitude are calculated. For what concern the amplitude scintillation index S4, data from the receivers of the CIGALA network are verticalized as described in (Rino, 1979a, 1979b):

$$S_4^{vert} = \frac{S_4^{slant}}{F\left(\alpha_{elev}\right)^b} \tag{3.12}$$

Where S_4^{slant} is the amplitude scintillation index measured along the ray-path from satellite to receiver, i.e. the output of the receiver, b is a coefficient depending on the slope (p) of the signal recorded by the receiver and directly given by the instrument itself:

$$b = \frac{p+1}{4} \tag{3.13}$$

$F(\alpha_{elev})$ is the well-known obliquity factor mentioned in (Mannucci et al., 1998) defined as:

$$F\left(\alpha_{elev}\right) = \frac{1}{\sqrt{1 - \frac{R_e \cos \alpha_{elev}}{R_e + H_{IPP}}}} \tag{3.14}$$

In which α_{elev} is the elevation angle of the satellite, R_e is the radius if the Earth and H_{IPP} is the height of the ionospheric pierce point, here assumed to be 350 km.

Data from the URTKN have been continuously acquired during 2012 while looking at the data from CIGALA network, some gaps can be noted even if, for climatological study, dataset can be considered well distributed during the period. Figure 20 shows the percentage of data available from each station during the year 2012.

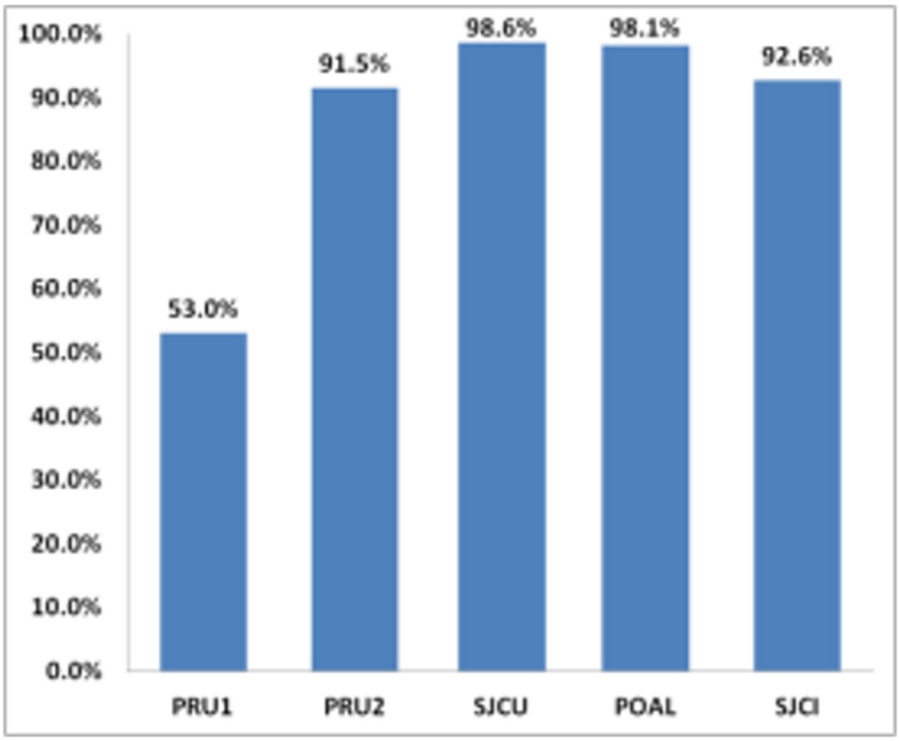

Figure 20. Data availability in percentage for the CIGALA network during the year 2012.

In order to catch the seasonal variation of the ionospheric parameter, the dataset has been divided into 4 different subset according to what described in Table 3.

Table 3. Dataset seasonal selection

Season	Day start	Day end
Summer	21 December	21 March
Winter	21 June	21 September
Spring	21 September	21 December
Fall	21 March	21 June

Figure 21 show the climatological distribution of the electron density during the entire 2012. It can be noted that, for all the 4 seasons, the area with the greater mean TEC is located around 15° S magnetic latitude. This is a clear signature of the southern crest of the EIA. Figure 21 also highlights the seasonal variation of the TEC distribution over the area of São Paolo showing that in fall and spring mean TEC reaches its maximum growing

until 50 TECu. During winter, a minimum of the mean TEC can be noted since the climatological values of the electron density reaches 20 TECu.

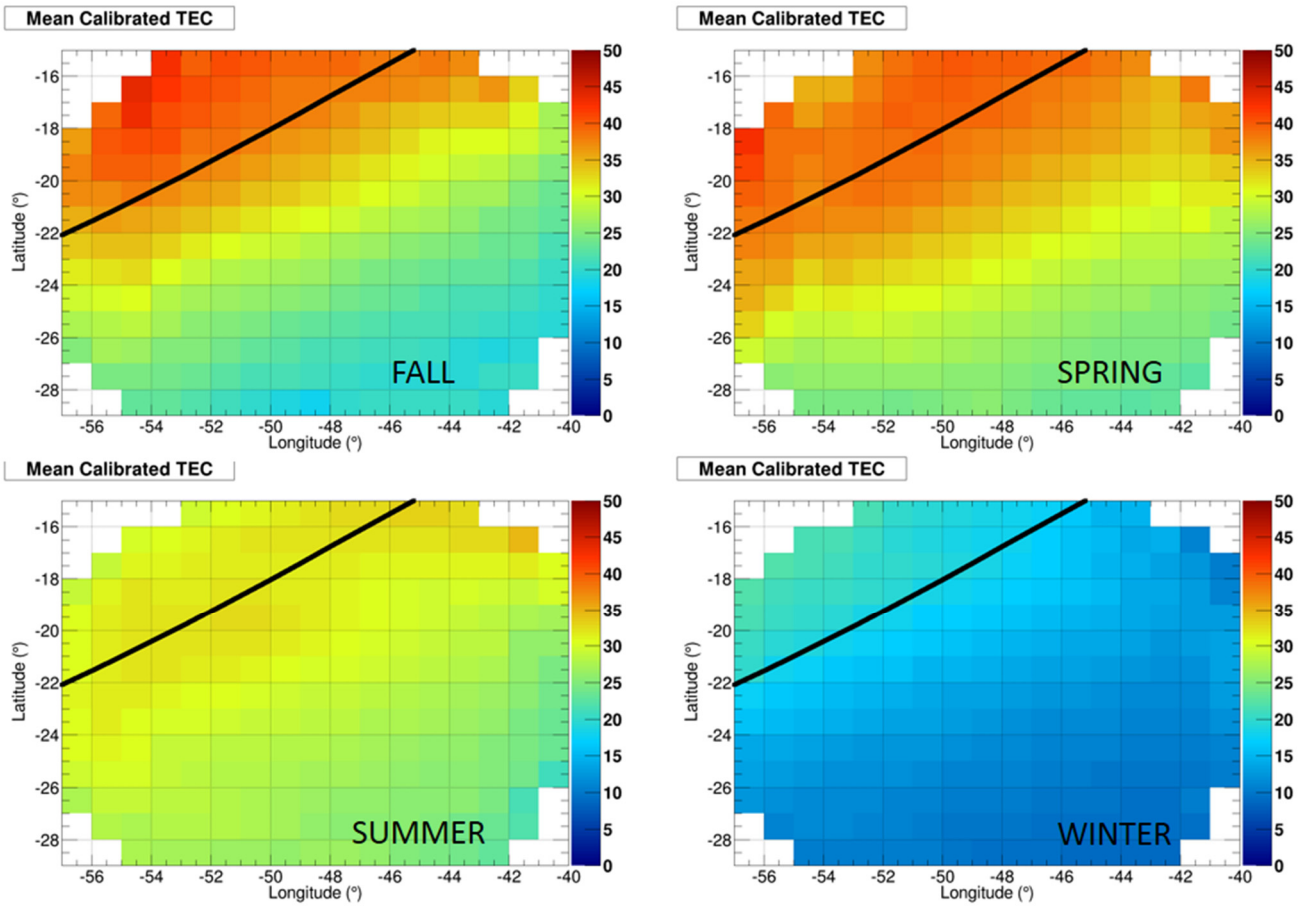

Figure 21. GBSC maps of TEC (in TECu) during the whole 2012 for each season. Black line represents the 15th southern magnetic parallel.

Figure 22 shows the ionospheric situation during the summer days. Panel a) represents the occurrence of S_4 > 0.25 that is the threshold above which the scintillation can be considered significant. From the map in panel a) is clear that the area with the greatest occurrence of amplitude scintillation is located about on the southern crest of the EIA. The maps of the spatial gradients of TEC (panel b and c) show that N-S gradients, reaching values up to $1X10^{-5}$ TECu/km, is greater than the E-W ones. Both N-S and E-W gradients present a similar behaviour changing direction crossing the 15th south magnetic parallel. From panel b) it's clear that the N-S gradients is northward (positive) for magnetic latitude greater than 15° becoming southward (negative) for magnetic latitude lesser than 15°. Zonal gradients show the same behaviour changing from westward (negative) to eastward (positive) values moving from lower to higher magnetic latitude. This gradients features reflect on the scintillation occurrence that shows a maximum along the 15th southern

magnetic parallel, where gradients change direction, highlighting that spatial gradients of TEC and amplitude scintillation are strictly in the region of the southern crest of the EIA. Panel e) and f) show the spatial gradients standard deviation for northward and eastward component respectively. A clear signature of the feature in these maps can be found, once again, in the occurrence of the amplitude scintillation distribution especially for N-S gradients. Values of the standard deviation of the N-S gradients different from the background (panel e) and f), yellow and dark blue bins) correspond to a high scintillation activity (panel a).

Figure 23 describe the mean ionosphere during the winter days of 2012. In this season the ionosphere appears quieter than during the summer. TEC distribution is almost homogeneous, i.e spatial gradients in both N-S and E-W directions do not show any pattern even if the meridional gradients seems to be slightly higher than the zonal ones. Although a signature of the southern crest of the EIA is clearly visible looking at the TEC distribution, also the standard deviation of the TEC (panel d) appear smoother than in the summer days. This quiet and homogeneous electron density distribution lead to an almost absent scintillation activity as can be seen on the scintillation occurrence maps (panel a).

Spring is the season in which the scintillation activities reaches its maximum (Figure 24, panel a) since the occurrence of S_4 is up to 20% and the region with a significant activity is wider than the area covered by the scintillation in summer. This is due to the great variability of the gradients of TEC as can be seen in panel e) and f) showing the standard deviation of the N-S and E-W gradients respectively. In this season the behaviour of the spatial gradients is similar to the one recorded during summer since it change direction moving from southern to northern magnetic latitude but the standard deviation of the gradients reaches values up to 2 times greater than in the summer ($50X10^4$ TEECu/km). North component of the gradient, as in the other seasons, appears greater and more variable than the east one. This reflect on the scintillation occurrence in which signature of this variability is clearly visible.

Figure 25 shows ionospheric condition during the fall days of 2012. As well as springs days, fall ones are characterized by a great standard deviation of the TEC in the whole area analysed (up to 25 TECu, panel d). Also high level of the spatial gradients is recorded during this season especially in N-S direction (up to $3X10^{-5}$ TECu/km, panel b and c) but looking at the standard deviation of the gradients (panel e and f) is clear that the gradients are quite homogeneous since these maps do not show any particular pattern. Scintillation activity is almost absent and comparable with the one recorded in winter days during which also the standard deviation of the gradients is neglectable. This observations lead to the conclusion that the scintillation activity is driven by the standard deviation of the TEC gradients and not from their absolute values. In fact, a high scintillation occurrence is observed when the standard deviation of the gradients is high (summer and spring, Figure 22 and Figure 24) independently from the values of the TEC and TEC gradients.

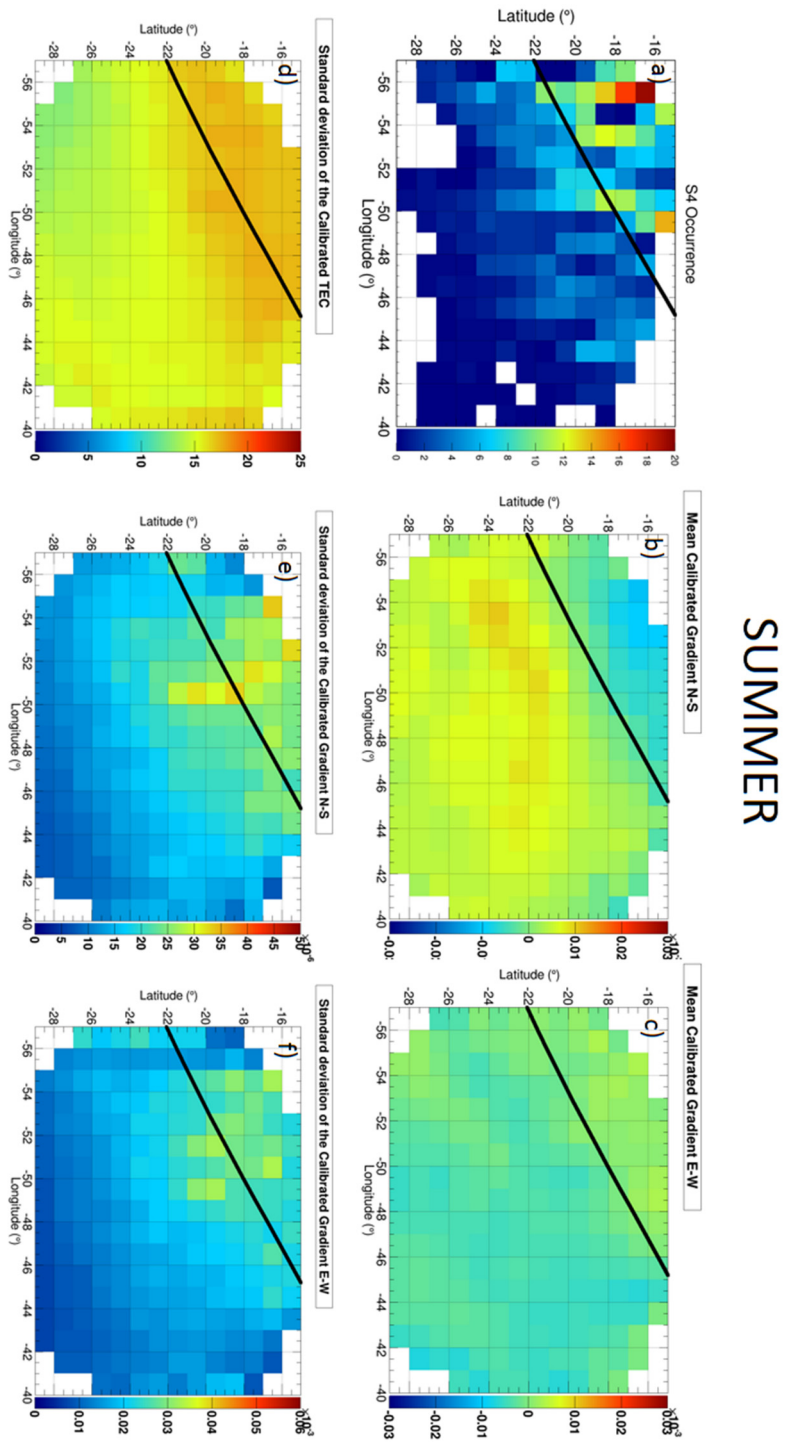

Figure 22. Climatological maps of different ionospheric parameters from GBSC for summer days. S4 occurrence (panel a), mean calibrated TEC gradients along N-S direction (in TECu/km, panel b) and its standard deviation (in TECu/km, panel e), mean calibrated TEC gradients along E-W direction (in TECu/km,panel c) and its standard deviation (in TECu/km,panel f), standard deviation of the calibrated TEC (panel d, in TECu). Black line represent 15th southern magnetic parallel.

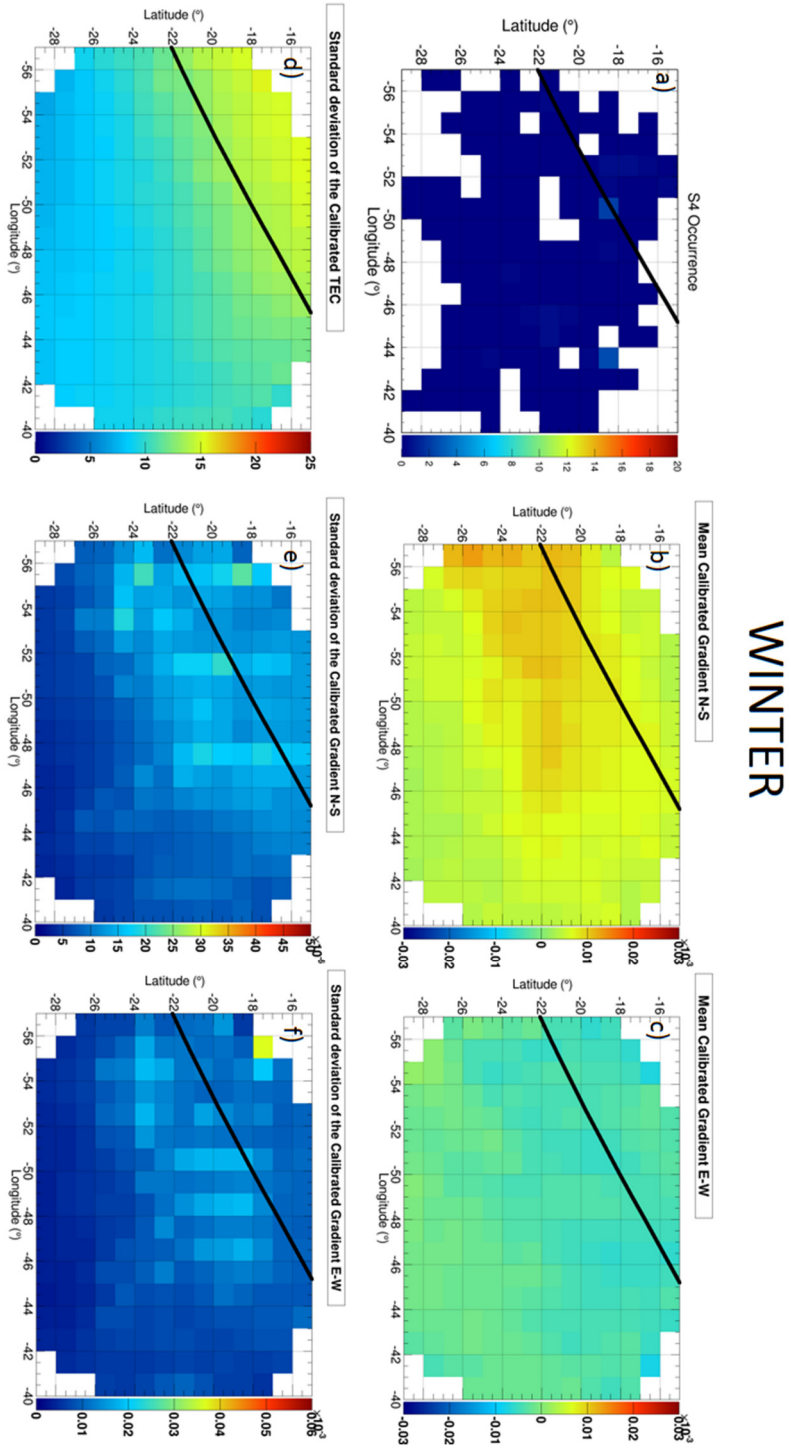

Figure 23. Climatological maps of different ionospheric parameters from GBSC for winter days. S4 occurrence (panel a), mean calibrated TEC gradients along N-S direction (in TECu/km, panel b) and its standard deviation (in TECu/km, panel e), mean calibrated TEC gradients along E-W direction (in TECu/km,panel c) and its standard deviation (in TECu/km,panel f), standard deviation of the calibrated TEC (panel d, in TECu). Black line represent 15th southern magnetic parallel.

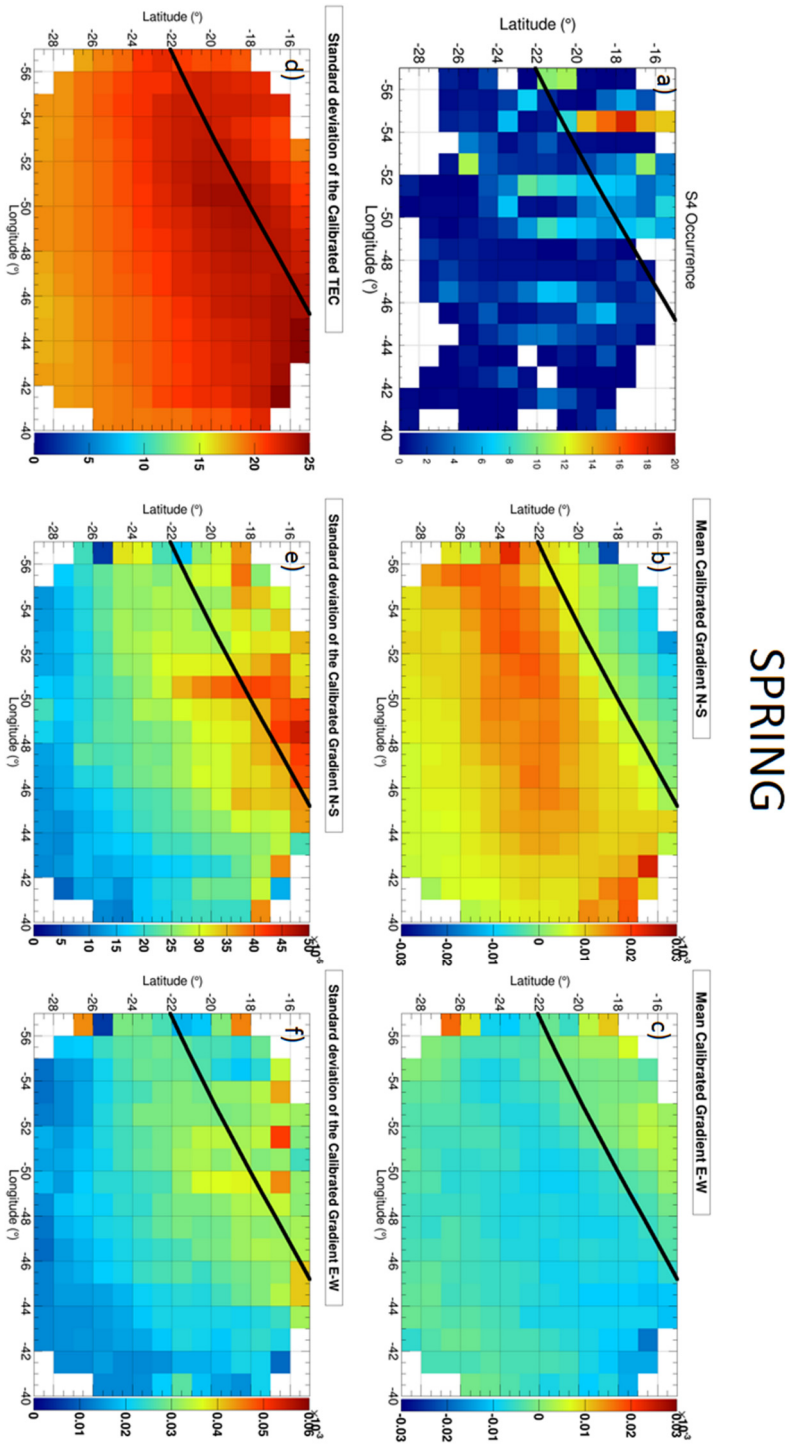

Figure 24. Climatological maps of different ionospheric parameters from GBSC for spring days. S4 occurrence (panel a), mean calibrated TEC gradients along N-S direction (in TECu/km, panel b) and its standard deviation (in TECu/km, panel e), mean calibrated TEC gradients along E-W direction (in TECu/km,panel c) and its standard deviation (in TECu/km,panel f), standard deviation of the calibrated TEC (panel d, in TECu). Black line represent 15th southern magnetic parallel.

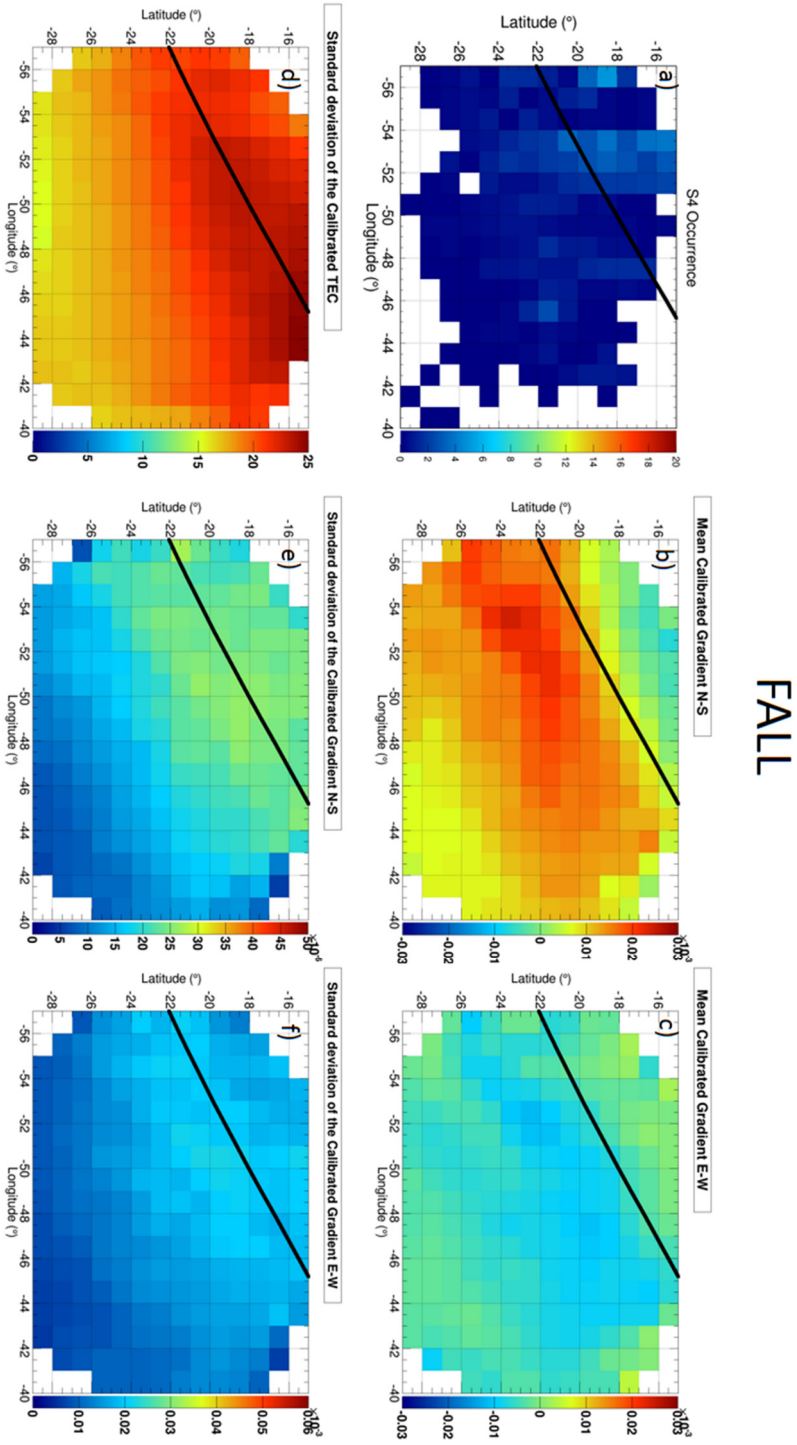

Figure 25. Climatological maps of different ionospheric parameters from GBSC for fall days. S4 occurrence (panel a), mean calibrated TEC gradients along N-S direction (in TECu/km, panel b) and its standard deviation (in TECu/km, panel e), mean calibrated TEC gradients along E-W direction (in TECu/km,panel c) and its standard deviation (in TECu/km,panel f), standard deviation of the calibrated TEC (panel d, in TECu). Black line represent 15th southern magnetic parallel.

3.2.2 Case studies

Cases for different seasons of 2012 and different scintillation conditions were analyzed to increase the understanding of the relationship between TEC spatial variations and amplitude scintillation occurrence coming the climatological studies presented in the previous section. Table 2 summarizes the case-studies chosen for this analysis, representing three different scintillation regimes: weak (S4<0.3), moderate (0.3<S4<0.7) and strong (S4>0.7) occurring at different seasons. The scintillation regimes have been chosen according to the maximum value reached by S4 over all satellites in view in the given day.

Table 4. Selected days considered as case studies covering a time period spanning all seasons of 2012 under 3 different scintillation conditions. Date and Julian day are reported for each day selected.

	S4 < 0.3	**0.3 <S4 < 0.7**	**S4 > 0.7**
Summer	16 Feb (47)	18 Jan (18)	12 Feb (43)
Winter	8 Jul (190)	9 Jul (191)	18 Jul (200)
Spring Equinox	8 Oct (282)	26 Sep (270)	9 Oct (283)
Fall Equinox	3 Apr (94)	25 Mar (85)	2 Apr (93)

Calibrated TEC values are calculated every 15 s (temporal resolution of RINEX files from URTKN receivers) whereas S4 values are computed from the PRU1 receiver firmware over 1 minute. Each map in Fig. 3 and 4 shows data collected during 10 minutes of measurements to improve the statistical consistency of the interpolated values. We consider a “frozen” ionosphere during 10 minutes to obtain more than 4000 TEC values associated with quite evenly distributed IPP. Even if this is a strong assumption, some tests carried out during data analysis showed that this is the best compromise between the temporal variability of ionosphere and a good spatial resolution of the maps.

We present maps of calibrated TEC, N-S and E-W gradients that include data of the most significant 10 minutes during the post-sunset period for each day. On the maps of the spatial gradients also scintillations events are depicted as white circles superimposed on the maps. Calibration of TEC gives a more realistic description of the ionospheric morphology during scintillation events differently from non-calibrated TEC data that are affected by the biases and errors afore mentioned. Maps related to weak scintillation days are not shown because they do not give significant contribution for the purposes of this study, i.e. for the days analysed under weak scintillation conditions (S4< 0.3) is not possible to find a clear relationship between gradients and amplitude scintillation intensity. Probably our method is not able to recognize gradients of very low intensity generating weak scintillation events. Given that the chosen interpolation method permits to estimate TEC values only inside of the convex hull of the pierce points dataset (Chazelle, 1993), the areas

covered by interpolated TEC values vary with the relative position between receivers and satellites. This is why for each day we are able to give TEC value over slightly different regions.

Figure 26 and Figure 27 show the maps for moderate and severe scintillation conditions listed in Table 4. Both figures contain TEC maps covering latitudes between 15° S and 30° S and longitude from 60° W to 40° W in the first row (panel a1,b1,c1,d1), second row shows zonal gradients over the same region (panel a2,b2,c2,d2) and in the last row there are meridional gradients maps (panel a3,b3,c3,d3). Dimension of white circles superimposed on gradients maps is proportional to the values of S_4 index on IPP. Panels a) of Figure 26 refers to ionospheric conditions on 18 January 2012 from 2:00 UTC to 2:10 UTC. We remind that LT=UTC-3. During this summer day, scintillations of moderate intensity ($0.3<S_4<0.7$) are associated with TEC gradients that reach values of the order of 0.3 TECu/km. These features are particularly visible near the southern crest region (geographic latitude≈20° S). During the winter day (09 July 2012 from 2:20 UTC to 2:30 UTC), panels b on Figure 26, the TEC distribution is quite uniform but some gradient structures of weak intensity but large spatial scale appear in the central part of the maps. Moderate scintillation events are recorded near the edges of the structures. Panels c) reports situation on 26 September 2012 (spring) during the period between 2:20 and 2:30 UTC in which the electrons distribution is inhomogeneous and the values of TEC reach annual maximum. Larger values of TEC are recorded in the region between longitudes 55° and 45° W. Some small TEC depletions (TEC<20 TECu), embedded into a region characterized by large TEC values (TEC≈90 TECu), are visible in the central and in the bottom panel. This is how the EPB's appear on this kind of map. This feature causes moderate scintillations (0.3<S4<0.7) distributed on the edges of the gradients. The fall day (25 March 2012 from 2:20 UTC to 2:30 UTC), panels d on Figure 27, is characterized by a more uniform electron density distribution with respect to the winter day, even if EPB's are still visible in the central part of the TEC map. Scintillations of moderate intensity are measured on the edges of some of those TEC structures. Here we remind that the scintillation information is available only at the pierce points of the signals in the 10 minutes time, so it is possible to discuss the eventual correlation between TEC and S_4 measurements only where scintillations appear on the map. Panels a of Figure 27 represent the state of the ionosphere during the period 2:20 UTC – 2:30 UTC on 12 February 2012. Under severe scintillation conditions ($S_4 > 0.7$) the meridional component of the TEC gradients reaches values larger than 0.5 TECu/km during the summer days as well as in the spring days (panels c, 9 October 2012 from 3:30 UTC to 3:40 UTC). The amplitude scintillation index increases in correspondence with strong gradient structures of small spatial extension. The maximum value of S_4 is reached near the southern crest region. The winter and the fall day (18 July 2012 from 4:20 UTC to 4:30 UTC and 2 April 2012 between 2:00 UTC and 2:10 UTC, respectively) look very similar .as shown in panels b and d of Figure 27. TEC values never exceed 40 TECu and the distribution of the electron content appears quite homogeneous. Despite this, some strong scintillation events are visible at the edges of the EPBs during the post-sunset period of both the days analyzed.

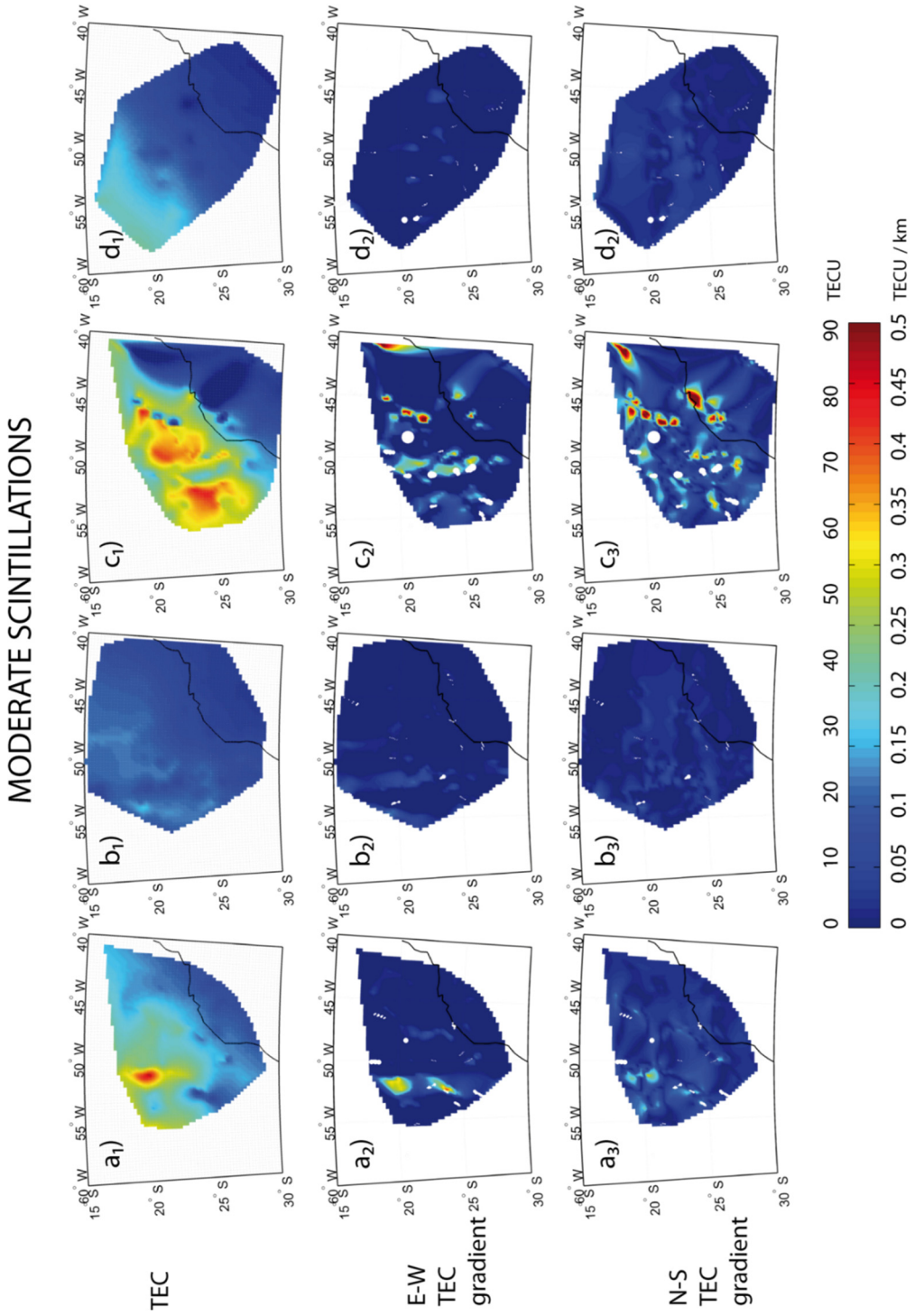

Figure 26. TEC, E-W and N-S TEC gradients maps for case studies under moderate scintillation condition. Panels a,b,c,d show ionospheric plasma distribution during summer, winter, spring equinox and fall equinox respectively (see Table 2). For all the days row 1,2,3 on the figure, represent TEC, E-W gradients and N-S gradients respectively. White points denote S_4 values at IPP. The greater the diameter of the circles, the higher is the value of the amplitude scintillation index.

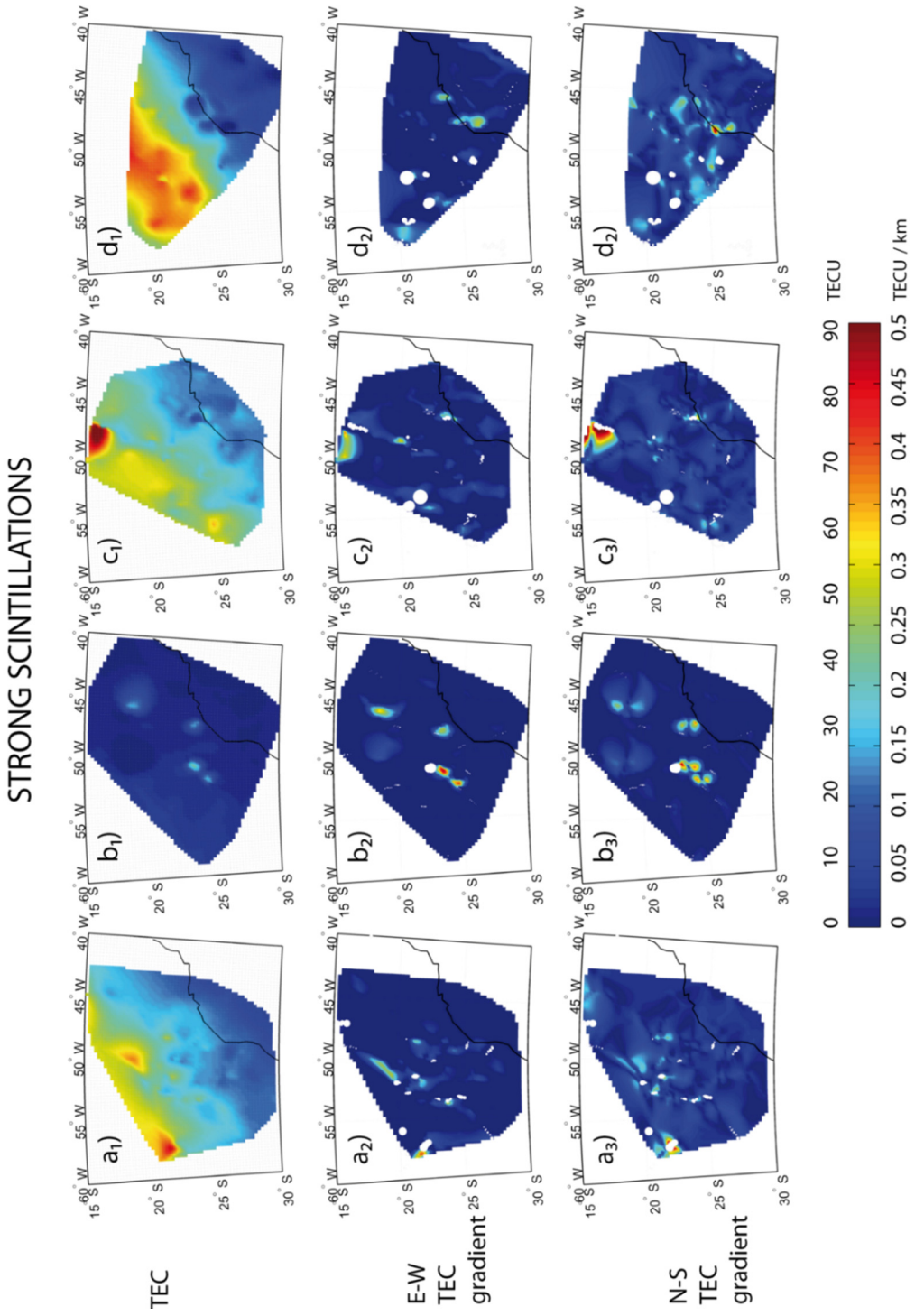

Figure 27. TEC, E-W and N-S TEC gradients maps for case studies under strong scintillation condition. Panels a,b,c,d show ionospheric plasma distribution during summer, winter, spring equinox and fall equinox respectively (see Table 2). For all the days row 1,2,3 on the figure, represent TEC, E-W gradients and N-S gradients respectively. White points superimposed denote S_4 values at IPP. The grater is the diameter of the circles, the higher is the value of the amplitude scintillation index.

3.3 Validation of the results in the "position domain"

To validate the results of the studies presented in the previous section, "truth" data of the ionospheric electron content should be available. Unfortunately, at present time, no instruments is able to measure absolute TEC. In order to validate TEC maps used to assess ionospheric morphology over Brazilian region, in collaboration with the Nottingham Geospatial Institute (NGI) of the University of Nottingham, such maps (hereafter CALIBRA TEC Maps or CTM) are used to compute 3D errors in positioning, as described in the following section, in comparison with the maps provided by International GNSS Service (IGS). Currently, vertical TEC (vTEC) maps are generated independently by four centers, i.e. CODE (Center for Orbit Determination in Europe), ESA (European Space Agency), JPL (Jet Propulsion Laboratory), and UPC (Polytechnic University of Catalonia). IGS combines them to generate the combined TEC map as a final product (Hernández-Pajares et al., 2009), which is used in this study. The GIM is provided as grid formatted vTEC value and corresponding vTEC RMS over the world in IONEX (Ionosphere map Exchange format) with 5° x 2.5° (lat/long) of spatial and 2 hours of temporal resolution. For the long baseline RTK processing, that is the algorithm adopted in this study, ,the GIM or the CTM were used in turn to provide the *a priori* information in in the equation described below, and their positioning performances were compared in order to evaluate the capability of each TEC map.

3.3.1 Data description

Figure 28 shows the GNSS stations of CALIBRA network (shown with red pins) consisting of Septentrio PolaRxS receivers, capable of monitoring ionospheric scintillation and the GNSS stations of the URTKN (shown with yellow pins) consisting of geodetic receivers from different manufacturers such as Trimble, Ashtech, Leica Geosystems, JAVAD, etc. The sampling rate of all experiments presented in this section is 15 seconds, which is currently the highest sampling rate available in the URTKN. In order to assess the RTK positioning results, we consider one of the reference stations in the network as a simulated rover so that the positioning solution at each epoch can be compared to the ground truth, which is the known coordinates of the simulated rover. In Figure 28 and Table 5, three selected baselines (BL1, BL2, BL3) are shown (red lines in Figure) which are chosen for the case studies based on the data availability at the different areas in the test site.

Table 5. Description of the baselines used for the experiments

	Reference - Rover	**Distance**
BL1	SPCA – SCJU	121.5 km
BL2	SPAR – SJRP	120.7 km
BL3	CHPI – SJCU	115.3 km

SJCU station is one of the CALIBRA network stations equipped with a PolaRxS receiver while the others are typical geodetic GNSS receivers, SPCA equips LEICA GRX1200, SPAR and SJRP equip TRIMBLE NETR8, and CHPI equips JAVAD TRE_G3T.

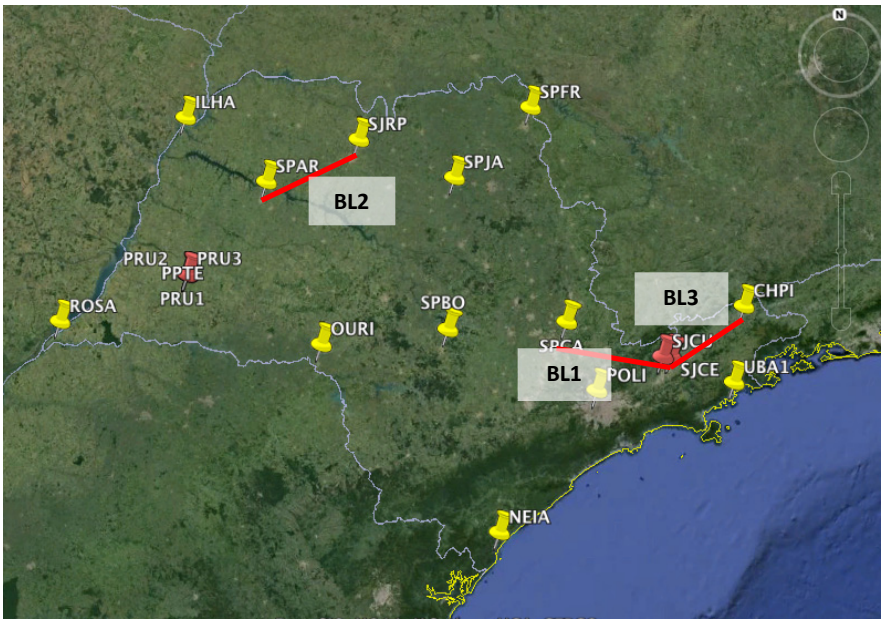

Figure 28. GNSS stations in São Paulo state including URTKN stations in yellow pins and CALIBRA network stations in red pins (Google earth); Selected baselines (BL1, BL2, and BL3) are indicated in red lines.

3.3.2 Long-baseline RTK algorithm

The dual frequency double difference (DD) GPS observables, in a wider term GNSS observables are expressed as follow:

$$\begin{cases} \Phi_{ij,1}^{kl} = \rho_{ij}^{kl} - I_{ij,1}^{kl} + T_{ij}^{kl} + \lambda_1 N_{ij,11}^{kl} + m_{ij,1}^{kl} + \varepsilon_{ij,1}^{kl} \\ \Phi_{ij,2}^{kl} = \rho_{ij}^{kl} - I_{ij,2}^{kl} + T_{ij}^{kl} + \lambda_2 N_{ij,2}^{kl} + m_{ij,2}^{kl} + \varepsilon_{ij,2}^{kl} \\ C_{ij,1}^{kl} = \rho_{ij}^{kl} + I_{ij,1}^{kl} + T_{ij}^{kl} + M_{ij,1}^{kl} + e_{ij,1}^{kl} \\ P_{ij,2}^{kl} = \rho_{ij}^{kl} + I_{ij,2}^{kl} + T_{ij}^{kl} + M_{ij,2}^{kl} + e_{ij,2}^{kl} \end{cases} \quad (3.15)$$

where a superscript *k*, *l* and subscript *i*, *j* denote satellites and stations, respectively. $\Phi_{ij,1}^{kl}$, $\Phi_{ij,2}^{kl}$ are the DD carrier phases of L1 and L2 respectively; $C_{ij,1}^{kl}$, $P_{ij,2}^{kl}$ are DD code pseudoranges of L1 and L2 respectively; ρ_{ij}^{kl} is the DD range between the stations *i* and *j* and the satellites *k* and *l*; $I_{ij,1}^{kl}$, $I_{ij,2}^{kl}$ are the DD ionospheric delays

of L1 and L2 respectively. Note that these terms represent the first order ionospheric delay term only. T_{ij}^{kl} is the DD tropospheric delay; λ_1, λ_2 are the wavelengths of L1 and L2; $N_{ij,1}^{kl}$, $N_{ij,2}^{kl}$ are the DD integer ambiguities on L1 and L2; $m_{ij,1}^{kl}$, $m_{ij,2}^{kl}$, $M_{ij,1}^{kl}$, $M_{ij,2}^{kl}$ are multipath errors of phases and code measurements on L1 and L2; $\varepsilon_{ij,1}^{kl}$, $\varepsilon_{ij,2}^{kl}$, $e_{ij,1}^{kl}$, $e_{ij,2}^{kl}$ are observation noises of phases and code observation on L1 and L2.

In this study, tropospheric delay is computed based on the calculation of a total zenith delay (TZD) model and a mapping function (MF) for each ray path and subtracted from the corresponding observation. The TZD was computed from Saastamoinen models (Saastamoinen, 1972) for both hydrostatic and wet delays with the standard atmosphere model as a meteorological data source. For the MF, Global Mapping Function (GMF) was applied. Integer ambiguity is searched by the Least-Squares AMBiguity Decorrelation Adjustment (LAMBDA) algorithm (Teunissen, 1994) and determined by W-ratio test (Wang et al., 1998).

The GNSS positioning solution can be performed by the adjustment computation theory. Equation (3.16) represents the Gauss-Markov Model (GMM) for a double difference GNSS solution involving two stations, one for which the coordinates need to be estimated. The GMM is a linear system of parameter estimation and is solved by the Least Squares (LSQ) method.

$$y = A\xi + e, \;\; e \sim \left(0, \sigma_0^2 W^{-1}\right) \tag{3.16}$$

where *y* is an observation vector, consisting of dual frequency GNSS observations, *ξ* is a parameter vector, which contains the corrections to the initial coordinates of the station to be estimated and other unknown parameters such as the ionospheric delay, carrier phase ambiguities, etc., *A* is a design matrix for the corresponding parameters in *ξ*, *e* is an observation error vector with the unit variance σ_0^2 and cofactor matrix *W*.

For the RTK solution of a short baseline under non-disturbed ionospheric conditions, the DD ionospheric delay can be ignored, assuming the ionospheric delays of four ray paths cancel each other and consequently the DD ionospheric delay is close to zero. If the residual ionospheric delay of each DD pair is not close to zero for a long baseline, it should be estimated separately, which introduces the constraint equation shown in equation (3.17).

$$\begin{cases} y = A\xi + e \\ z = K\xi + e_0 \end{cases}, \begin{bmatrix} e \\ e_0 \end{bmatrix} \sim \left(\begin{bmatrix} 0 \\ 0 \end{bmatrix}, \; \sigma_0^2 \begin{bmatrix} W^{-1} & 0 \\ 0 & Q_0 \end{bmatrix} \right) \tag{3.17}$$

where *z* is the a priori information for certain parameters of *ξ*, *K* is the corresponding design matrix, e_0 is the error vector of the a prior information, and Q_0 is the corresponding cofactor matrix.

If TEC maps are available in the area of interest, the DD ionospheric delay of a particular GNSS ray path can be predicted, which is included in the a priori information vector, z, and its accuracy, whose stochastic characteristic is defined by $\sigma_0^2 Q_0^2$.

3.3.3 Performance of IGS and CTM maps

This section presents the case studies for long baseline RTK using the GIM and CTM under different scintillation conditions (quiet or strong) and compares the performance of each ionospheric map.

For the quiet scintillation case, BL1 (see Figure 28) was selected on DOY141, 2013 (21 May 2013) as the S4 index recorded at SJCU in BL1 was lower than 0.3 during most of the day. Figure 29 shows the RTK processing results of BL1 (SPCA-SJCU, baseline length 121.5km) aided respectively by the GIM (left panel) and the CTM (right panel). The top three plots in each panel indicate the positioning error in north, east, and up components respectively and the bottom plot is the ambiguity resolution (AR) index (0-float, 1-fixed).

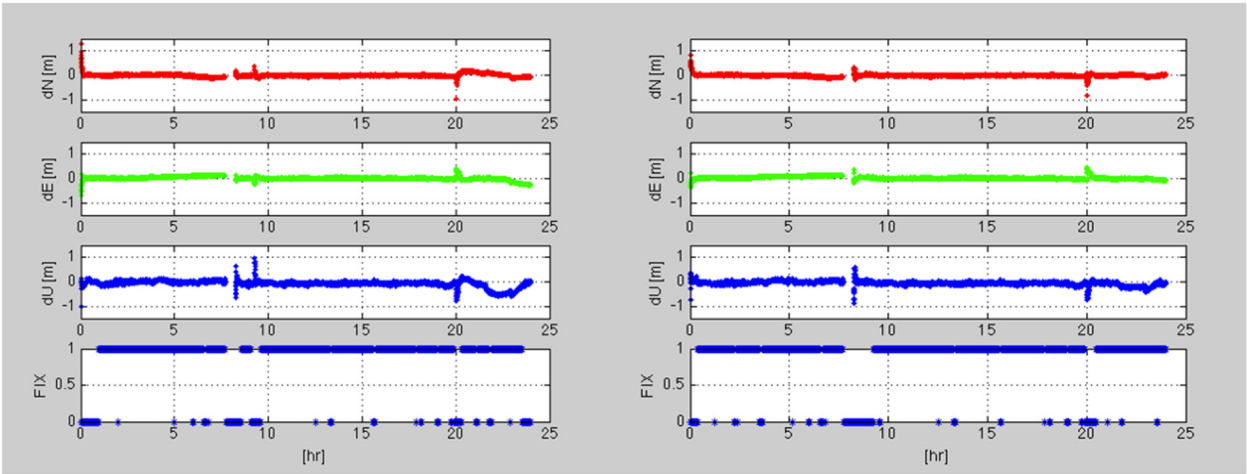

Figure 29. RTK result of BL1 using the GIM (left) and using the CTM (right) on DOY141, 2013 (time is in UT) – quiet day scintillation case; Positioning error in north, east, and up components on the top three plots (dN, dE, dU) and the ambiguity resolution index on the bottom plot (0 – float, 1 – fixed)

The AR success rates by using respectively the GIM and the CTM are 81.8% and 84.2%, while the 3D positioning RMSs are 0.130 m and 0.101 m. The positioning performance using either of the maps is quite satisfactory if one considers the 15 sec sampling rate and a 121.5 km baseline. The low values of S4 indicate that there were no significant TEC fluctuations or associated scintillation activity so that both the GIM and the CTM work equally well in RTK.

Further, an anomalous behavior in the dU time series observed around 22-24 hours using GIM (shown in the left panel) is mitigated by using the CTM (shown in the right panel). By using the CTM, the AR success rate slightly increased, with a consequent improvement in the overall RMS. From this result, it can be concluded that the CTM performed better than the GIM but the improvement is not much significant during the quiet ionospheric conditions.

Unlike the quiet case, strong scintillation cases are more challenging due to the larger TEC spatial and temporal gradients in the region. Several strong scintillation cases were chosen and their RTK results with the GIM and the CTM were compared. Figure 30 shows the S4 recorded on DOY 269 in 2013 at PRU1 and SJCU stations, which are located in the west and east regions of São Paulo state respectively. From Figure 30, it can be seen that both receivers recorded high S4 during the local post sunset hours (0-6 UT and 22-24 UT).

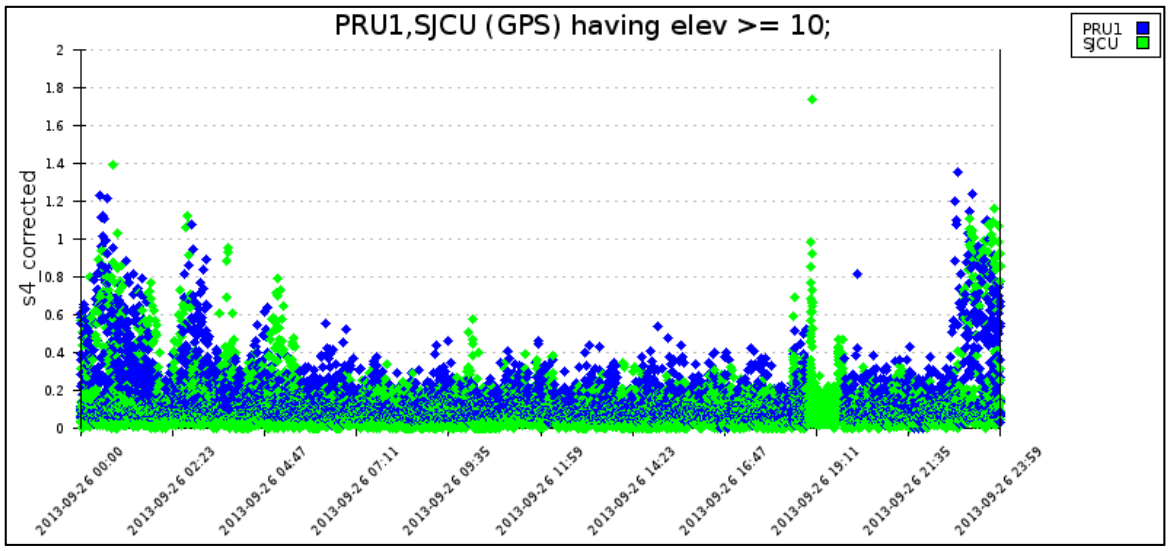

Figure 30: S4 recorded at PRU1 and SJCU on DOY269, 2013 (time is in UT)

For the experiments, BL2 (the nearest scintillation monitoring station is PRU1) and BL3 (which includes SJCU) were processed using the GIM and the CTM. Figure 31 and Figure 32 are the RTK positioning results of BL2 (SPAR-SJRP, baseline length 120.7 km) and BL3 (CHPI-SJCU, baseline length 115.3km) on DOY269 in 2013, respectively.

For BL2 (Figure 31), the AR success rate and the 3D positioning RMS when using the GIM are 4.0% and 2.279m respectively, and when using the CTM they are 36.6% and 1.294m respectively. For BL3 (Figure 32), the AR success rate and the 3D positioning RMS when using the GIM are 20.9% and 1.546m respectively, while when using the CTM, they are 67.1% and 0.403m respectively. From the two figures, it can be observed that the use of the CTM resulted in more fixed solutions than the GIM and hence the CTM performed better than the GIM in providing the external ionospheric information. It should be noted that in both cases, the RTK

solutions during the strong scintillation hours (about 0-6 UT and 22-24 UT) barely resulted in fixed solutions. That was most likely due to the poor quality of the observations during the scintillation events.

Table 6 lists the experimental results including more case studies, which compare the performance of the GIM and the CTM under quiet, moderate, and strong scintillation conditions. The last two columns in the table, titled 'Improvement of 3D RMS' in meter and percentage, show the improvement in terms of 3D RMS by using the CTM compared with the one by using the GIM.

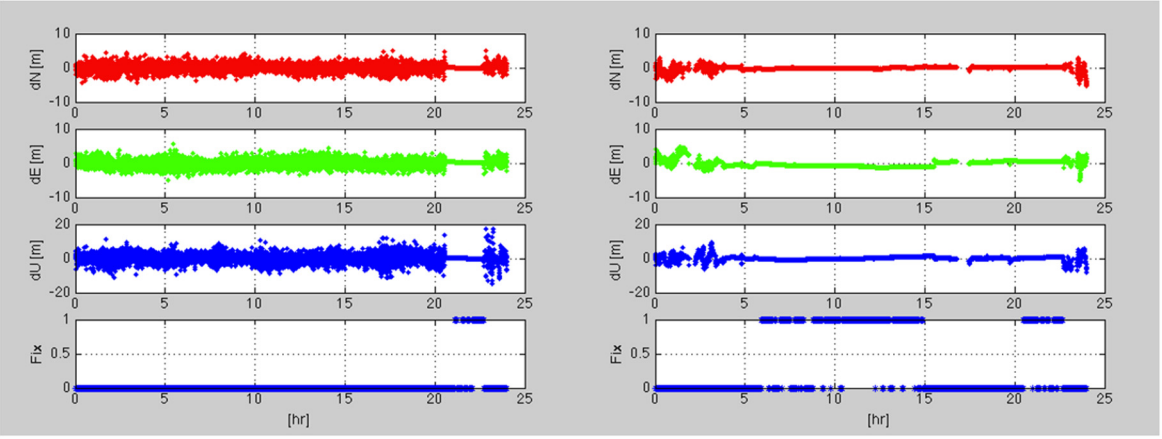

Figure 31: RTK result of BL2 using the GIM (left) and using the CTM (right) on DOY269, 2013 (time is in UT) – strong scintillation case; Positioning error in north, east, and up components on the top three plots (dN, dE, dU) and the ambiguity resolution index on the bottom plot (0 – float, 1 – fixed)

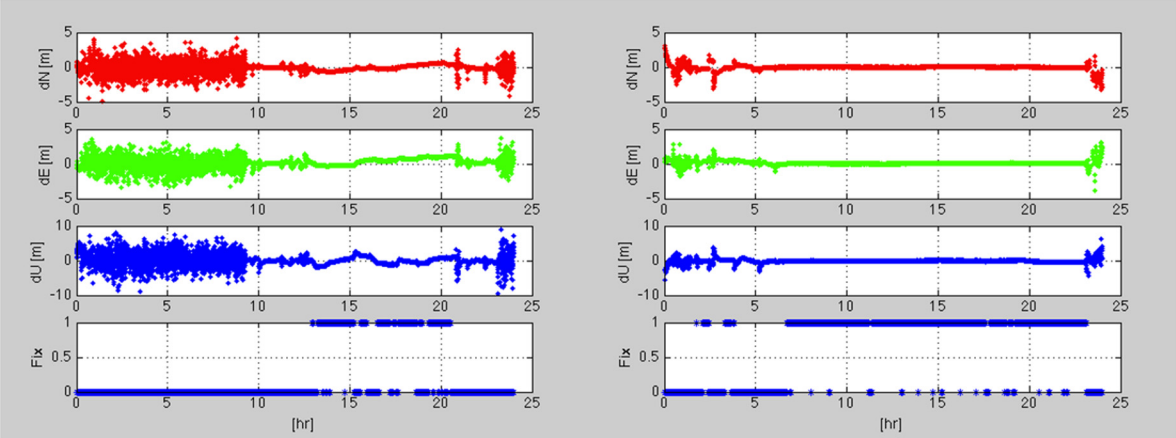

Figure 32: RTK result of BL3 using the GIM (left) and using the CTM (right) on DOY269, 2013 (time is in UT) – strong scintillation case; Positioning error in north, east, and up components on the top three plots (dN, dE, dU) and the ambiguity resolution index on the bottom plot (0 – float, 1 – fixed)

Table 6. Summary of the results including also cases not described in the text.

DOY, Year	Baseline	Scintillation Category	GIM		CTM		Improvement of 3D RMS	
			AR [%]	**3D RMS [m]**	**AR [%]**	**3D RMS [m]**	**[m]**	**[%]**
141, 2013	BL1	Quiet	81.8	0.130	84.2	0.101	0.019	22.3%
141, 2013	BL2	Moderate	62.3	0.164	72.6	0.263	-0.099	-60.4%
269, 2013	BL2	Strong	4.0	2.579	36.6	1.294	1.285	49.8%
269, 2013	BL3	Strong	20.9	1.546	60.6	0.403	1.143	73.9%
21, 2014	BL3	Strong	17.3	1.193	58.6	0.749	0.444	37.2%
45, 2014	BL2	Strong	14.0	1.026	17.4	1.141	-0.115	-11.2%
AVG				1.106		0.659	40.4%	

It can be observed from Table 6 that for most cases, the CTM performed better than the GIM in terms of the AR success rate and the 3D RMS. However, there are two cases (shown as negative improvement) when the use of CTM degraded the RTK performances. For the cases of BL2 on DOY141 in 2013 and of BL2 on DOY45 in 2014, the AR success rate using the CTM were slightly higher and the positioning RMS results were slightly poorer, which must be due to incorrectly fixed ambiguities.. However, the absolute 3D positioning errors of these cases are not much significant, which are around 10cm, compared to the big improvements in other cases.

3.4 Summary and discussion

The case studies suggest that the ionospheric condition of the URTKN area during the year 2012 in the post-sunset, pre-midnight and post-midnight hours (02-06 UTC; corresponding to 23-03 LT) can be described as follows.

Calibrated TEC shows the expected seasonal variation reaching the highest values during spring (up to 90 TECu) and the lowest values during winter (lower than 40 TECu). The spring and fall equinoxes ionospheric backgrounds, under quiet scintillation conditions, are very similar and are mainly ruled by the solar irradiation (sunset time in spring and fall around 18 LT);

When S4 is moderate or disturbed, the TEC behaviour of the two equinoxes differs: when 0.3<S4<0.7 the spring time presents the highest values (up to 90 TECu), while during fall TEC reaches 50 TECu; for S4>0.7 both spring and fall record TEC levels up to 90 TECu;

The TEC gradients scenario is more complex: under quiet conditions both the N-S and the E-W variations, if any, are weak. Only during fall the N-S TEC variation presents several significant gradients (up to 0.1 TECu/km, not shown in the figure). Under moderate S4 levels there are several N-S and E-W gradients of medium intensity (up to 0.3 TECu/km) during summer (Figure 26, panels a) and of high intensity (0.5 TECu/km or more) during spring (Fig. 2, panels c). Scintillations at the high end of the moderate level are mostly visible on the edges of plasma bubbles of different N-S and E-W sizes in spring. The spring equinox reveals to be the most scintillation effective also under severe scintillation conditions: both the N-S and E-W TEC gradients are intense, even if quite few (Figure 27, panels c). During summer and winter, severe scintillations result to be produced either by plasma density depletions or by enhancements of medium intensity (Figure 27, panels a, b).

From the comparison between the maps of TEC and TEC gradients presented herein one can deduce that the plasma bubbles, visible as TEC depletions with the extension of hundreds kilometers in the TEC maps, are better revealed by the N-S gradients. Often the scintillations are visible on the edge of N-S gradients, which could mean that, on average, scintillations are mainly produced by latitudinal TEC gradients.

Not all the latitudinal neither all the longitudinal TEC gradients produce moderate or severe scintillations. This is probabily due to the fact that amplitude scintillations are produced by ionospheric irregularities of scale sizes up to the Fresnel dimension that on L band is of hundreds of meters considering the irregularities located at the F layer peak. Thus, only irregularities having such at horizontal dimension can lead to scintillation.

It is clear from the maps that in the region of the southern crest of the EIA there is a high scintillation occurrence. EPBs generated in the magnetic equator region, in fact, are well-developed when they reach the crest region and this is the cause of the generation of small-scale (hundred meters) irregularities producing scintillations (Muella et al., 2010).

Besides, it can be assumed that the electron density gradients are due to the plasma transport and deductions about the way in which the transport of plasma takes place in these cases can be made.

The transport transversal with respect to the magnetic field B (TT) cannot lead to electron density gradients, as at the heights of the F2 region, the plasma is incompressible in that direction. Conversely, the gradients can be associated to the transport of plasma in a direction parallel with respect to B (PT). Then, it has been shown that the Rayleigh Taylor instability is associated with TT rather than with PT (Tsunoda, 2013). The

observation of scintillations in association with the gradient suggests that, at least in these circumstances, act simultaneously both the TT that PT.

3.5 Conclusions

The analysis of TEC spatial distribution and S_4 index during 4 seasons of 2012 is performed using URTKN and CIGALA scintillation monitor network covering the São Paolo state region, including the region of the Southern crest of the EIA. From the climatological analysis and case studies, the main features resulting can be summarized as follows:

1. Scintillation occurrence is mainly driven by the presence of high values of the gradients standard deviation.

2. At least for strong scintillations, S_4 values are often associated with meridional gradients.

3. Strongest scintillations take place during post-sunset spring equinox at the edge of high intensity TEC gradient structure. Scintillations are mostly observed in the region of the southern crest of the EIA in which the distribution of the plasma appears quite inhomogeneous.

4. TEC is confirmed to reach highest values during the spring seasons even if, under strong scintillations regime, also during the fall post-sunset hours TEC can assume values of up to 90 TECu.

In the framework of the FP7 CALIBRA project (Countering GNSS high Accuracy applications Limitations due to Ionospheric disturbances in Brazil) a number of additional high sampling rate scintillation receivers covering São Paulo state region have been recently deployed to increase the potential of the scintillation monitoring network. In particular, 3 of these receivers are placed at a few hundred meters from each other along geomagnetic E-W and N-S directions. Using data collected by two of these three receivers, also the dynamic of the ionospheric irregularities causing scintillation is studied as widely described in the next section.

3.6 References

Abdu, M. a., Batista, I. S., Carrasco, a. J. and Brum, C. G. M.: South Atlantic magnetic anomaly ionization: A review and a new focus on electrodynamic effects in the equatorial ionosphere, J. Atmos. Solar-Terrestrial Phys., 67(17-18), 1643–1657, doi:10.1016/j.jastp.2005.01.014, 2005.

Alfonsi, L., Spogli, L., De Franceschi, G., Romano, V., Aquino, M., Dodson, A. and Mitchell, C. N.: Bipolar climatology of GPS ionospheric scintillation at solar minimum, Radio Sci., 46, doi:10.1029/2010RS004571, 2011.

Bevis, M., Businger, S., Herring, T. A., Rocken, C., Anthes, R. A. and Ware, R. H.: GPS meteorology: Remote sensing of atmospheric water vapor using the global positioning system, J. Geophys. Res., 97(D14), 15787, doi:10.1029/92JD01517, 1992.

Blewitt, G., Kreemer, C., Hammond, W. C., Plag, H. P., Stein, S. and Okal, E.: Rapid determination of earthquake magnitude using GPS for tsunami warning systems, Geophys. Res. Lett., doi:10.1029/2006GL026145, 2006.

Boissonnat, J.-D. and Cazals, F.: Smooth surface reconstruction via natural neighbour interpolation of distance functions, Comput. Geom., 22, 185–203, doi:10.1016/S0925-7721(01)00048-7, 2002.

Chatterjee, S. and Chakraborty, S. K.: Variability of ionospheric scintillation near the equatorial anomaly crest of the Indian zone, Ann. Geophys., 31(4), 697–711, doi:10.5194/angeo-31-697-2013, 2013.

Chazelle, B.: An optimal convex hull algorithm in any fixed dimension, Discrete Comput. Geom., 10(1), 377–409, doi:10.1007/BF02573985, 1993.

Ciraolo, L., Azpilicueta, F., Brunini, C., Meza, a. and Radicella, S. M.: Calibration errors on experimental slant total electron content (TEC) determined with GPS, J. Geod., 81, 111–120, doi:10.1007/s00190-006-0093-1, 2007.

Crane, R. K.: Ionospheric scintillation, Proc. IEEE, 65(2), 180–199, doi:10.1109/PROC.1977.10456, 1977.

Doherty, P., Coster, A. J. and Murtagh, W.: Space weather effects of October-November 2003, GPS Solut., 8(4), 267–271, doi:10.1007/s10291-004-0109-3, 2004.

Dow, J. M., Neilan, R. E. and Rizos, C.: The International GNSS Service in a changing landscape of Global Navigation Satellite Systems, J. Geod., 83(3-4), 191–198, doi:10.1007/s00190-008-0300-3, 2009.

Finlay, C. C., Maus, S., Beggan, C. D., Bondar, T. N., Chambodut, A., Chernova, T. A., Chulliat, A., Golovkov, V. P., Hamilton, B., Hamoudi, M., Holme, R., Hulot, G., Kuang, W., Langlais, B., Lesur, V., Lowes, F. J., Lühr, H., Macmillan, S., Mandea, M., McLean, S., Manoj, C., Menvielle, M., Michaelis, I., Olsen, N., Rauberg, J., Rother,

M., Sabaka, T. J., Tangborn, A., Tøffner-Clausen, L., Thébault, E., Thomson, A. W. P., Wardinski, I., Wei, Z. and Zvereva, T. I.: International Geomagnetic Reference Field: the eleventh generation, Geophys. J. Int., 183(3), 1216–1230, doi:10.1111/j.1365-246X.2010.04804.x, 2010.

Foster, M. P. and Evans, A. N.: An Evaluation of Interpolation Techniques for Reconstructing Ionospheric TEC Maps, IEEE Trans. Geosci. Remote Sens., 46(7), 2153–2164, doi:10.1109/TGRS.2008.916642, 2008.

De Franceschi, G., Alfonsi, L., Romano, V., Aquino, M., Dodson, A., Mitchell, C. N., Spencer, P. and Wernik, A. W.: Dynamics of high-latitude patches and associated small-scale irregularities during the October and November 2003 storms, J. Atmos. Solar-Terrestrial Phys., 70(6), 879–888, doi:10.1016/j.jastp.2007.05.018, 2008.

Frezzotti, M., Capra, A. and Vittuari, L.: Comparison between glacier ice velocities inferred from GPS and sequential satellite images, Ann. Glaciol., 1998.

Hernández-Pajares, M., Juan, J. M., Sanz, J., Orus, R., Garcia-Rigo, a., Feltens, J., Komjathy, a., Schaer, S. C. and Krankowski, a.: The IGS VTEC maps: A reliable source of ionospheric information since 1998, J. Geod., 83, 263–275, doi:10.1007/s00190-008-0266-1, 2009.

Koster, J. R.: Equatorial scintillation, Planet. Space Sci., 20(12), 1999–2014, doi:10.1016/0032-0633(72)90056-6, 1972.

Larson, K. M.: GPS seismology, J. Geod., doi:10.1007/s00190-008-0233-x, 2009.

Lee, D. T. and Schachter, B. J.: Two algorithms for constructing a Delaunay triangulation, Int. J. Comput. Inf. Sci., 9(3), 219–242, doi:10.1007/BF00977785, 1980.

Mannucci, a. J., Wilson, B. D., Yuan, D. N., Ho, C. H., Lindqwister, U. J. and Runge, T. F.: A global mapping technique for GPS-derived ionospheric total electron content measurements, Radio Sci., 33(3), 565, doi:10.1029/97RS02707, 1998.

Mitchell, C. N., Alfonsi, L., De Franceschi, G., Lester, M., Romano, V. and Wernik, a. W.: GPS TEC and scintillation measurements from the polar ionosphere during the October 2003 storm, Geophys. Res. Lett., 32(12), 1–4, doi:10.1029/2004GL021644, 2005.

Muella, M. T. a H., Kherani, E. a., De Paula, E. R., Cerruti, a. P., Kintner, P. M., Kantor, I. J., Mitchell, C. N., Batista, I. S. and Abdu, M. a.: Scintillation-producing Fresnel-scale irregularities associated with the regions of steepest TEC gradients adjacent to the equatorial ionization anomaly, J. Geophys. Res. Sp. Phys., 115(A3), A03301, doi:10.1029/2009JA014788, 2010.

Muella, M. T. a H., de Paula, E. R. and Monteiro, A. a.: Ionospheric Scintillation and Dynamics of Fresnel-Scale Irregularities in the Inner Region of the Equatorial Ionization Anomaly, Surv. Geophys., 34(2), 233–251, doi:10.1007/s10712-012-9212-0, 2013.

Okabe, A., Boots, B. and Sugihara, K.: Nearest neighbourhood operations with generalized Voronoi diagrams: a review, Int. J. Geogr. Inf. Syst., doi:10.1080/02693799408901986, 1994.

Parkinson, B. and Spiker, J. J.: Global Positioning System: Theory and Applications, Volume 1., 1996.

Rama Rao, P. V. S., Gopi Krishna, S., Niranjan, K. and Prasad, D. S. V. V. D.: Study of spatial and temporal characteristics of L-band scintillations over the Indian low-latitude region and their possible effects on GPS navigation, Ann. Geophys., 24(6), 1567–1580, doi:10.5194/angeo-24-1567-2006, 2006.

Rino, C. L.: A power law phase screen model for ionospheric scintillation: 2. Strong scatter, Radio Sci., 14, 1147, doi:10.1029/RS014i006p01147, 1979a.

Rino, C. L.: A power law phase screen model for ionospheric scintillation: 2. Strong scatter, Radio Sci., 14, 1147, doi:10.1029/RS014i006p01147, 1979b.

Rino, C. L. and Livingston, R. C.: On the analysis and interpretation of spaced-receiver measurements of transionospheric radio waves, Radio Sci., 17, 845, doi:10.1029/RS017i004p00845, 1982.

Romano, V. and Bougard, B.: Investigation of low latitude scintillations in Brazil within the cigala project, Proocedings 3rd Int. Colloq. Sci. Fundam. Asp. Galileo Program. Copenaghen 2011, 2011.

Saastamoinen, J.: Atmospheric correction for the troposphere and stratosphere in radio ranging satellites, Geophys. Monogr. Ser., 15, 247–251, doi:10.1029/GM015p0247, 1972.

Sekido, M.: Evaluation of GPS-based ionospheric TEC map by comparing with VLBI data, Radio Sci., 38(4), n/a–n/a, doi:10.1029/2000RS002620, 2003.

Shimada, S., Fujinawa, Y., Sekiguchi, S., Ohmi, S., Eguchi, T. and Okada, Y.: Detection of a volcanic fracture opening in Japan using Global Positioning System measurements, Nature, doi:10.1038/343631a0, 1990.

Spogli, L., Alfonsi, L., De Franceschi, G., Romano, V., Aquino, M. H. O. and Dodson, a.: Climatology of GPS ionospheric scintillations over high and mid-latitude European regions, Ann. Geophys., 27(9), 3429–3437, doi:10.5194/angeo-27-3429-2009, 2009.

Teunissen, P. J. G.: A new method for fast carrier phase ambiguity estimation, Proc. 1994 IEEE Position, Locat. Navig. Symp. - PLANS'94, doi:10.1109/PLANS.1994.303362, 1994.

Tsunoda, R. T.: On seeding equatorial spread F: Parallel or transverse transport?, J. Atmos. Solar-Terrestrial Phys., 103, 24–29, doi:10.1016/j.jastp.2012.10.016, 2013.

Wang, J., Stewart, M. P. and Tsakiri, M.: A discrimination test procedure for ambiguity resolution on-the- ¯ y, J. Geod., 644–653 [online] Available from: http://link.springer.com/article/10.1007/s001900050204

Yeh, K. C. and Swenson, G. W.: The scintillation of radio signals from satellites, J. Geophys. Res., 64(12), 2281–2286, doi:10.1029/JZ064i012p02281, 1959.

4 Zonal velocity of the ionospheric irregularities

A deeper understanding of the ionospheric phenomena affecting the GNSS signals propagation needs the analysis of the dynamics of the ionospheric irregularities driving scintillation. Thus, the estimation of the velocity of the ionospheric irregularities plays a fundamental role in validating ionospheric models, in particular those adopted to assist the mitigation solutions using the evaluation of the plasma velocity field as proxy for the scintillations forecasting (Wernik et al., 2007). Also in CALIBRA FP7 project, in the framework of which this work has been done, a model for the short term forecasting of TEC and scintillation parameters has been developed. The fundamental equations, on which the model is based, contain the velocity field of the ionospheric plasma and so, an independent evaluation of such velocity field like the one presented in this section, could help a correct estimation of the ionospheric parameters.

4.1 Measurement technique

The spaced-receivers technique is used since decades to estimate the movement of the scintillation patterns at the receivers as well as to estimate the geometric properties of the ionospheric plasma irregularities (Basu et al., 1996; Kil et al., 2000). The technique is based on the transmission of one or more radio waves from a remote source, i.e. an artificial satellite (in our case, GPS satellites). If the frequency of the radio waves is greater than the ionospheric plasma frequency (or the electron gyrofrequency), the waves can be diffracted by ionospheric irregularities smaller than the appropriate first Fresnel zone size (≈250 m for GPS-L1 frequency). The diffraction effects is visible on the signal recorded by the receiver on ground as scintillation pattern in both amplitude and phase. (Yeh and Liu, 1982). Using cross-correlation (Costa et al., 1988) or cross-spectral techniques, the velocity (V_{scint}) and the orientation of amplitude and phase scintillation pattern can be evaluated, together with the zonal velocity (V_{ion}) of the irregularities.

It is assumed that both the receivers and the source of the radio waves are sufficiently far from the scattering medium (the ionospheric plasma) and that their relative distances are much larger than the scale size of the irregularities that cause diffraction (Huygen-Fresnel diffraction regime). This hypothesis is verified as in our case, the source of the signal is an artificial satellite (e.g. GPS) orbiting at about 20000 km above the Earth surface and the scattering media is the ionospheric thin layer at 350 km.

The propagation ray-paths are assumed straight and, additionally, the signal propagation speed (speed of light), is assumed to be much greater than the scintillation pattern velocity or satellite velocity that is typically of the order of hundreds of meters per second.

The scintillation-causing irregularities are assumed to be located in a relatively thin layer (typically at 350 km above sea level), aligned along the magnetic field lines and moving predominantly along the East-West magnetic direction (Yeh and Liu, 1982). This alignment causes the scintillation pattern produced by the

irregularities to be projected onto the receiver plane (Kintner, 2004; Rino and Livingston, 1982). The scintillation pattern projection is not necessarily aligned along the magnetic field direction.

A sketch of the zonal velocity measurement is given in Figure 33. Two receivers (REC1 and REC2) acquiring GNSS signals at 50 Hz are 300 m spaced out, i.e. about the Fresnel scale for GPS frequencies. At a given time (t_0), the signal acquired by REC2 crosses the ionospheric irregularity generating a scintillation pattern in the signal recorded (Figure 33a). At time t_1, the same irregularity crosses the line of sight GPS-REC1 (Figure 33b). Under the hypothesis that the irregularity shape does not change between t_0 and t_1, the scintillation patterns recorded by the two receivers should be strictly correlated. In Figure 33, a typical signal to noise ratio recorded when the signal crosses an irregularity is shown in red while the blue plots represent the signal to noise ratio when the ionospheric irregularities are not present.

Spaced-receivers analysis estimates the scintillation pattern velocity by dividing the receivers' separation distance (≈300 m) by the scintillation pattern time lag between the two receivers (estimated trough a correlation analysis technique). This measurement method is reasonable, as long as it is assumed that the scintillation pattern velocity is constant during the time lag (Kintner et al., 2004).

The zonal scintillation pattern velocity, estimated by using a pair of receivers, may be biased with respect to the “truth” scintillation pattern velocity. Three different factors can lead to biases:

- The scintillation pattern is evolving in time as it moves between receivers, so the measured velocity is not the actual velocity of the scintillation pattern. A “random” characteristic velocity due to the changing shape of the pattern perturbs the “true” pattern velocity during the motion between the two receivers. In our case, the random velocity is considered negligible (frozen-in hypothesis) as the receivers are close enough to reasonably consider the shape of the irregularities fixed between the two receivers. The typical time lags, in fact, is about a couple of second.
- The receivers are not precisely aligned along the zonal direction. A vertical displacement of the receivers may causes a pattern velocity bias that is a function of the pattern projection angle on the meridional-vertical plane.
- The presence of the so-called “windowing effect” in the cross-correlation. Cross-correlation of two scintillation patterns over a finite interval causes apparent decorrelation. This is because the two scintillation patterns at two spaced receivers for the same finite time span are typically not the same. This effect is particularly evident when (i) the “random” characteristic velocity is not negligible, (ii) the scintillations are weak or (iii) the receivers’ noise is significant.

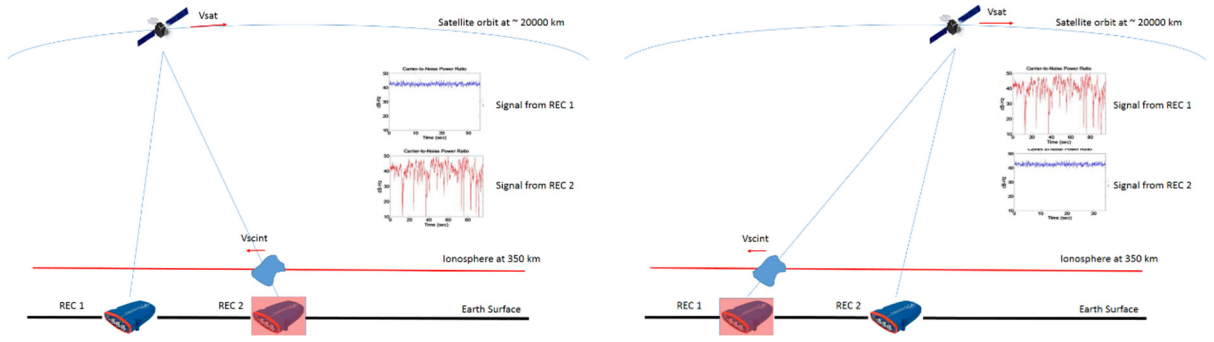

Figure 33. Schematic representation of the measurement of the ionospheric irregularities zonal velocity: the irregularity moves from right to left and encounter first the REC2 receiver (a) and then the REC1 receiver (b). The typical effect induced by the irregularity on the signal is plotted on top right part of both (a) and (b) panels (red curve) while blue lines represent the signal in "quiet" condition.

4.2 Algorithm description

Considering the geometry of the receivers, the local magnetic field lines and the position of the satellites, the equation of the zonal velocity of the ionospheric irregularities is function of the velocity of both the scintillation pattern and the satellites (Ledvina et al., 2004; Muella et al., 2009, 2013):

$$V_{ion} = \frac{h_{sat} - h_{ion}}{h_{sat}} V_{scint} + \frac{h_{ion}}{h_{sat}} \left[V_{satx} + \left(q_y / q_x \right) V_{saty} + \left(q_z / q_x \right) V_{satz} \right] \quad (4.1)$$

where V_{ion} is the zonal velocity of the ionospheric irregularities along the magnetic East-West direction, V_{scint} is the velocity of the scintillation pattern, V_{sat} is the satellite velocity vector that is projected on the receivers direction (coincident with the magnetic field reference frame) by the factors q_y/q_x and q_z/q_x. h_{sat} and h_{ion} are, respectively, the height of the satellites (about 20000 km) and the height of the thin ionospheric layer (assumed to be located at 350 km a.s.l.). Therefore, the estimation of V_{ion} is accomplished by measuring (i) V_{scint} from the cross-correlation of the signal amplitude and (ii) V_{satx},V_{saty},V_{satz}, from the orbital parameters in the RINEX navigational files.

Figure 34 shows a block diagram of the algorithm, developed in the framework of this thesis, to calculate V_{ion} starting from (i) the signal amplitude recorded by PRU1 and PRU3 (50 Hz SBF raw data) and (ii) the navigational information stored in the RINEX files. Light green shadow highlights the procedure applied to obtain V_{scint} and grey shadow covers the procedure for the estimation of V_{sat} both described in detail in the next two sections.

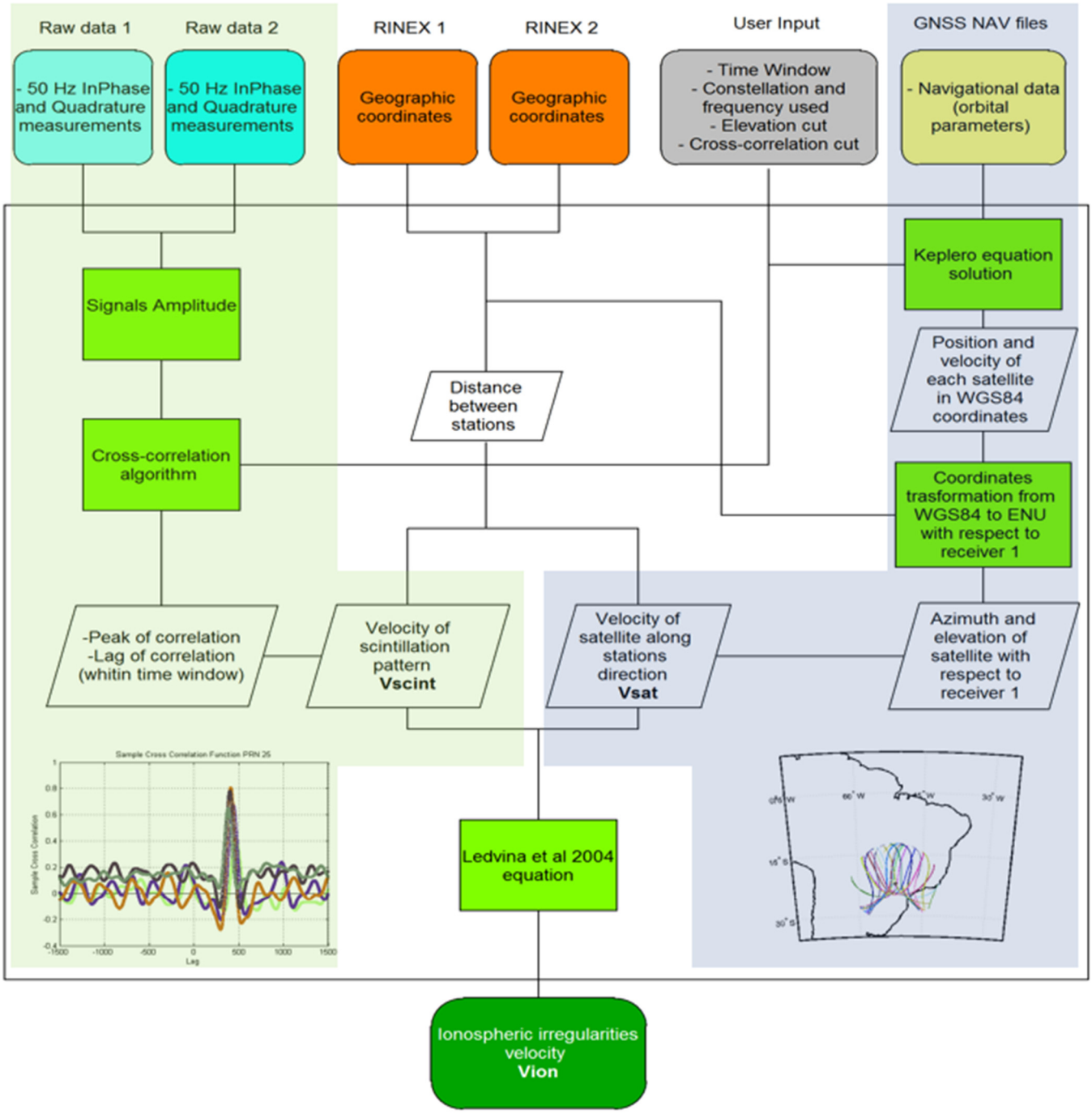

Figure 34. Block diagram of the algorithm for $\boldsymbol{V_{ion}}$ evaluation. Light green shadow highlights the procedure applied to obtain $\boldsymbol{V_{scint}}$ and grey shadow covers the procedure for the estimation of $\boldsymbol{V_{sat}}$.

4.2.1 Scintillation pattern velocity

To measure the similarity of two signals, e.g. waveforms as a function of time in which one of them has a time lag with respect to the other, cross-correlation technique is usually used in different application fields like pattern recognition, particle tracking etc. The cross-correlation can be defined, for two continuous functions, using the inner product of the function as:

$$C_{f,g}(\tau) \equiv \int_{-\infty}^{+\infty} f^*(t)\, g(t+\tau)\, dt \tag{4.2}$$

Where the asterisk denote the complex conjugate and τ is the time lag between the two functions. For discrete functions, e.g. a digital sampling of signals, the equation defining the cross-correlation function become:

$$C_{f,g}(n) \equiv \sum_{m=-\infty}^{+\infty} f^*(m)\, g(m+n) \tag{4.3}$$

In which n represents the lag between the functions in terms of sampling steps.

In this work, the cross-correlation function is used to determine the time delay between two signal. Once the cross-correlation function is calculated, in fact, the time at which the function maximize represents the lag in correspondence of which the signals are best aligned:

$$\tau_{delay} = \arg_t \max(\mathrm{C}_{f,g}(\mathrm{t})) \tag{4.4}$$

Starting from I and Q (in-phase and quadrature component of the signal) data recorded by the receivers every 0.02 seconds and stored in the SBF files, the equation used to reconstruct the signal amplitude is:

$$A_n(t_i) = \sqrt{I_n(t_i)^2 + Q_n(t_i)^2} \tag{4.5}$$

Where n=1, 2 is the ID of the stations and t_i is the sampling time. In this case, $t_{i+1} - t_i$ = 20 ms (50 Hz sampling frequency).

By selecting a suitable time window, it is possible to find the optimal correlation lag between the two signals. The selected time window should be the best compromise between avoiding false correlation peaks due to signal noise (too short time window) and signals de-correlation (too long time window). For the purpose of this study, the optimal time window is 60 s. Since each SBF file contains an hour of data, for every couple of files (one for each receiver) it is possible to obtain 60 different measures of the optimal cross-correlation time lag for each of the satellite in view. Figure 35 shows an example of cross-correlation vs. time lag for PRN 25 and five different couples of 1-minute data. For each correlation curve, the optimal time lag (peak in the cross-correlation) is detected and then V_{scint} is determined by applying the following:

$$V_{scint} = \frac{d_{ipp}}{t_{lag}} \tag{4.6}$$

Where d_{ipp} the distance between the two IPP 's, one for each receiver, of the investigated satellite and t_{lag} is the optimal time lag coming from the cross-correlation analysis. Under the reasonable hypothesis of $h_{sat} \gg h_{ion}$ and, for large elevation angles, d_{ipp} is equal to the distance of the stations at ground, d_{ground}.

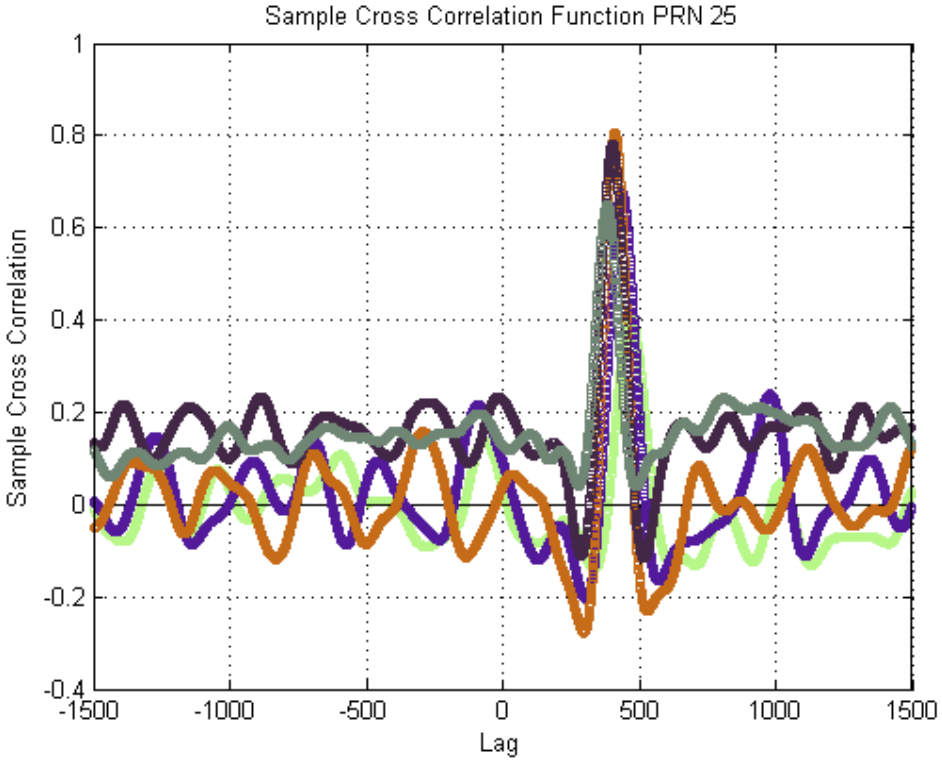

Figure 35. Example of the cross-correlation as a function of the time lag. Each curve represents the cross-correlation for a time window of 1 minute.

4.2.2 Satellites position and velocity

For an accurate determination of the velocity of the ionospheric irregularities, the computation of the position of the satellite on its orbit is crucial. This position can be determine, for each epoch, using the RINEX navigational files containing the orbital parameters for some reference time t_0 (changing day by day) broadcast by each satellite listed in Table 7 and sketched in Figure 36 and Figure 37**Errore. L'origine riferimento non è stata trovata.**. In first approximation, the orbit of the satellites can be evaluated applying Keplero's laws using the parameters listed in the left column of Table 7 and shown in Figure 36. However, the effect of other forces on the satellites (perturbation on Earth gravity field, Moon gravity force, solar radiation pressure etc.) results in a perturbation in the motion satellite. This perturbation can be evaluated using the parameters listed in the right column of Table 7 and sketched in Figure 37.

Table 7. Orbital parameters broadcast from each satellite in the navigational messages.

Parameter description	Parameter symbol	Parameter description	Parameter symbol
Reference time	t_0	**Variation Of Mean Angular Velocity**	Δn
Mean Anomaly	Mo	**Correction Coefficients**	cuc, cus, crc, crs, cic, cis
Square root of Semi-Major Axis	$\sqrt{a}$	**Rate Of Inclination Angle**	$\dot{I}$
Argument Of Perigee	ω	**Rate Of The Right Ascension**	$\dot{\Omega}$
Eccentricity	e		
Inclination	I_0		

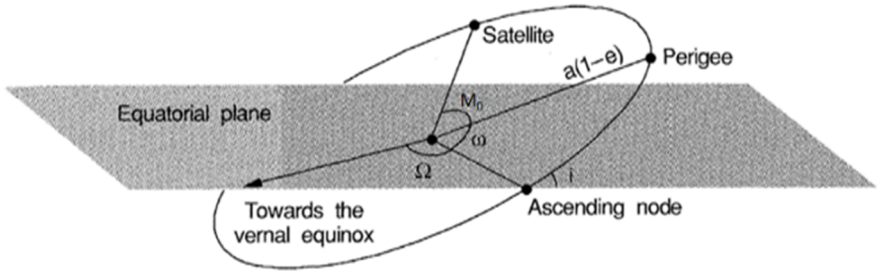

Figure 36. The elements of a keplerian orbit. From (Langley, 1991)

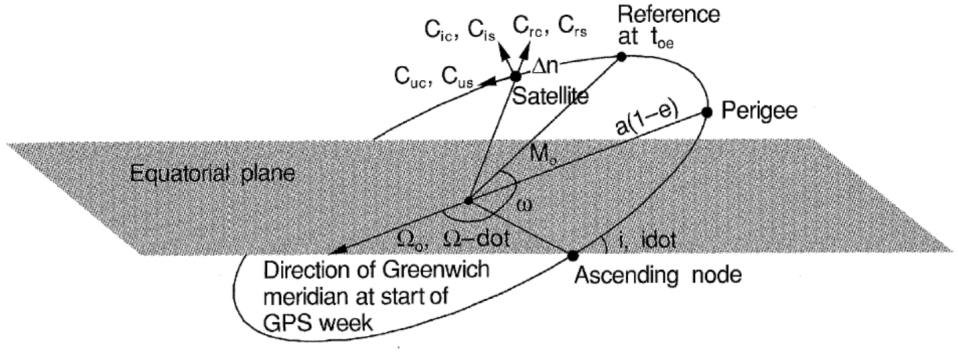

Figure 37. The parameters of the GPS broadcast ephemeris. From (Langley, 1991)

Starting from the information in the RINEX navigational files is it possible to determine the position and velocity of the satellite on its orbit and then in the WGS84 reference frame according to the following steps:

- Determination of the time difference between the reference time and epoch considered
- Computation of the mean motion using the parameter **a** (circular orbit)
- Computation of the mean anomaly starting from M_0 and Δn
- Evaluation of the Eccentricity anomaly by iteration process starting from parameter **e**
- Computation of the true anomaly $(\boldsymbol{\nu})$ starting from the eccentricity anomaly
- Computation of the longitude and radius correction using $\boldsymbol{\nu}$ **and correction coefficients**
- **Evaluation of the satellite position in the orbital plane**
- Determination of orbit inclination and longitude of ascending node at the epoch considered starting from $\boldsymbol{i}, \boldsymbol{i_0 \Omega_0}, \dot{\boldsymbol{\Omega}}$
- **Computation of satellite position and velocity in WGS84 reference frame**

The velocity of the satellite computed as just described, can be used to feed (4.1).

4.3 Micro Test Area

During the period September 2013 – February 2014 a measurement campaign has been organized in order to collect GNSS data for the evaluation of the zonal velocity of the ionospheric irregularities. Following the measurements and analysis method described in the previous section, data from this campaign have been processed to obtain information about the dynamics of small ionospheric irregularities. Description of the instruments, data availability and analysis and results are presented in this section.

4.3.1 Description

The regions mostly affected by scintillations are in the latitudinal range between 30°S and 10°N and in correspondence of longitudes between 300°E and 330°E, with particular strength over Sao Paulo States, due to the presence of the EIA southern crest. In addition, the finer URTKN and CIGALA climatology, described in the previous chapter, confirmed that Sao Paulo State was the best candidate to test the algorithms for the determination of the zonal velocity, developed during this PhD research period. Therefore, the MTA has been set up exploiting the already installed PRU1 receiver and deploying a new PolaRxS receiver (PRU3) for a six-month campaign from September 2013 to February 2014. Figure 38 shows the location of the MTA receivers, also listed in Table 8. MTA is located where the effects on GNSS signals due to the EIA southern crest are expected to maximize (-15°÷-20° magnetic degrees, orange lines). Moreover, MTA is located inside the SAMA, where the total geomagnetic field (purple lines) decreases, as particles precipitation from outer space due to SAMA is a further source of ionospheric turbulence affecting GNSS.

EIA and SAMA impact on GNSS is empowered and modulated by several geomagnetic storms and substorms occurred along the campaign, being larger in late February 2014, when the Dst reached about -120 nT. October, November and December 2013 are also characterized by moderate storms.

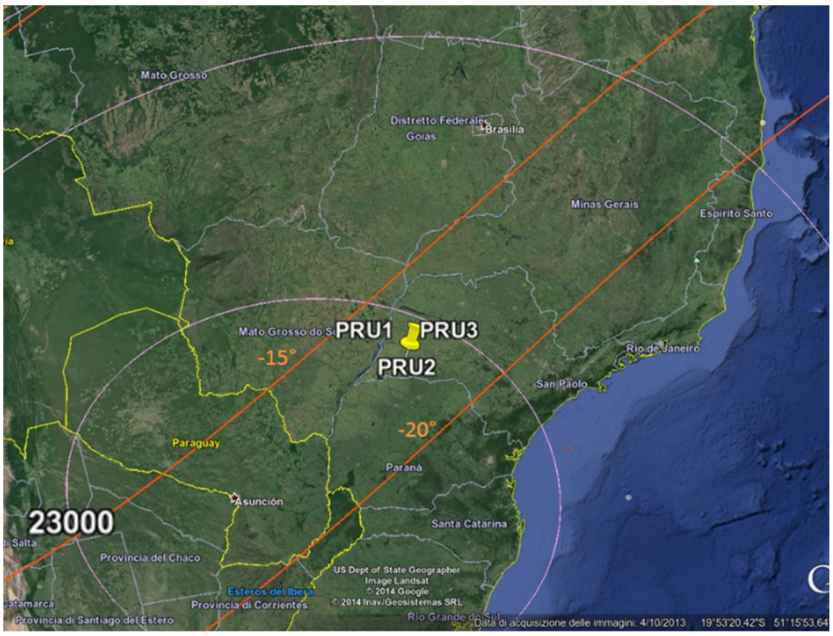

Figure 38. Location of the MTA receivers. The orange lines represents the position of the Dip Equator and of the magnetic parallels at -15° and -20° degrees, as indicated by the labels. The purple lines represent the intensity of the geomagnetic field at ground (in nT).

Table 8. List of the MTA stations and their geographic coordinates.

Station ID	Latitude (°N)	Longitude (°E)
PRU1	-22,120	-51,409
PRU3	-22,119	-51,406

Figure 39 is a zoom of Figure 38, detailing the relative position of the three MTA receivers. The red lines represent the approximate positions of both magnetic meridian and parallel at PRU1. The location of the newly deployed receiver (PRU3) was selected in order to be aligned with the magnetic E-W direction. Such a choice allows performing a measurement of the zonal velocity of the ionospheric irregularities as described in the previous sections.

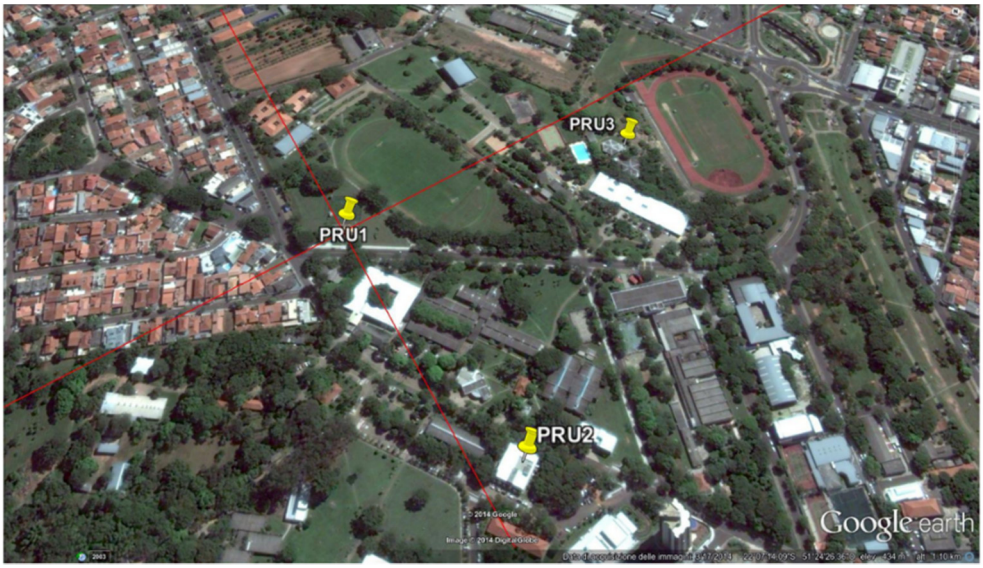

Figure 39. Zoom of Figure 38, detailing the relative position of the three MTA receivers. Red lines are the approximate positions of the magnetic meridian and parallel passing over PRU1 receiver.

4.3.2 Data availability

The PolaRxS is a multi-frequency, multi-constellation receiver capable of tracking simultaneously GPS L1CA, L1P, L2C, L2P, L5; GLONASS L1CA, L2CA; GALILEO E1, E5a, E5b, E5AltBoc; COMPASS B1, B2; SBAS L1 (Bougard et al., 2011). Sampling at 50 Hz, the receiver gives the following main output parameters:

8. the σ_Φ phase scintillation index calculated over different time intervals (1, 3, 10, 30, 60 seconds);
9. the S_4 amplitude scintillation index calculated over 60 seconds;
10. the TEC and ROT every 15 seconds,
11. the spectral parameters: spectral slope of the phase Power Spectral Density (p) in the 0.1 to 25Hz range and the spectral strength of the phase PSD (T) at 1 Hz (60 seconds);
12. the Standard Deviation of the Code Carrier (CCSTDDEV - 60 seconds) ;
13. the Carrier to noise ratio (60 seconds);
14. locktime (60 seconds).

All these quantities (except TEC and ROT) are calculated for all the available signal frequencies emitted by the satellites and along the slant path connecting receiver and satellite. TEC values are obtained by the pseudorange measurements only. For GPS, the TEC is based on the L2-P and L1-P pseudoranges; for GLONASS it is based on the L1-C/A and L2-C/A pseudoranges and for GALILEO, it is based on the L1BC and E5a. ROT is computed from the carrier phase measurements only, and hence is much more accurate than TEC.

As already mentioned, the MTA campaign took place between September 2013 and February 2014. The period has been chosen in order to get the worst ionospheric conditions during the equinox and austral summer in accordance with the climatological study as reported before. The data acquisition was almost continuous and only few data gaps have been encountered. As shown in Figure 40, the percentage of days of data available was above 90% for the two receivers. The monthly percentage of days with available data is in Figure 41 (panel a), which confirms the homogeneous distribution of the data as a function of the month.

To perform the measurement of the zonal velocity of the ionospheric irregularities, the simultaneous availability of PRU1 and PRU3 data is necessary. Figure 41 (panel b) reports the simultaneous availability of the data from the two receiver month by month in order to show that measurements are sufficient to perform the analysis of the zonal velocity for all the period covered by the measurements campaign.

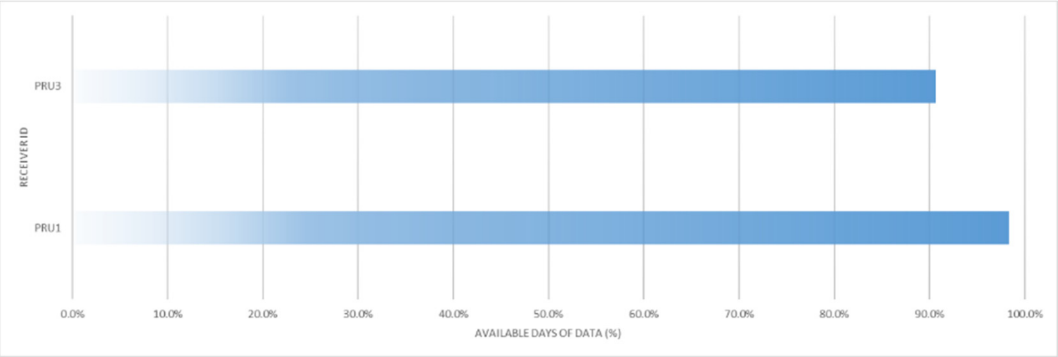

Figure 40. Percentage of days of data available from the MTA receivers in the period September 2013- February 2014.

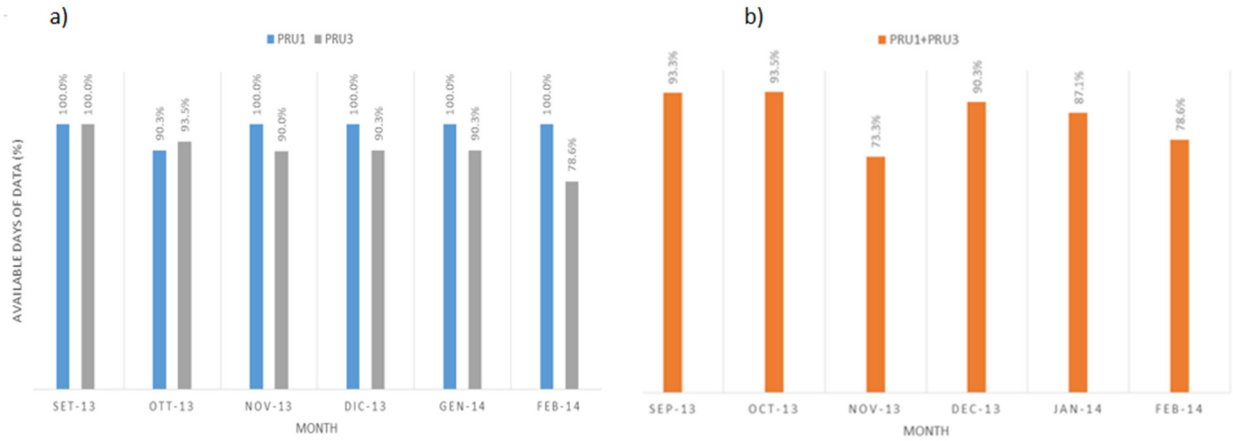

Figure 41. Percentage of days of data available from the MTA receivers as a function of the month (a) and percentage of data simultaneously available from PRU1 and PRU3 (b)

4.4 Results

To characterize the dynamics of the small-scale ionospheric irregularities over the MTA area, a measurements campaign was performed during the period September 2013 – February 2014 acquiring data from 22 UT to 04 UT (post-sunset hours). This period was chosen to investigate the dynamics of the ionosphere during the seasons and the hours of maximum scintillation activity as highlighted in the previous chapter. For this purpose, in-phase (I) and in quadrature (Q) L1 raw data from the PRU1 and PRU3 receivers has been analysed to obtain information about the zonal velocity of the ionospheric irregularities of the order of the Fresnel scale (about 250 m). These two receivers, in fact, are deployed roughly along the East-West magnetic direction. The assumption to carried out the analysis proposed here is that the irregularities are elongated in the direction of the magnetic field with a velocity vector along E-W magnetic direction (Kintner, 2004).

Applying the algorithm described in the previous section, zonal velocity (V_{ion}) of the irregularities is computed each minute using the signal form each satellite simultaneously acquired by PRU1 and PRU3 but during the analysis two different cut-off have been applied. According to the hypothesis that the distance of the IPP's d_{1-2}, is equal to the distance of the stations on ground (d_{ground}), formulated in previous section, data from lowest elevation angles (below 60°) is not considered in the results presented here. The second cut-off is applied on the values of the peak of the cross-correlation. According to the frozen-in hypothesis, only correlation with a peak value greater than 0.8 are considered in this work. Correlation with low peak value could be due to the variability on the shape of the irregularities as they move between receivers leading to a significant "random" characteristic velocity.

4.4.1 Comparison with indipendent measurements

To validate the results, a comparison with Jicamarca Incoherent Scatter Radar (ISR, dip latitude 0.05° S) and Boa Vista Ionosonde (dip latitude 12°N) measurements has been performed. Figure 42 shows the location of the instruments used to perform the comparison, highlithing their position with respect to the magnetic equator (red line in the Figure 42). Considerng measurements acquired during all the campaign, hourly mean and standard deviation of the GNSS data is performed in order to check the compatibility with the other measurements. Figure 43 shows in red line the zonal velocity coming from MTA GNSS measurements analisys, in blue line the Incoherent scatter radar data and in black line the measeruments coming from the ionosonde. The behaviour of the GNSS zonal velocity is in agreement with the other ones but some differences in the magnitude can be noted. These differences could be due to two main reasons:

- Differences in the dynamics of the plasma at different locations: ISR is located on the magnetic equator, the ionosonde is on the northern crest of the Equatorial Ionization Anomaly (EIA) while the GNSS receivers is deployed on the southern crest of EIA area

- Different wavelengths used by the three instruments to investigate the plasma dynamics. The frequency of the signal used by the instruments, determines the scale of the irregularities affecting the signal propagation. As reported in Figure 42, the three instruments investigate the zonal velocity of irregularities with different sizes that could have a relative motion to each other, i.e. different velocities.

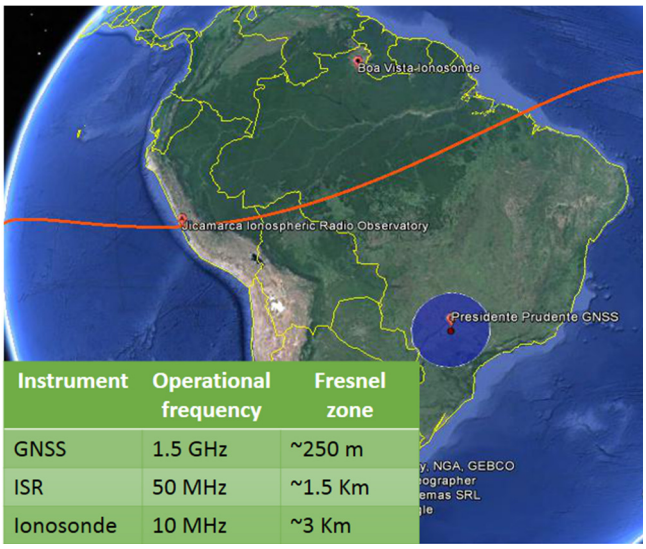

Instrument	Operational frequency	Fresnel zone
GNSS	1.5 GHz	~250 m
ISR	50 MHz	~1.5 Km
Ionosonde	10 MHz	~3 Km

Figure 42. Location of the MTA, of the Jicamarca ISR and of the Boa Vista Ionosonde. Blue circle represents the area spanned from data with elevation greater than 60°. Table in the left-bottom corner report the operational frequency and the dimension of the first Fresnel zone for each instrument.

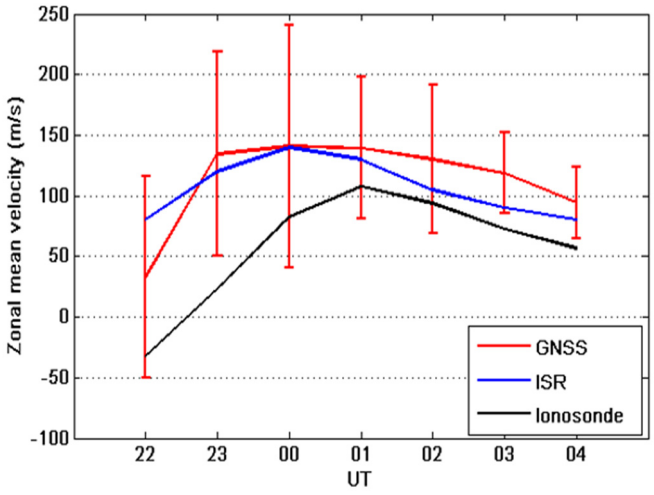

Figure 43.Hourly mean of the ionospheric irregularities zonal velocity as measured by MTA GNSS receivers (red line), by Jicamarca ISR (blue line) and Boa Vista Ionosonde (black line).

Zonal velocity over the MTA region, reaches its maximum at midnight (21 LT) as well as the variability of the velocity itself, as highlighted by the standard deviation (red bar in Figure 43).

4.4.2 *Zonal velocity and scintillations occurrence*

Figure 44 shows the relationship between the hourly mean of the zonal velocity of the small-scale ionospheric irregularities and the hourly mean of the occurrence of $S_4 > 0.25$. Statistical analysis on the scintillations occurrence is performed taking into account data from PRU1. It is clear that the two quantities are strictly related, as their behaviour is quite similar during the post-sunset hours. This relationship suggests that the scintillations events are driven not only by TEC gradients, as highlighted in the previous chapter, but also by an "advective" term related to the velocity of the ionospheric plasma.

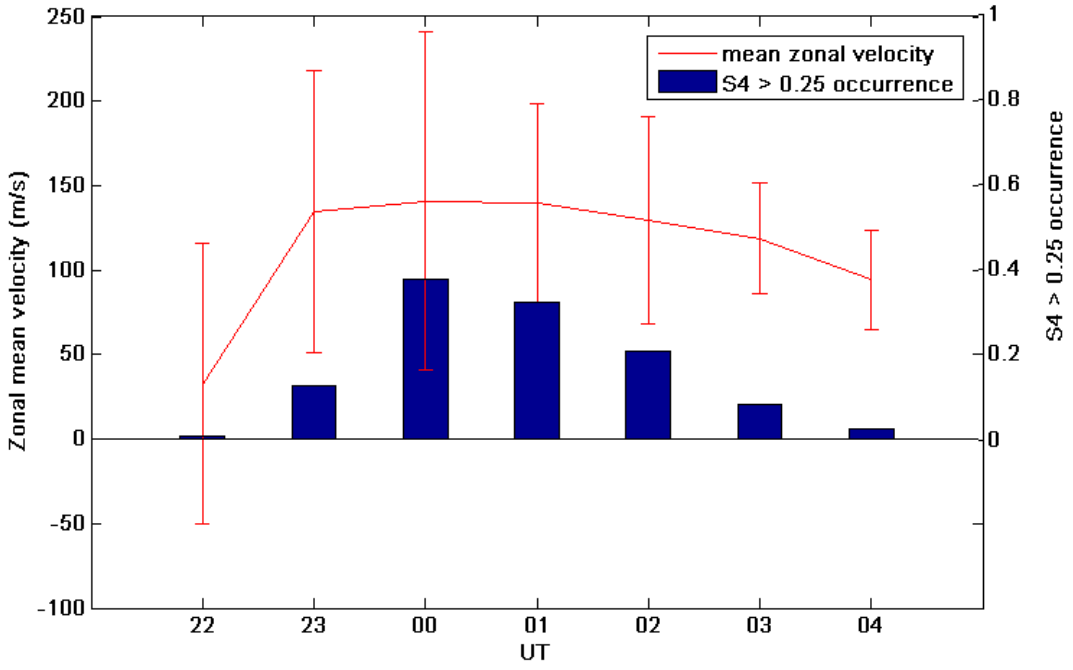

Figure 44. Mean value of the zonal velocity of ionospheric irregularities and occurrence of S4 above 0.25 as a function of the Universal Time (LT=UT-3).

To confirm the relationship between S_4 occurrence and V_{ion}, the analysis of the seasonal variability of these two quantities is carried out. Figure 45 and Figure 46 show the hourly mean of S_4 occurrence and the hourly mean of the velocity V_{ion} respectively, obtained by considering data from September-October 2013 (blue lines), November-December 2013 (green lines) and January-February 2014 (red lines). As well as for the overall comparison, also the seasonal behaviour of the S_4 occurrence and zonal velocity seems to be similar over the MTA region. This analysis confirm not only the dependence of the scintillations from the plasma dynamics but also that the scintillations activity reach its maximum on spring and summer. The velocity V_{ion} maximizes also in spring/summer with an evident difference with respect to the other season at least until 01 UT. From 02 UT to 04 UT, when the scintillations activity decreases, the differences among seasons become smaller.

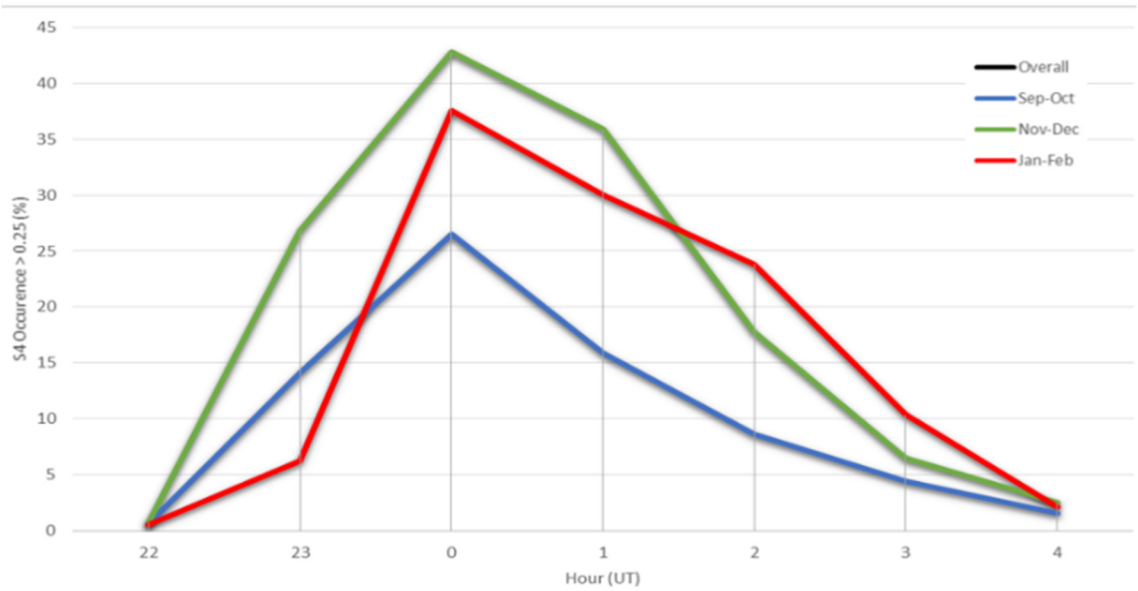

Figure 45. Occurrence of S4 above 0.25 as a function of UT (LT=UT-3) obtained by considering the whole dataset (black line) and by considering data from September 2013 and October 2013 measurements (blue line), from November 2013 and December 2013 measurements (green line) and from January 2014 and February 2014 (red line).

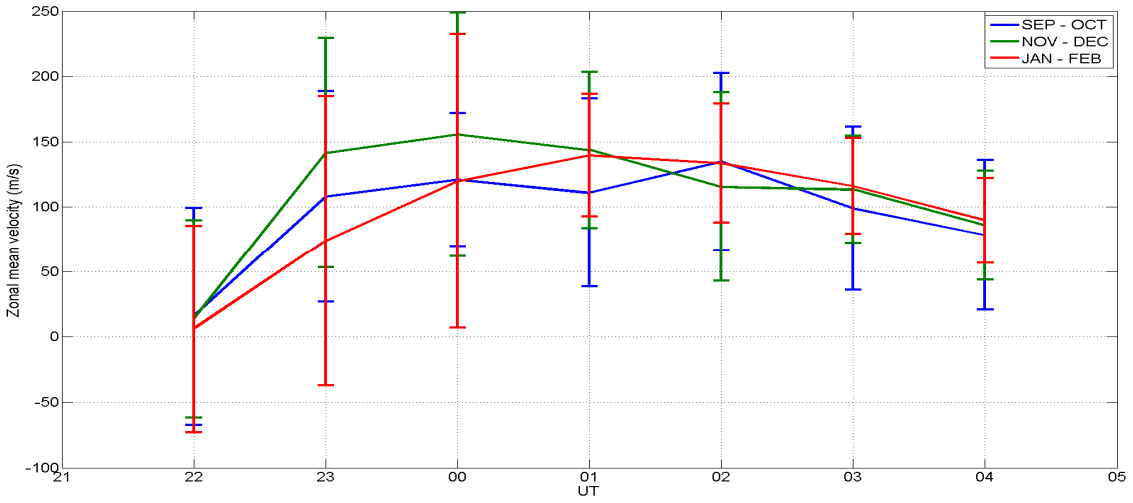

Figure 46. Mean of the ionospheric irregularities zonal velocity as a function of UT (LT=UT-3) obtained by considering the whole dataset (black line) and by considering data from September 2013 and October 2013 measurements (blue line), from November 2013 and December 2013 measurements (green line) and from January 2014 and February 2014 (red line).

4.5 Conclusions

The analysis of the dynamics of the small-scale ionospheric irregularities by means of high sampling frequency data from two GNSS receivers is analysed in this chapter. The work can be divided into 2 main phases:

1) Development of the algorithm to estimate the zonal velocity of the irregularities starting from raw GNSS data and its validation by means of the comparison with independent measurements
2) Study of the correlation between zonal velocity of the irregularities and scintillation occurrence

The main features resulting can be summarized as follows:

1. Data acquired by two spaced receivers (distance≈300 m) displaced along magnetic E-W direction every 20 ms can be used to investigate the dynamics of the ionosphere at low latitude.
2. Velocity inferred by the correlation of spaced receivers data is in good agreements with independent measurements performed using different instrument and technique (Figure 43).
3. Some differences between velocity inferred with different instruments and in different low latitude region (northern crest, equator and southern crest) can be observed. These differences are primarily due to:
    - Differences in the dynamics of the plasma in different latitudes. ISR and ionosonde measurements presented here are performed in equatorial and southern crest region respectively.
    - Different behaviour of the irregularities of different size. Each technique can probe the dynamics of irregularities of different size depending on the frequency of the electromagnetic wave used by each instrument (Figure 42).
4. During the first hour of the post sunset period (22 UT, 19 LT) V_{ion} can assume negative values. This is due to the fact that at post sunset the velocity of the ionospheric plasma reverses from westward to eastward direction.
5. Clear relationship between zonal velocity of the small-scale ionospheric irregularities and amplitude scintillation occurrence exists. Both S_4 occurrence and V_{ion} reach their maximum at midnight (UT) to decrease until the end of the post sunset period (04 UT).
6. Moreover, the seasonal behaviour of S_4 occurrence and V_{ion} is very similar. Both quantities reach their maximum during local spring (November-December) confirming also what highlighted in the previous chapter.

4.6 References

Basu, S., Kudeki, E., Basu, S., Valladares, C. E., Weber, E. J., Zengingonul, H. P., Bhattacharyya, S., Sheehan, R., Meriwether, J. W., Biondi, M. A., Kuenzler, H. and Espinoza, J.: Scintillations, plasma drifts, and neutral winds in the equatorial ionosphere after sunset, J. Geophys. Res., 101(A12), 26795, doi:10.1029/96JA00760, 1996.

Bougard, B., Sleewaegen, J., Spogli, L. and Nazionale, I.: CIGALA : Challenging the Solar Maximum in Brazil with PolaRxS, Compass, 2572–2579 [online] Available from: http://www.ion.org/search/view_abstract.cfm?jp=p&idno=9810 (Accessed 5 November 2014), 2011.

Costa, E., Fougere, P. and Basu, S.: Cross-correlation analysis and interpretation of spaced-receiver measurements, Radio Sci. [online] Available from: http://onlinelibrary.wiley.com/doi/10.1029/RS023i002p00141/full (Accessed 5 November 2014), 1988.

Kil, H., Kintner, P. M., de Paula, E. R. and Kantor, I. J.: Global Positioning System measurements of the ionospheric zonal apparent velocity at Cachoeira Paulista in Brazil, J. Geophys. Res., 105(A3), 5317, doi:10.1029/1999JA000244, 2000.

Kintner, P. M.: Size, shape, orientation, speed, and duration of GPS equatorial anomaly scintillations, Radio Sci., 39(2), n/a–n/a, doi:10.1029/2003RS002878, 2004.

Langley, R. B.: The orbits of GPS satellites, GPS World, 1991.

Ledvina, B. M., Kintner, P. M. and De Paula, E. R.: Understanding spaced-receiver zonal velocity estimation, J. Geophys. Res. Sp. Phys., 109(A10), A10306, doi:10.1029/2004JA010489, 2004.

Muella, M. T. a H., de Paula, E. R., Kantor, I. J., Rezende, L. F. C. and Smorigo, P. F.: Occurrence and zonal drifts of small-scale ionospheric irregularities over an equatorial station during solar maximum - Magnetic quiet and disturbed conditions, Adv. Sp. Res., 43(12), 1957–1973, doi:10.1016/j.asr.2009.03.017, 2009.

Muella, M. T. a H., de Paula, E. R. and Monteiro, A. a.: Ionospheric Scintillation and Dynamics of Fresnel-Scale Irregularities in the Inner Region of the Equatorial Ionization Anomaly, Surv. Geophys., 34(2), 233–251, doi:10.1007/s10712-012-9212-0, 2013.

Rino, C. L. and Livingston, R. C.: On the analysis and interpretation of spaced-receiver measurements of transionospheric radio waves, Radio Sci., 17, 845, doi:10.1029/RS017i004p00845, 1982.

Wernik, a. W., Alfonsi, L. and Materassi, M.: Scintillation modeling using in situ data, Radio Sci., 42(1), n/a–n/a, doi:10.1029/2006RS003512, 2007.

Yeh, K. C. and Liu, C. H.: Radio Wave Scintillations in the Ionosphere., Proc. IEEE, 70, 324–360, doi:10.1109/PROC.1982.12313, 1982.

5. NeQuick model validation over Tucuman (Argentina)

Ionosphere is, as widely stressed within this thesis, the main error source in GNSS based positioning. Using dual frequency receivers able to use both L1 and L2 to compute their position partially solve this problem (first order ionospheric error) but, unfortunately, almost all of the commercial receivers is, nowadays, single frequency apparatus. This limitation is mainly due to the high cost of the dual frequency receivers that are no suitable for the end-users applications. Since the introduction of the GPS constellations, the approach to try to solve the ionospheric errors in single frequency receivers was using a model able to describe the ionospheric contribution affecting the signal during the flight between satellite and receiver (Dubey et al., 2006; Klobuchar and Abdu, 1989; Klobuchar, 1987). Klobuchar model used to correct ionospheric delay in single frequency GPS is able to correct about 50% of the delay introduce by the ionosphere in the GNSS acquisitions. Moreover, Klobuchar model completely fails to describe the behaviour of the ionosphere in low latitude regions.

For this reason, European Space Agency (ESA), adopts the NeQuick model (described in chapter 2) to correct the ionospheric delay in the new GALILEO constellation (Radiceila, 2009; Radicella et al., 2008). This model, differently from the Klobuchar, is able to describe the Equatorial anomaly ionization but, being a climatological model, is not always able to correct the effects of the low latitude irregularities. Some data ingestion technique was applied to drive the model to a better estimation of the TEC (Bidaine and Warnant, 2011; Nava et al., 2011; Yue et al., 2011) but further work is required to validate and improve the performance of the NeQuick in terms of TEC and ionospheric delay estimation especially in the equatorial and low latitude region.

In this work, using data from an ionosonde and a GNSS receiver located in Tucuman (Argentina) and applying a selection based on the technique recently introduced (Cesaroni et al., 2013), a validation of the NeQuick model within the southern crest of EIA is done.

5.1 Data and method

In order to study the performance of the NeQuick model in the low latitude regions, data coming from co-located ionosonde and GNSS receiver installed in Tucuman (Argentina, 26°50'S 65°12'W, dip latitude 13° S) have been used. As described in the chapter 2, NeQuick model generates vertical profiles of electron density starting from some ionospheric parameters (f_oF2 and M(3000)F2) modelled using ITU-R coefficients. For the purpose of this work, a modified version of the NeQuick has been created in order to use measured parameters instead of modelled ones. In particular, this modified NeQuick is able to ingest data coming from ionograms recorded by Tucuman ionosonde and analysed by Autoscala software (described in section 2.2.3). A subroutine of the NeQuick software is able to integrate the vertical profile in order to provide the TEC along a given ray-path. Integrating the profile between ground and about 20000 km (mean height of the GNSS satellite) in the vertical diretion is possible to obtain a vTEC value to be compared with the calibrated vTEC

(see section 3.1.3) obtained by GNSS measurements. Therefore, in this work, calibrated TEC from GNSS is assumed as the "true" ionospheric electron content. In order to evaluate the improvements of the performance of the modified version of NeQuick in terms of TEC, a suitable method to select only the "correctly" scaled ionograms is applied. This original method, developed in the framework of this thesis, is reported in Cesaroni et al., 2013 and briefly described in the next section.

5.1.1 Data selection

The method used in this work is based on the calculation of contrast, a parameter generally applied in image recognition techniques. This is used by Autoscala for assessing the similarity of an empirical curve with the recorded trace. Here, the same method is used to quantify the similarity of the trace reconstructed by Autoscala to the recorded ionograms.

Initially the ionogram is loaded by Autoscala as a matrix *A* of *n* columns and *m* rows which numbers are defined by the following formulas:

$$n = \mathrm{int}\left[\frac{f_f - f_0}{\Delta f}\right] + 1 \tag{5.1}$$

$$m = \mathrm{int}\left[\frac{h'_f - h'_0}{\Delta h'}\right] + 1 \tag{5.2}$$

Where f_f,h'_f, f_0, h'_0, and Δf are final frequency, final virtual height, initial frequency, initial virtual height, and frequency step of the sounding, respectively. $\Delta h'$ is the height resolution at which the sounding has been recorded. The element a_{xy} (with x=1,…,m and y=1,…, n) of the matrix A is an integer. The higher the value, the stronger the echo amplitude received by the ionosonde.

At the end of the automatic interpretation process, Autoscala adapts the parameters of a model providing an electron density profile $N_e(h)$ from which it reconstructs the ordinary trace fitting the recorded one (Scotto, 2009).In this work the reconstruction of the extraordinary trace starting from the same $N_e(h)$ and using the appropriate refractive index is also performed.

Two other matrices, of the same dimensions as A, is generated to collect the two restored traces. O and X are the matrices storing the ordinary and the corresponding extraordinary restored traces, respectively. In these matrices, if *I* and *j* correspond to coordinates of one point of the ordinary (extraordinary) trace, O_{ij}=1 (X_{ij}=1) is set, otherwise O_{ij}=0(X_{ij}=0).

Furthermore, using the reconstructed traces from Autoscala, the first derivatives $T'_{ord}(k)$ and $T'_{ext}(k)$ for the k-th element of the ordinary and extraordinary trace is calculated through the relations:

$$T'_{\mathrm{ord}(k)} = \frac{h'_{\mathrm{ord}(k+1)} - h'_{\mathrm{ord}(k)}}{f_{\mathrm{ord}(k+1)} - f_{\mathrm{ord}(k)}} \tag{5.3}$$

$$T'_{\mathrm{ext}(k)} = \frac{h'_{\mathrm{ext}(k+1)} - h'_{\mathrm{ext}(k)}}{f_{\mathrm{ext}(k+1)} - f_{\mathrm{ext}(k)}} \tag{5.4}$$

The first derivatives calculated above are used to discern the parts of traces that have a slope higher than those closer to being horizontal. For this purpose a fixed threshold Γ is imposed that if $T'_{ord(i)} > \Gamma$ ($T'_{ext} > \Gamma$) the ordinary (extraordinary) trace is next to be vertical, otherwise the traces is considered as being near horizontal. $\Gamma$is empirically determined (Γ=60).

At this point, contrasts C_{ord} and C_{ext} for ordinary and extraordinary traces can be calculated. The computation can be formalized by the following expressions:

$$C_{\mathrm{ord}} = N_{\mathrm{ord}} \left\{ \sum_{i=1}^{N} \sum_{j=1}^{M} \mathcal{H}\left(-T'(f) + \Gamma\right) O_{ij} SEC_{ij} + \mathcal{H}\left(T'(f) - \Gamma\right) O_{ij} SEC_{ij} \right\} \tag{5.5}$$

$$C_{\mathrm{ext}} = N_{\mathrm{ext}} \left\{ \sum_{i=1}^{N} \sum_{j=1}^{M} \mathcal{H}\left(-T'(f) + \Gamma\right) X_{ij} SEC_{ij} + \mathcal{H}\left(T'(f) - \Gamma\right) X_{ij} SEC_{ij} \right\} \tag{5.6}$$

Where $\mathcal{H}(q)$ is the Heaviside function:

$$\mathcal{H}(q) = \begin{cases} 1 & q > 0, \\ 0 & q < 0. \end{cases} \tag{5.7}$$

The normalization terms

$$N_{\mathrm{ord}} = \left(6 \sum_{i=1}^{N} \sum_{j=1}^{M} O_{ij} \right)^{-1} \tag{5.8}$$

$$N_{\mathrm{ext}} = \left(6 \sum_{i=1}^{N} \sum_{j=1}^{M} X_{ij} \right)^{-1} \tag{5.9}$$

allow the value of the contrast to be independent from the numbers of points (echos) composing the trace.

The quantity *SEC* (Single Element of Contrast)

$$SEC_{ij} = 6a_{ij} - a_{i,j-3} - a_{i,j-2} - a_{i,j-1} - a_{i,j+1} - a_{i,j+2} - a_{i,j+3} \tag{5.10}$$

represents the contribution to the contrast due to a single point of the reconstructed trace. The parameters C_{ord} and C_{ext} give a numerical estimation of the degree at which the reconstructed traces are distinguished with respect to the background. In other words C_{ord} and C_{ext} permit evaluation of the quality of the Autoscala reconstructed traces: the higher the contrast , the better the reconstruction of the considered trace.

The equations above can be interpreted by observing that the difference between the value of each element of the trace matrix a_{ij} and the surrounded points is computed by considering the elements of the same column if $T'_{ord(i)}<\Gamma(T'_{ext(i)}<\Gamma)$, otherwise the points of the same row.

To better understand the significance of the contrast that is used, below is presented three examples of different situations in the matrix that represent the recorded ionograms and the corresponding calculations of the *SEC*.

Figure 47 illustrates the 3 above mentioned conditions where a single point belonging to a reconstructed trace produces different values of *SEC*. It is supposed that the point considered corresponds to row *i** and column *j**, so that we have $o_{i^*j^*}=1$ (or $x_{i^*j^*}=1$). Figure 47 (panel a) represents the best possible situation: $a_{ij}=255$ (black pixel) and the surrounding points are all zero (white pixels). The direction along which surrounding pixels are considered (vertical or horizontal) depends on the values of the derivative. For this case it results:

$$SEC_{i^*j^*} = \frac{(6*255 - 0 - 0 - 0 - 0 - 0 - 0)}{6} = 255 \tag{5.11}$$

Figure 47 (panel b) shows the worse possible situation: $a_{i^*j^*} = 0$ and the elements around is equal to 255. In this case $SEC_{i^*j^*}$ is:

$$SEC_{i^*j^*} = \frac{(6*0 - 255 - 255 - 255 - 255 - 255 - 255)}{6} = -255 \tag{5.12}$$

Figure 47 (panel c) describes an intermediate situation in which $A_{i^*j^*} = 192$ and where some surrounded points are equal to zero whereas others are equal to intermediate values. In this case, *SEC* can be written as:

$$SEC_{i^*j^*} = \frac{(6*192 - 0 - 64 - 0 - 0 - 0 - 128)}{6} = 170 \tag{5.13}$$

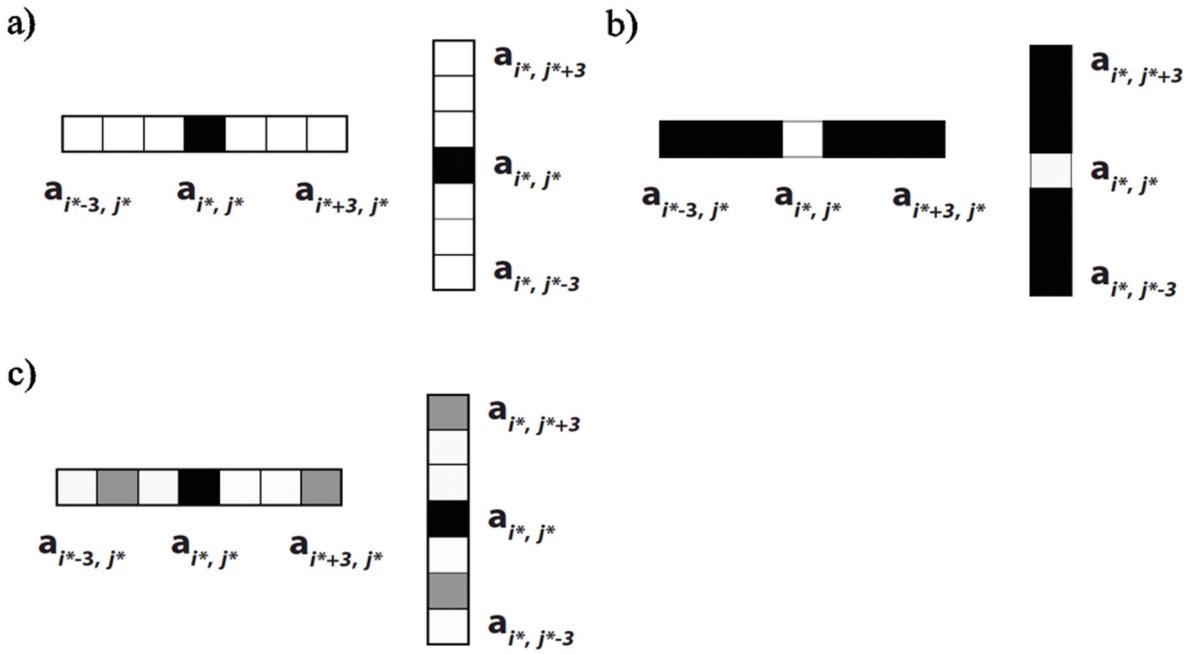

Figure 47. Schematic representation of possible situations for SECi*j* computation for a point of the restored trace corresponding to the entry ai*j* of the matrix A, in which the observed ionogram is stored. The best situation is when ai*j* =255 and all the elements around it, both those in horizontal and in vertical, are zero (a); in this case the maximum possible value of SECi*j*=(6•255-0-0-0-0-0-0)/6=255 is reached. The worst situation is when ai*j* =0 and all other elements around are equal to 255 (b), in which case the minimum possible value of SECi*j*=(6•0-255-255-255-255-255-255)/6=-255 is touched. In general traces is in an intermediate situation; here an example with ai*j* =170 is presented, having some entries around it with non-zero value; in this case there is an intermediate value of SECi*j*=(6•192 -0-64-0-0-0-128)/6=160.

5.2 Results

5.2.1 Quality evaluation for f_0F2 given by Autoscala

A database of about 4,000 ionograms from 2013 to 2014 recorded at the ionospheric station of Tucuman was selected, including all seasons and all hours of the day. Figure 48 shows the probability that the difference between f_oF2 provided by Autoscala and the corresponding f_oF2 obtained by an operator is less than 0.5 MHz. These values give an estimation of the probability distribution associated with automatically provided f_oF2 and so represents a good parameter for defining the accuracy of the autoscaled f_oF2.

For C_{ord}> 170 the number of available data was extremely small, so that the obtained graph is not significant. Instead, for C_{ord}< 0 the relationship between contrast and probability described above is not well defined and these values are not included in Figure 49.

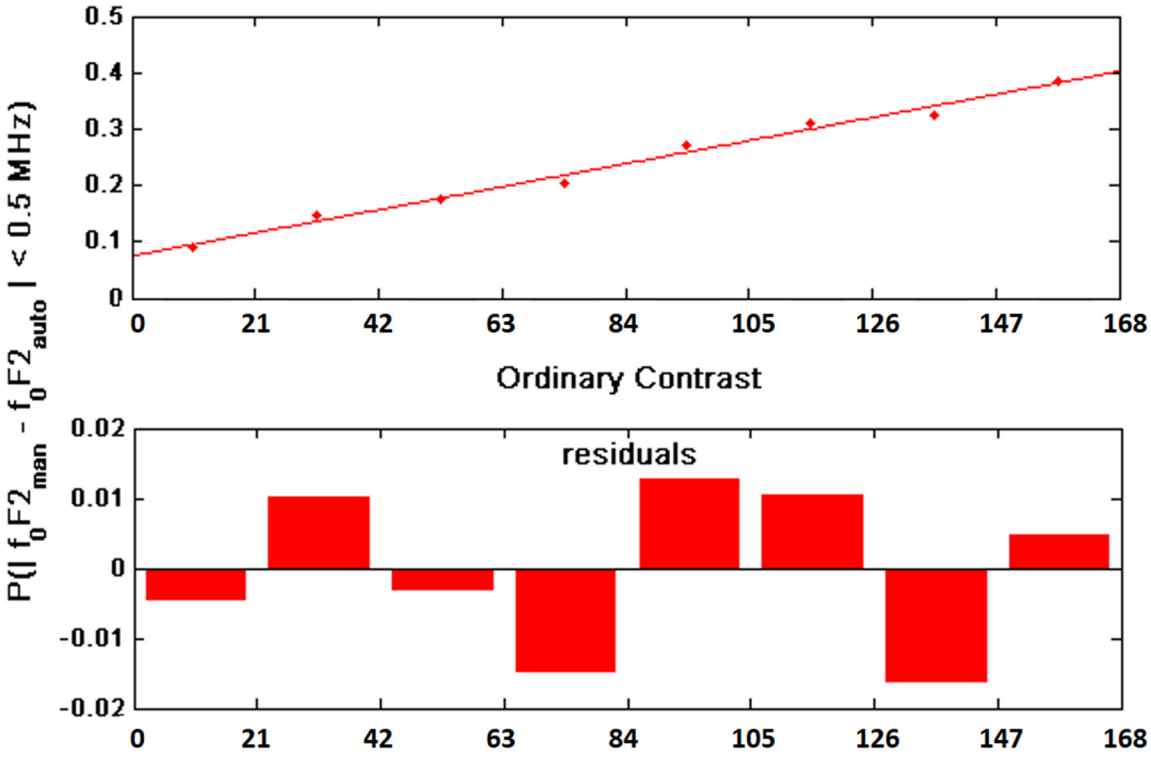

Figure 48. Probability that autoscaled and manual scaled differ of less than 0.5 MHz vs C_{ord}. The bottom panel represents the residual associated with the fitting curve shown in the top panel.

Besides, as shown in Figure 48, the variable C_{ord} also allows to evaluate, for a given automatically obtained f_oF2, the probability $P(|f_oF2_{aut}-f_oF2_{man}|)<\alpha$. Of particular interest is the estimation of the probability for α = 0.5 MHz, which is the manual scaling error accepted, according to the standard URSI. Therefore, this technique allows assigning a quality factor in a probabilistic sense, which can be added as an output to the f_oF2 given by Autoscala.

In this work, C_{ord} is used to evaluate the goodness of the autoscaled parameters to establish if they are suitable as input of the NeQuick model TEC modelling.

5.2.2 Comparison between GNSS TEC and NeQuick TEC over Tucuman

The performance of the NeQuick model in terms of vTEC computation at low latitude regions is evaluated, in this work, by means of the comparison between vTEC computed by the model itself and vTEC derived from RINEX files containing GNSS measurements. This comparison is performed in three different way in order to evaluate the improvements of the model when it can ingests measured parameters (f_oF2 and M3000F2) and, in addition, when a proper data selection method is applied (see previous section).

Figure 49 shows the steps following which the datasest for the 3 cases used for the comparison is construct. Case 1 dataset includes vTEC values coming from the original version of model, i.e. using modelled ionospheric parameters f_oF2 and M3000F2 to generate the electron profiles. Case 2 dataset includes vTEC values coming from the modified version of the model. These vTEC are computed integrating the vertical electron profiles generating starting from the f_oF2 and M3000F2 inferred by Autoscala analysing Tucuman ionograms. Case 3 dataset is a subset of the case 2 dataset including only parameters coming from ionograms with C_{ord} greater then a given threshold. In this work the selected threshold is equal to 105 to ensure that $P\left(\left|f_0F2_{man} - f_0F2_{auto}\right| < 0.5MHz\right)$ is greater than 30%. The three datasets are built considering a period spanning 2013 and 2014 to study the behaviour of the model during the maximum of the solar activity.

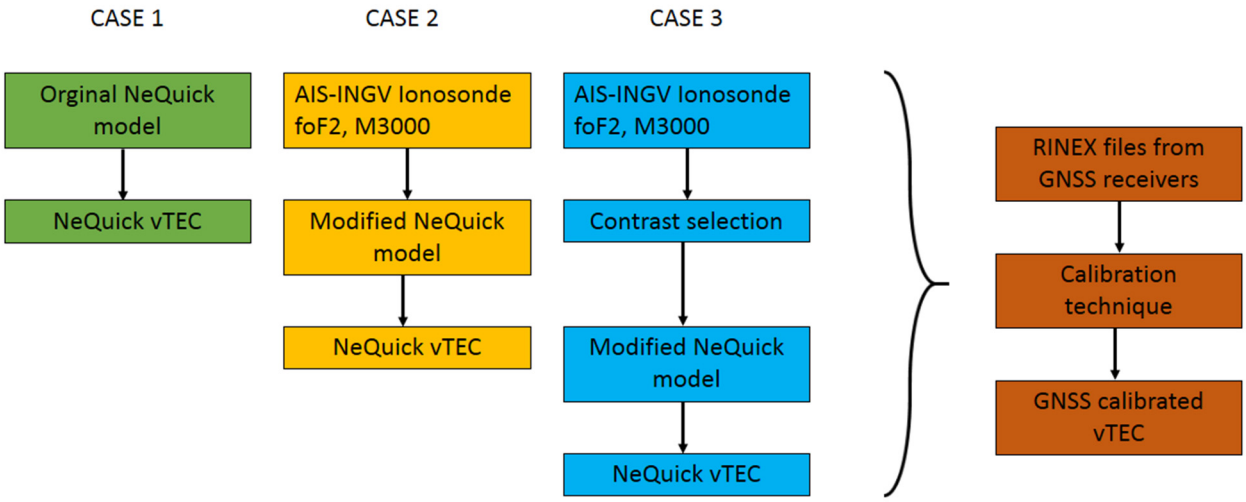

Figure 49. Block scheme describing the 3 different vTEC datasets from the NeQuick model used for the comparison with the GNSS vTEC.

All the datasets described above are separately compared with the vTEC obtained following the calibration procedure described in section 3.1, applied to the GNSS measurements performed during 2013 and 2014 by means of the receiver installed in Tucuman. Results of the comparisons are presented in Figure 50, Figure 51 and Figure 52 and summarized in Table 9.

Top panel of Figure 50 shows a scatter plot of the vTEC from original version of the NeQuick model vs the corresponding values of the vTEC coming from GNSS. Points appears to be spread especially for the higher values of TEC. Angular coefficient of the linear fit (red line in the top panel) is 0.71 (see Table 9) and the correlation R^2 is 0.31. Bottom panel of Figure 50 shows the residual associated to the linear fit. It is clear that the model in general underestimates vTEC in particular for higher values of vTEC (greater than 50 TECu)

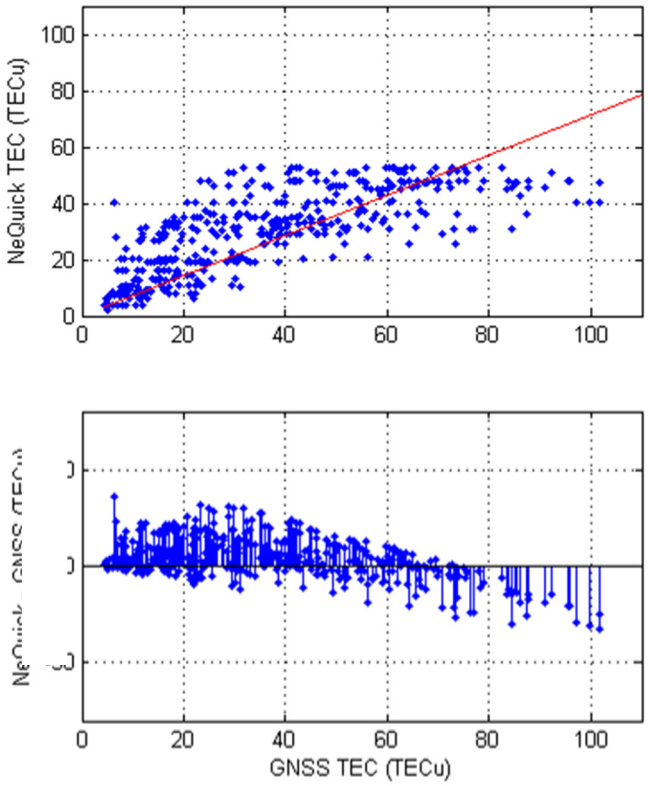

Figure 50. TEC from original version of NeQuick model vs TEC derived from GNSS receiver (top panel). Linear fit of the the data are also represented (red line). Residual associate to the linear fit (bottom panel)

Figure 51 presents the scatter plot of the vTEC from modified NeQuick version (see Figure 49) vs the corresponding vTEC from GNSS. In this case, angular coefficient (0.97) is closer to 1 than the previous case which indicate that the ingestion of measured parameters f_oF2 and M3000F2 improve significantly the performance of the model. The improvement is manly visible for high vTEC values. Correlation coefficient R^2 is equal to the previous one.

Figure 52 reports result of the comparison for the dataset case 3. Even if the dataset is reduced with respect to the previous two, scatter plot shows that the improvement of the performance of the NeQuick model is considerable when a proper data selection is applied on the parameters ingested by the model. In particular angular coefficient of the linear fit is 0.97 indicating the very good agreements between the modelled vTEC and the one from GNSS. Correlation coefficient is also higher than the previous two being equal to 0.56. The residual shown in the bottom panel highlight the improvements of the model performance using dataset case 3 mainly related to the values of vTEC higher than 50 TECu

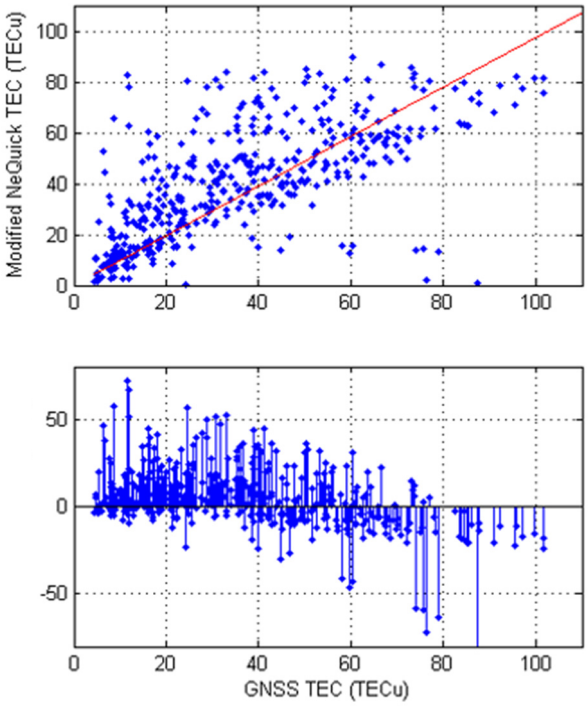

Figure 51. TEC from modified version of NeQuick model (see text for details) vs TEC derived from GNSS receiver (top panel). Linear fit of the the data are also represented (red line). Residual associate to the linear fit (bottom panel)

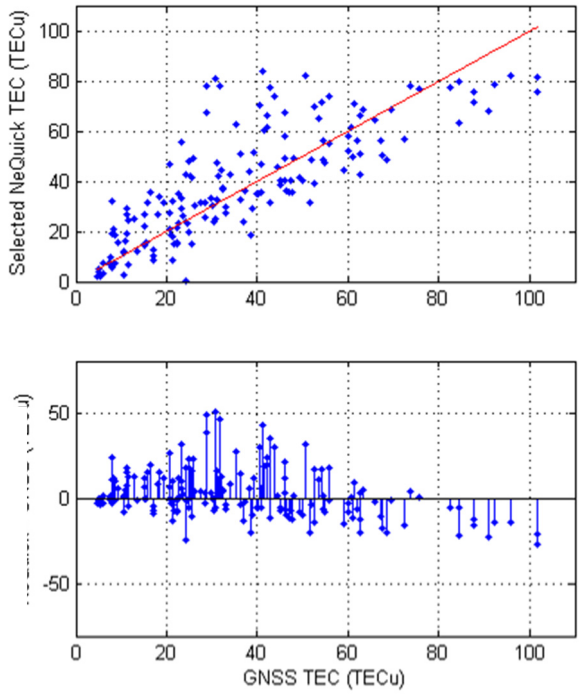

Figure 52. TEC from modified version of NeQuick model and selected with the contrast method (see text for details) vs TEC derived from GNSS receiver (top panel). Linear fit of the the data are also represented (red line). Residual associate to the linear fit (bottom panel)

Table 9. Summary of the linear fit and goodness of fit parameters for the 3 cases presented.

	Original NeQuick	Modified NeQuick	Selected NeQuick
Angular coefficient	0.71	0.97	0.99
SSE	6.344e+04	1.519e+05	3.557e+04
R-Square	0.31	0.30	0.56
RMSE	12.1	18.7	14.7

5.3 Conclusions

The work of this chapter is focused on the analysis of the performance of the climatological model named NeQuick in modelling vTEC at low latitude regions. In particular, GNSS derived vTEC over Tucuman (Argentina) is here used for the comparison with the modelled vTEC by NeQuick. A modified version of the model able to ingest ionospheric parameters from Autoscala applied to Tucuman ionograms is developed in the framework of this work. Finally, a data selection method, developed during this thesis work as well, is applied to proper select data that the model can ingest.

The main outcomes of this work can be summarized as follow:

1. The NeQuick model as it is shows some difficulties in modelling vTEC in the low latitude regions, at least in the southern crest, during solar maximum.
2. The NeQuick model in the present version shows an underestimation of the vTEC especially for values greater than 50 TECu.
3. Using of actual f_oF2 and M3000F2 parameters instead of modelled ones to construct electron density profiles (and consequently vTEC values) improves significantly the performance of the NeQuick. For this scope a modified version of the NeQuick able to ingest these data has been developed.
4. Contrast method used to select input data among data provided by Autoscala works properly when applied to the ionograms coming from Tucuman ionosonde.
5. Selection of the data input with the method proposed increase dramatically the performance of the model in terms of vTEC especially for high values of vTEC.

5.4 References

Bidaine, B. and Warnant, R.: Ionosphere modelling for Galileo single frequency users: illustration of the combination of the NeQuick model and GNSS data ingestion, Adv. Sp. Res. [online] Available from: http://www.sciencedirect.com/science/article/pii/S027311771000596X (Accessed 4 February 2015), 2011.

Cesaroni, C., Scotto, C. and Ippolito, a: An automatic quality factor for Autoscala< i> f</i>< sub> o</sub> F2 values, Adv. Sp. Res., 2013.

Dubey, S., Wahi, R. and Gwal, a. K.: Ionospheric effects on GPS positioning, Adv. Sp. Res., 38, 2478–2484, doi:10.1016/j.asr.2005.07.030, 2006.

Klobuchar, J.: Ionospheric Time-Delay Algorithm for Single-Frequency GPS Users, IEEE Trans. Aerosp. Electron. Syst., AES-23, 325–331, doi:10.1109/TAES.1987.310829, 1987.

Klobuchar, J. a. and Abdu, M. a.: Equatorial ionospheric irregularities produced by the Brazilian Ionospheric Modification Experiment (BIME), J. Geophys. Res., 94, 2721, doi:10.1029/JA094iA03p02721, 1989.

Nava, B., Coïsson, P. and Radicella, S. M.: A new version of the NeQuick ionosphere electron density model, J. Atmos. Solar-Terrestrial Phys., 70, 1856–1862, doi:10.1016/j.jastp.2008.01.015, 2008.

Nava, B., Radicella, S. M. and Azpilicueta, F.: Data ingestion into NeQuick 2, Radio Sci., 46, doi:10.1029/2010RS004635, 2011.

Radiceila, S. M.: The NeQuick model genesis, uses and evolution, Ann. Geophys., 52, 417–422 [online] Available from: ftp://olggps.oeaw.ac.at/pub/GIOMO/papers/4597-4870-1-PB.pdf (Accessed 4 February 2015), 2009.

Scotto, C.: Electron density profile calculation technique for Autoscala ionogram analysis, Adv. Sp. Res., 44(6), 756–766, doi:10.1016/j.asr.2009.04.037, 2009.

Yue, X., Schreiner, W. S., Lin, Y. C., Rocken, C., Kuo, Y. H. and Zhao, B.: Data assimilation retrieval of electron density profiles from radio occultation measurements, J. Geophys. Res. Sp. Phys., 116, doi:10.1029/2010JA015980, 2011.